Spring 2003

Dynamics of Phase Transitions on Low-Index Metal Surfaces

Bo Lin
Old Dominion University

DYNAMICS OF PHASE TRANSITIONS ON LOW-INDEX METAL SURFACES

By

Bo Lin

M.S. Optics, August 1985, Zhejiang University
B.S. Physics, August 1982, Lanzhou University

A Dissertation Submitted to the Faculty of
Old Dominion University in Partial Fulfillment of the
Requirements for the Degree of

DOCTOR OF PHILOSOPHY

ELECTRICAL ENGINEERING

OLD DOMINION UNIVERSITY

May 2003

Approved by:

Hani E. Elsayed-Ali (Director)

Sacharia Albin (Member)

Linda Vahala (Member)

Leposava Vuskovic (Member)

ABSTRACT

DYNAMICS OF PHASE TRANSITIONS ON LOW-INDEX METAL SURFACES

by
Bo Lin
Old Dominion University, 2002
Director: Dr. Hani E. Elsayed-Ali

The surface superheating and phase transitions at the low-index surface of metal were investigated using conventional continuous and 100-ps time-resolved reflection high-energy electron diffraction. Three metal surfaces, In(111), Au(110) and Pb(111), have been investigated in this work. The high temperature behavior of the In(111) surface was investigated using reflection high-energy electron diffraction with 100-ps temporal resolution. The change of surface vacancy density on In(111) is observed from 300 K to near the bulk melting point. The vacancy-formation energy of In(111) surface is estimated from experimental results. The surface vacancy density is observed to increase with temperature; however, the average random step terrace width remains unchanged from its value at room temperature. When the indium surface is heated at a slow rate, the In(111) surface remains ordered up to the highest temperature studied, 4 K below the bulk melting point. When the surface is laser heated at a heating rate of ~10^{12} K/s, the In(111) surface remains ordered up to 73±9 K above its bulk melting pointing. The surface Debye temperature of indium is also obtained from the measurement. The top layer relaxation (or contraction) of In(111) surface is studied.

The vicinal Au(110) surface morphology throughout the (1x2)-(1x1) reconstruction is studied by quantitative reflection high-energy electron diffraction. As the surface is heated from 300 K, the average terrace width remains unchanged up to 635±10 K. Above that temperature, the average terrace width increases and at 683 K has a value (34±10)% more than at 300 K. At higher temperatures, the average terrace width decreases. The average string length at step terraces on Au(110) remains unchanged up to ~ 650 K and decreases sharply at higher temperatures indicative of a step-induced roughening transition. Thermal-induced adatom/vacancy generation on terraces is shown to increase significantly above ~ 680 K. At room temperature, the spacing between the topmost two layers of the Au(110) surface is contracted by 0.31 ± 0.03 Å or ~22% of the bulk-terminated structure.

A laser-driven Photoemission electron microscope with 5 μm spatial resolution was developed and used to study surface morphology of laser heated Pb single crystal. The basic idea of this microscope is the use of ~50 ps ultraviolet laser pulse to photoemit electrons from the surface, while a well synchronized infrared laser pulse heats the surface and induces surface morphology changes. Surface melting and other morphological changes can be imaged. The photoemitted electrons are imaged using three electrostatic electron lenses on a pair of microchannel plates. The UV and IR laser pulses are set at the time which the surface morphology is imaged during pulsed laser heating. When the surface is heated by a picosecond laser pulse, the heating rate is in the order of 10^{12} K/s. Photoemission electron microscopy was used to investigate the dynamics of laser heating-induced morphology changes on Pb(111). Using PEEM, visual images of Pb(111) surface below and above the melting temperature are recorded.

ACKNOWLEDGMENTS

It is my personal pleasure to thank my supervisor, Dr. Hani E. Elsayed-Ali, for his guidance and support. Dr. Ali provided a very stimulating research environment for me throughout my time at Ultrafast Science Laboratory of the Physical Electronics Research Institute, Electrical & Computer Engineering Department of Old Dominion University. I also would like to thank Dr. Sacharia Albin, Dr. Linda Vahala, and Dr. Leposava Vuskovic for serving on my committee.

The help and friendship of Dr. Xinlin Zeng, I. El-Kholy, Dr. Zhihong Zhang, Mohammed Hegazy and my coworkers at PERI Laboratory have enhanced my graduate research career. Finally, I wish to thank my wife and my parents for their encouragement, patience and love.

This work was supported by the US Department of Energy under grant no. DEFG02-97ER45625 and the National Science Foundation, grant no. DMR-998669.

TABLE OF CONTENTS

Page

Page

Page

LIST OF FIGURES

Figure Title Page

LIST OF TABLE

Chapter I

INTRODUCTION

Crystal surfaces undergo several types of phase transitions. The well-known phase transitions are surface reconstruction, surface roughening, and surface melting. The melting phenomenon of metals is one of the most commonly observed phase transitions that one's intuitive reaction is to imagine the familiar sight of a metal, when it is heated, melting from the outside inward. Melting is a process in which, at a certain temperature T_m, the crystalline substance undergoes a phase change from a solid to liquid (melt). When a crystal is heated, its atomic vibrations become stronger and stronger until the temperature reaches T_m and the atoms of the crystal lose their order and become a disordered conglomeration. It is still not possible to observe directly the atomic details of the process. This means that we do not know the process of melting or atom characteristic motions prior to and during melting. A complete understanding of the melting process remains elusive. Time-resolved reflection high-energy electron diffraction (RHEED) provides the means by which we can observe the melting process in real time and how crystalline orientation influences the time-resolved dynamics of the disordering process.

Surface melting is a first-order phase transition. Figure 1 shows a schematic of the Gibbs free energy versus temperature. Surface melting is frequently discussed according to a thermodynamic view. The general mechanism was originally proposed on the basis of qualitative arguments [1.1, 1.2]. The principles of the modern theory were explicitly stated many years later [1.3-1.5]. A well-known expression is that the first derivation of

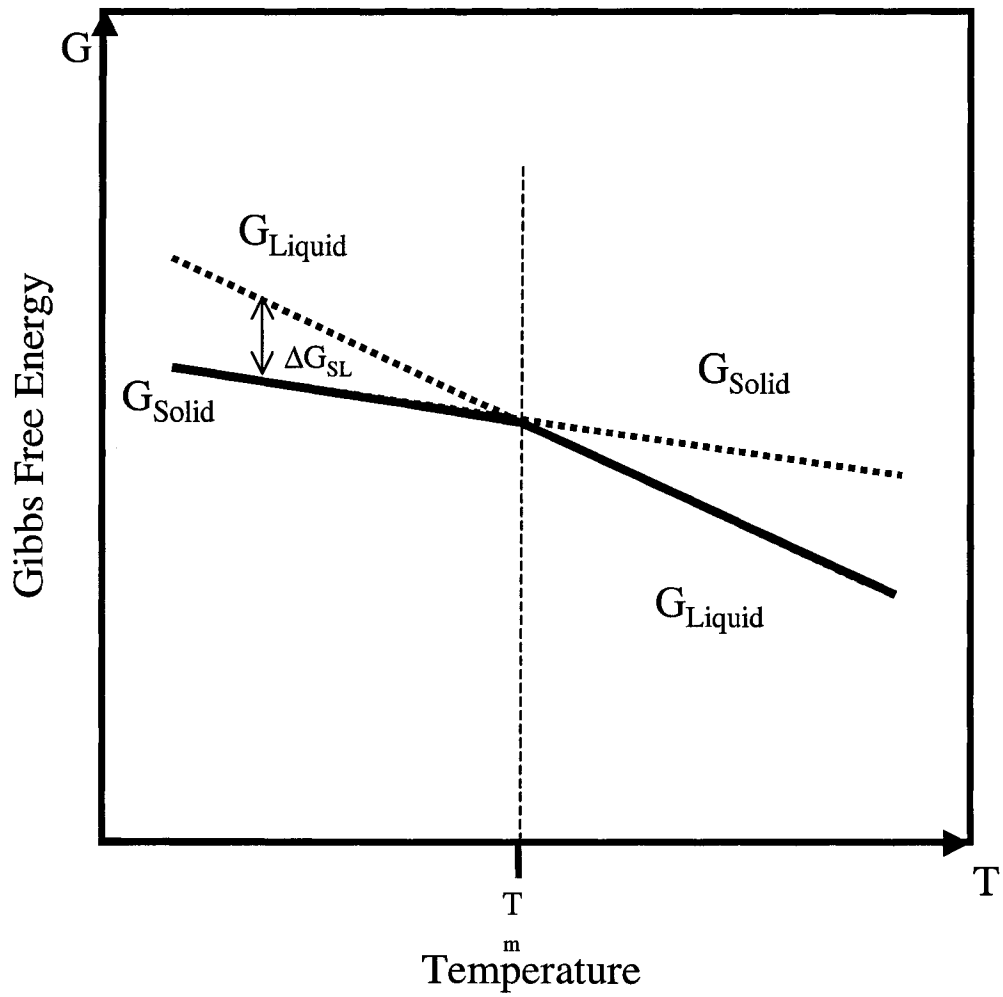

Figure 1. The Gibbs free energy changes with the crystal temperature. The discontinuity of the crystal Gibbs free energy at the melting point indicates a first-order phase transition.

the Gibbs free energy with respect to temperature and pressure is discontinuous across the transition. The interfacial free energy of the solid-vapor, solid-liquid, and liquid-vapor interfaces are defined as γ_{sv}, γ_{sl}, and γ_{lv}, respectively. The tendency of a surface to melting can be expressed as follows:

$$\gamma_{sv} - \gamma_{sl} - \gamma_{lv} = \Delta\gamma > 0$$

Here $\Delta\gamma$ is the free energy change due to melting. If $\Delta\gamma > 0$, it indicates that the surface forms a thin disordered layer between the ordered solid and the vapor, as shown in Fig. 2. If $\Delta\gamma < 0$, then the surface remains dry up to T_m (bulk melting point). The sign and magnitude of $\Delta\gamma$ depend on the material and the surface orientation. Many early experiments on surface melting provided evidence for the existence of the temperature dependence on the surface structure properties that is different from those of the bulk. Because of the asymmetric bonding at the surface atoms and the reduced number of nearest neighbors compared with that of bulk atoms, the atomic mean vibrational amplitudes at the surface are different from those of bulk atoms. This gives clues why different surface packing densities of face centered crystal (fcc), e.g. low index facets (100), (110) and (111), exhibit different surface disorder temperatures. For a fcc metal, an atom on the {110} surface has 7 nearest-neighbor atoms, compared to 12 nearest-neighbor atoms for bulk.

Unlike bulk melting, surface phase transitions can be second-order. The surface is formed by cutting through the solid parallel to a chosen plane or atom. If the atoms are not disturbed from their bulk equilibrium positions by this process, the surface can be considered as a bulk exposed plane, as shown in Fig. 3(a). The loss of nearest neighbor atoms on one side of surface will change their electronic states near and at the surface, as

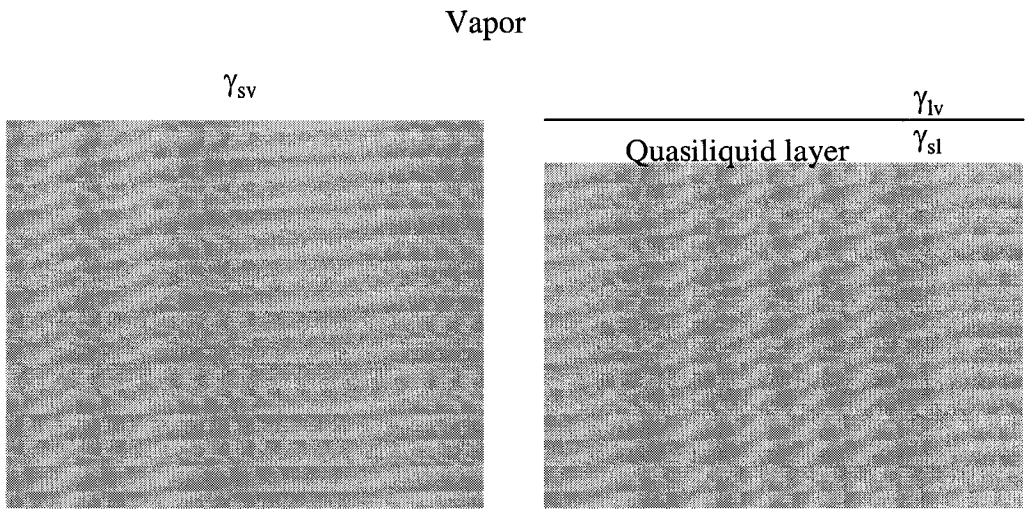

Figure 2. The surface is wetted by its own melt. When the Gibbs free energy of a system can be reduced by converting a layer of solid to liquid, even at a temperatures below the bulk melting point T_m , then a quasiliquid film forms to reduce the system´s Gibbs free energy. (v = vapor, l = liquid, s = solid).

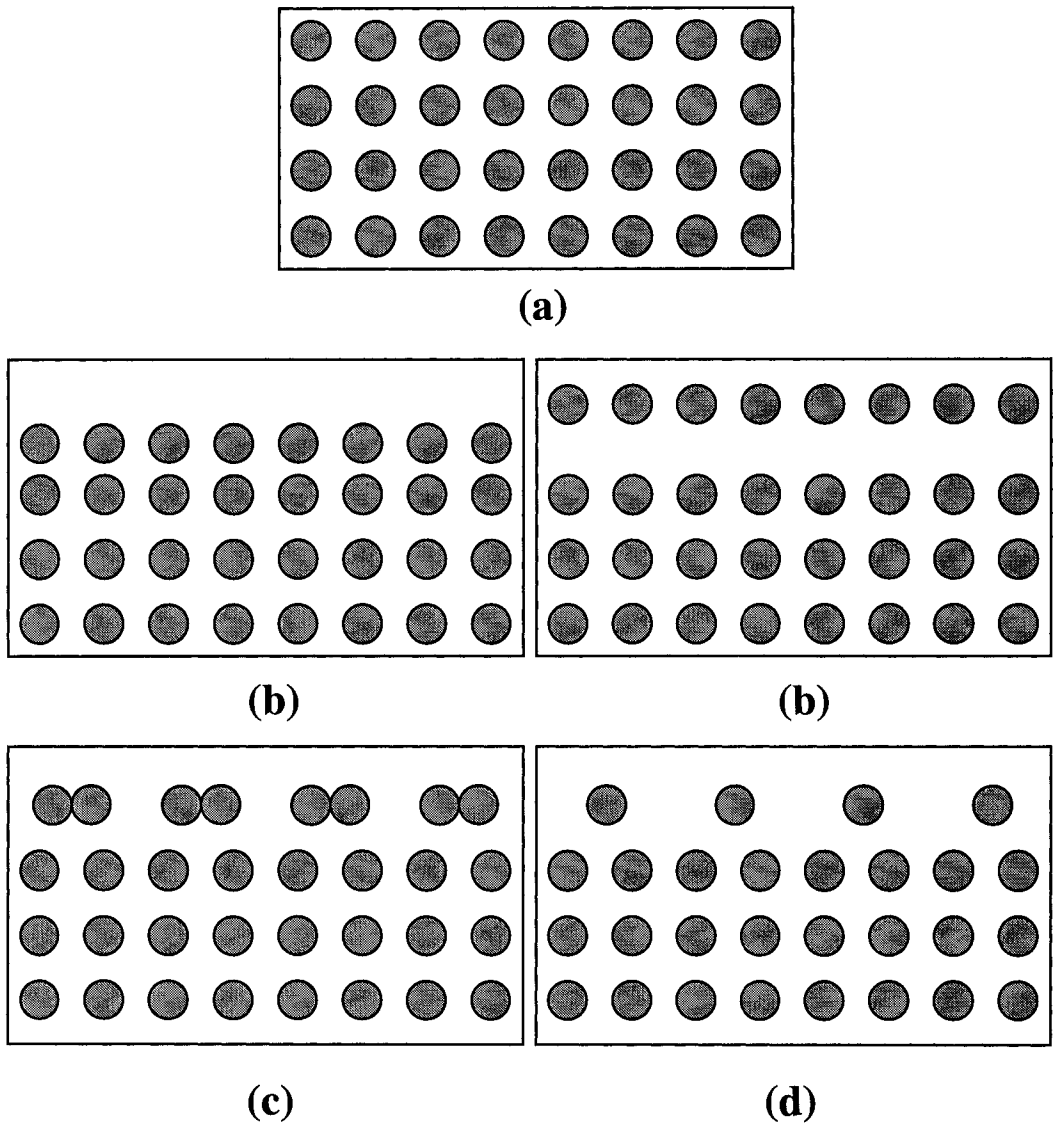

Figure 3. Schematic side view of characteristic rearrangements of surface atoms of a simple cubic lattice. (a) the bulk exposed plane; (b) relaxation of the topmost atomic layer normal to surface (inwards and outwards); (c) reconstruction of the topmost atomic layer; (d) missing row reconstruction with missing atoms in the topmost lattice plane.

a result the surface electronic properties are different from those of bulk atoms. This disturbance will result in new equilibrium positions for the atoms in and near the surface.

Figure 3 shows schematically characteristic rearrangements of surface atoms. Figure 3(b) shows the rearrangements of surface relaxation. Relaxation retains the symmetry of the atomic arrangement parallel to the surface but changes the spacing normal to the surface. The rearrangement of surface reconstruction is shown in Fig. 3(c). The 2D-unit mesh has dimensions different from those of a projected bulk unit cell. Reconstruction also includes surface atomic configurations in which, atoms or an entire row of atoms are missing in comparison with those inside the bulk, as shown in Fig. 3(d). In this case the surface periodicity is always different from that of the bulk. The missing row reconstruction of fcc {110} is a well known class of reconstructions. The {110} surface is the most open surface and is a widely studied low-index fcc surface. Thus, it has the lowest surface layer atomic density and the highest surface energy, making it the most likely to reconstruct. Clean {110} surfaces of Ir, Pt, and Au reconstruct giving rise to the (1x2) missing row reconstruction [1.6]. Au(110) surface is a multilayer reconstruction extending to the fourth layer [1.7]. Of these systems, the Au(110) has been given the most attention [1.8].

The Au(110)-(lx2) reconstruction is stable up to ~650 K. At higher temperature, the intensities of the half-order LEED spots diminish rapidly [1.9]. It was suggested that the top-layer atoms in the high temperature phase of the Au(110) are randomly placed on the surface rather than aligned in rows, but remain in the same type of site as in the ordered structure. The (1x2) to (1x1) phase transition is a 2D Ising transition without large mass transport [1.10]. Although the geometric structure of the reconstruction is well

understood, the basic mechanical stabilizing this geometry and the dynamics of this reconstruction are far from clear. In order to study surface reconstruction and disorder, the Au(110) surface was investigated. In Chapter 5, the Au(110) surface, the most open low-index Au crystal surface, is chosen to investigate surface disorder before T_m.

To study surface superheating, indium is chosen. Indium is selected because of its relatively low bulk melting point (T_m = 430 K) and low vapor pressure near its melting point. In fact the vapor pressure of indium at 641 K (which is 211 K above its bulk melting point) is in the 10^{-11} Torr range which allows for measuring the surface structure with negligible vapor near the surface [1.11]. Unlike Pb which is fcc and Bi which is rhombohedral, indium crystallizes in a close-packed face-centered-tetragonal (fct) structure. The fct structure can be considered as a distorted fcc structure, with less symmetry. In this experiment, we also try to answer whether the symmetry plays an important role or not in surface superheating. One interesting aspect of indium is that it is one of the few elements for which good data exists for its surface free energy anisotropy for T approaching T_m [1.12]. Those measurements were performed by observing the equilibrium shape of micron-sized crystallites using scanning electron microscopy. From this equilibrium shape, the surface free energy anisotropy is obtained using the Wulff construction. If the indium crystal structure is described as an fct with a = b = 4.5912 Å and c = 4.9355 Å, then the ratio between γ_{sv} for the hkl facet to the {111} facet, $\gamma_{sv}\{hkl\}/\gamma_{sv}\{111\}$ has a shape very similar to that measured for Pb. Similar to Pb, γ_{sv} is maximum for the open {110} surface. However, the ratio $\gamma_{sv}\{110\}/\gamma_{sv}\{111\}$ for indium is 1.062 compared to 1.032 for Pb, making the anisotropy stronger for In. In addition to differences in the crystal structure, another interesting difference between Pb and In is in

the surface diffusion of the molten state. There is evidence that surface diffusion of liquid indium is much more than that of liquid Pb. This can be concluded from the impossibility of quenching the equilibrium shape of micron size crystallites of indium using slow cooling rate [1.12]. This quenching, however, was readily observed for the Pb crystallites [1.12]. Enhanced surface diffusion could affect the nucleation and growth of the melt on the surface, and thus affect the surface structural dynamic that we study with time-resolved RHEED.

This dissertation is organized as follows: Chapter 2 is a brief review of the experimental and theoretical works on surface phase transition; Chapter 3 describes the techniques of reflection high-energy electron diffraction (RHEED) with both conventional and time-resolved approach; In Chapter 4, the study of In(111) surface and observation of laser-induced transient surface superheating are presented; Chapter 5 discusses the study of surface deconstruction and surface defects on Au(110) by conventional RHEED; In Chapter 6, A laser-driven photoemission electron microscope was developed and used to study surface morphology during laser heating Pb(111) single crystal; Finally Chapter 7 gives summary and highlights of the present work.

Chapter II

EXPERIMENTAL AND THEORETICAL REVIEW OF PHASE TRANSITION

2.1. Review of superheating theory of low-index surfaces

Theoretical and experimental studies of superheating are still ongoing. It is fundamentally important to understand the two different proposed models of melting. In the first model, the metal crystal melts homogeneously. For the second model, metal crystal initiates melting from the surface. The current theories focus on the nucleation mechanisms that cause crystal melting.

Several approaches attempted to estimate the limits of superheating crystals. Fecht and Johson [2.1] proposed that when the entropy of a superheated crystal exceeds that of the liquid phase, the superheated solid becomes unstable and melts. For Al, W, and Nb, this proposed entropy catastrophe occurs at 1.38, 1.18, and 1.43 T_m respectively [2.1]. According to Lele *et al.*, the superheating temperature can be as high as 2.0 T_m for all alkali metals [2.2]. Lu and Li introduced a new kind of instability involving a massive homogeneous nucleation of the melt that reduced the superheating temperature to 1.2 T_m [2.3]. Using non-classical nucleation theory, Iwamatsu obtained a maximum superheating temperature of 1.11 T_m by examining the homogeneous nucleation of melting in a superheated crystal [2.4]. We will review the catastrophic homogeneous nucleation based on the density functional theory and surface melting based on the thermodynamic model.

2.1.1. The density functional model for crystal melting

Because the melting usually starts at heterogeneous nucleation sites, the early estimating the upper limit for the superheating of crystal based on heterogeneous nucleation. Recently, Lu and Li, and Iwamatsu have proposed a homogeneous nucleation that causes a lower limit of the crystals superheating temperature [2.3, 2.4]. In order to understand first order phase transitions or homogeneous nucleation, we consider the nucleation rate as:

$$J = J_0 \exp[- \Delta W/kT] \qquad (2.1)$$

The unit of nucleation rate J is $cm^{-3} \cdot s^{-1}$ where J_0 is a pre-exponential factor, ΔW is the work of formation of critical nuclei, T is the temperature, and k is Boltzman's constant.

In the density-function model, a solid is treated as an inhomogeneous liquid with spatially varying singlet atomic number density $\rho(r)$. By introducing the order parameters, the Fourier components u_K of local density $\rho(r)$ are the order parameters of the crystal-melt transition. The local density, $\rho(r)$, is defined as

$$\rho(r) = \rho_0 (1 + \Sigma_K u_K e^{iKr}) \qquad (2.2)$$

Where **K** is reciprocal lattice vector of the crystal phase, ρ_0 is the average density of solid. The Fourier component $u = u_K$ is called the 'crystallinity' order parameter. The simple Landau type expansion of the free energy ΔF can be written as follows [2.5]:

$$\Delta F = (n_0 kT/2) \int (a_2 u^2 - a_3 u^3 + a_4 u^4 + b|\nabla u|^2)\, d\mathbf{r} \qquad (2.3)$$

Where n_0, cm^{-3}, is the number density of crystal, a_2, a_3, a_4 and b are expansion coefficients.

The following non-dimensional quantities ϕ, x, and ε are introduced to simplify the free energy.

$$\phi(x) = u(r)/u_0 \text{ and } x = (a_{2m}/b)^{3/2} r \tag{2.4}$$

$$\varepsilon = (1/a_{2m}) \cdot (da_2/dT)_{T=Tm}\Delta T \tag{2.5}$$

where $a_{2m} = a_2$ $(T = T_m)$, $u_0 = (a_{2m}/a_4)^{1/2}$, $\Delta T = T - T_m$ and $\varepsilon = \Delta T \cdot 1.9/(4.3T_m)$ obtained by Iwamatsu [2.4], then the model free energy can be written as,

$$\Delta F = 3\gamma(b/a_{2m}) \cdot (T/T_m)\, \Delta F \tag{2.6}$$

where γ is the surface tension of planar interface at $T = T_m$

$$\Delta F = \int [(\nabla\phi)^2 + \varepsilon\phi^2 + \phi^2 (1-\phi^2)]\, \mathbf{dr} \tag{2.7}$$

ΔF is a non-dimensional free energy. In the non-classical nucleation theory, the spherical liquid droplets are the critical nuclei in superheated crystal. The equilibrium order parameter profile represents a spherical critical nucleus that is determined by the stationary condition.

$$(\delta\Delta F)/\delta\phi = 0 \tag{2.8}$$

Using eq. (2.7) and (2.8), we obtain the differential equation

$$\frac{d^2\phi}{dr^2} - \frac{2}{r}\frac{d\phi}{dr} - (\varepsilon\phi + \phi - 3\phi^2 + 2\phi^3) = 0 \tag{2.9}$$

This equation can only be solved by numerical methods with boundary conditions.

$$\phi(r \rightarrow \infty) = \phi_b \tag{2.10}$$

$$(d\phi/dr)_{r=0} = 0 \tag{2.11}$$

where $\phi_b = 0$ is the condition for freezing and $\phi_b = \phi_+$ for melting.

As we know, that the work of formation of critical nucleus is equal to the free energy ΔF.

$$\Delta F = \Delta W \tag{2.12}$$

and the non-dimensional free energy ΔF is obtained by Iwamatsu [2.4].

$$\Delta F = 160 \tag{2.13}$$

Using equation (2.7), (2.9) and equation (2.13), the superheating and undercooling condition is roughly given by $\varepsilon \approx 0.05$ and $\varepsilon \approx -0.078$, respectively.

From $\varepsilon = \Delta T \cdot 1.9/(4.3T_m)$, the maximum superheating temperature is obtained.

$$\Delta T = 0.11\, T_m \tag{2.14}$$

2.1.2. Thermodynamic model of surface melting

Because the surface plays an important role in initiating of the crystal melting, a thermodynamical model of surface melting has been developed. This model was based on an extension of the mean-field theory of surface melting. Surface melting involves the formation of a thin disorder layer. This disordered layer is not a true liquid and is usually referred to as a 'quasiliquid', as shown in Fig. 2 in Chapter I.

From thermodynamics, the surface is wetted by its own melting. A liquid film of thickness ℓ grows from zero (no liquid on surface) to a finite value. The total free energy change per unit area is [2.6]

$$G_l - G_s = \left(\frac{\partial G_l}{\partial T}\Big|_{Tm} - \frac{\partial G_s}{\partial T}\Big|_{Tm}\right)(T - T_m) + \Delta\gamma(l) \tag{2.15}$$

where G_l and G_s are total free energy of liquid and solid per unit area. As we know

$$S = -\partial G/\partial T \text{ and } \Lambda = T_m \Delta S_m \tag{2.16}$$

where S is entropy and ΔS_m is entropy of melting. Λ is the latent heat of fusion per atom.

$$\Delta\gamma(\ell) = \gamma_{sv} - \gamma_{lv} - \gamma_{sl} \tag{2.17}$$

where γ_{sl} is solid-liquid interfacial free energy, γ_{lv} is liquid-vapor interfacial free energy, and γ_{sv} is solid-vapor interfacial free energy.

$$\Delta G(\ell) = \Lambda\rho(1-T/T_m)\,\ell + \Delta\gamma(\ell) \tag{2.18}$$

where ρ is the atomic density of the liquid.

The first term of this equation is from the free energy difference between solid and liquid. The second term is the free energy that a dry surface has in excess of a surface completely wetted by a macroscopically thick melt. $\Delta\gamma$ is a function of ℓ, the separation between the solid-liquid and liquid-vapor interfaces. When a liquid film of thickness ℓ is zero, it is possible to superheat the surface. By definition, $\Delta\gamma(0) = 0$. When the free energy of a crystal surface satisfies the following conditions, the crystal surface will melt:

(1). $\Delta G(\ell)$ has a minimum at $\ell = \ell_0 > 0$ and

(2). $\Delta G(\ell_0) < 0$

When surface temperature is below the melting temperature, The first term of equation (2.18) is always positive. Thus, a necessary condition is

$$\Delta\gamma < 0 \tag{2.19}$$

to satisfy $\Delta G(\ell) < 0$ in order for surface melting to happen.

By definition, $\Delta\gamma(0) = 0$. Assuming short-range forces, the interfacial energy difference on the film thickness ℓ can be written as an exponential dependence

$$\Delta\gamma = \Delta\gamma_\infty\,[1-\exp(-\ell/\xi)] \tag{2.20}$$

where $\Delta\gamma_\infty = \gamma_{lv} + \gamma_{sl} - \gamma_{sv}$ is the net free energy change upon conversion of the solid-vapor interface in two noninteracting solid-liquid and liquid-vapor interfaces. ξ is a correlation length in the liquid. Let us insert equation (2.20) into equation (2.18), we have

$$\Delta G(\ell) = \Lambda\rho(1-T/T_m)\,\ell + \Delta\gamma_\infty\,[1-\exp(-\ell/\xi)] \qquad (2.21)$$

The optimal liquid thickness can be obtained by minimizing the total free energy and the solution is the well-known formula [2.6].

$$\ell_0(T) = \xi \ln[\frac{|\Delta\gamma_\infty|}{\xi\Lambda\rho(1-T/T_m)}] \qquad (2.22)$$

This is mean-field thickness of the melted film. Equation (2.22) implies the presence of a 'wetting temperature' by $\ell_0(T) = 0$.

$$T_W = T_m[1-\frac{|\Delta\gamma_\infty|}{\xi\Lambda\rho}] \qquad (2.23)$$

For a nonmelting surface with $\Delta\gamma_\infty > 0$ and $T > T_m$, now ℓ^* corresponds to a free energy maximum at a critical thickness.

$$\ell^*(T) = \xi \ln[\frac{|\Delta\gamma_\infty|}{\xi\Lambda\rho(T/T_m - 1)}] \qquad (2.24)$$

The minimum of free energy disappears when $\ell^*(T_i) = 0$ and maximum of free energy disappears above an instability temperature T_i.

$$T_i = T_m[1+\frac{|\Delta\gamma_\infty|}{\xi\Lambda\rho}] \qquad (2.25)$$

Above T_i, the maximum of crystal free energy will disappear and the crystal surface will melt. When the temperature is below T_i, the crystal surface remains solid and can be superheated. For $T_m < T < T_i$, the restriction of crystal superheating is a typical nucleation

problem. As we discussed previously, the upper limit temperature of homogeneous nucleation is 1.11 T_m. According to the above, superheating is a general phenomenon. The maximum superheating temperature is restricted by the instability temperature T_i and the upper limit of homogeneous nucleation.

2.2. Review of low-index metal surface phase transition

2.2.1. Molecular dynamics simulation for high temperature behavior of metal surfaces

The more realistic microscopic description of disordering and premelting or even superheating on crystal surfaces can be obtained using computer-simulation methods, especially the molecular-dynamics (MD) method, where the real dynamics of the atomic system can be followed. There are two methods available for simulation of material at atomic level around non-zero temperatures, namely the Monte Carlo simulation and molecular dynamics simulation. A good introduction to these methods is given in the book by Allen and Tildesley [2.7]. In the molecular dynamics simulation, the positions and velocities of each atom follow Newton's laws of motion. A typical molecular-dynamics simulation cell contains several hundred or a few thousand atoms. The trajectories of the motion can be obtained from potential energy that determined each time step on each atom. To determine averages of quantities, such as energy, stress and order parameters of the system, atoms are followed for a long enough time that a representative set of configurations is generated.

The simplest expression of the potential in the MD method contains two terms, a repulsive pair term and an attractive many-body term. Finnis and Sinclair [2.8], using the tight binding approach, showed that the attractive part should be proportional to the square root of the local density of atoms so that

$$V = \varepsilon_0 \sum_{i=1}^{N} [\sum_{\substack{j=1 \\ j \neq i}}^{N} V_{ij} - c_d \sqrt{\rho_i}] \tag{2.26}$$

$$V_{ij} = (\sigma_L / r_{ij})^n \quad \text{and} \quad \rho_i = \sum_j (\sigma_L / r_{ij})^m \tag{2.27}$$

where σ_L is the fcc lattice constant, c_d is a non-dimension parameter, ε_0 is an energy parameter, and m and n are integers. The first term describes the repulsion between the atomic cores that belongs to Lennard-Jones potential. ρ_i is the electron density at the nucleus of atom i. The second term expresses attractive interaction between the atoms.

There are several other potentials that are used for simulating metals. Daw and Baskes developed the embedded atom potential [2.9]. The effective medium potentials were used by Norskov *et al.* [2.10] and glue potential for gold was developed by Erolesi *et al.* [2.11,2.12]. In generally, potentials show the form of a pair term and a local many-body term.

A copper surface has been simulated by the MD method. A Cu(111) surface has been observed superheating by MD simulation [2.13]. Even through preexisting vacancies exist up to 10% on Cu(111) surface, Cu(111) surface still can be superheated.

2.2.2. Surface melting

When a crystal is heated, its atomic vibration of amplitude become large until a temperature T_m is reached and the atoms forming the crystal lose their order to become a disordered conglomeration. It is still not possible to observe directly the atomic details of the melting process. Characteristic atomic motions prior to and during melting are still not fully understood. Time-resolved RHEED provides the means by which we can measure the temporal evolution of the process and how crystalline orientation influences the time-resolved dynamics of disordering.

Surface melting is frequently discussed according to the thermodynamic view. The general mechanism was originally proposed on the basis of qualitative arguments [2.14,2.15]. The principles of the modern theory were stated many years later [2.16-2.18]. By using the interfacial free energies of the solid-vapor, solid-liquid, and liquid-vapor interfaces, we have the following relation for a surface covered with a disordered layer [2.19]:

$$\gamma_{sv} > \gamma_{sl} + \gamma_{lv} \qquad (2.28)$$

Where γ_{sv} , γ_{sl} , and γ_{lv} are the interfacial free energies of the solid-vapor, solid-liquid, and liquid-vapor interfaces, respectively. Table 1 lists the thermodynamic quantities for a number of elements [2.20]. From this table, we find that indium is a good candidate for surface melting study. Indium is selected because of its relatively low melting point (T_m = 430 K) and low vapor pressure near its melting point. In fact the vapor pressure of indium at 641 K (which is 211 K above its bulk melting point) is in the 10^{-11} Torr range which allows for measuring the surface structure with negligible vapor near the surface [2.20].

Z		T_m(K)	Λ(mJ/m^2)	γ_{sv} mJ/m^2	γ_{sl} mJ/m^2	γ_{lv} mJ/m^2	$\Delta\gamma$ mJ/m^2	Melting(+) Non-melting(-)	$T_m\Delta\gamma/\Lambda$	$P(T_m)$ Torr
29	Cu	1356	21.7	1592	263	1310	19	(+)	1187	4×10^{-4}
32	Ge	1232	57.6	870	273	640	-43	(-)	-920	8×10^{-7}
49	In	430	6.4	638	48	560	30	(+)	2016	1×10^{-11}
50	Sn	505.1	11.8	654	66	570	18	(+)	770	1×10^{-11}
79	Au	1336	21.0	1363	200	1130	33	(+)	2099	1×10^{-5}
82	Pb	600.7	7.9	544	62	460	22	(+)	1673	4×10^{-9}
83	Bi	544.2	18.3	501	74	380	47	(+)	1398	2×10^{-10}

Table 1. Thermodynamic quantities related to surface melting for a number of elements mentioned in this dissertation [2.20]. The symbols are defined as: Z is atomic number, T_m is the bulk melting point, Λ is the latent heat of fusion per atom, γ_{sv},, γ_{sl}, and γ_{lv} are respectively the solid-vapor, solid-liquid and liquid-vapor interfacial free energies, $P(T_m)$ is the vapor pressure at the bulk melting point.

Unlike Pb which is fcc and Bi which is rhombohedral, indium crystallizes in a close-packed face-centered-tetragonal (fct) structure. The fct structure can be considered as a distorted fcc structure, with less symmetry.

Many early experiments provide evidence showing that the structure properties of the surface temperature dependence are different from that of the bulk. Because of the asymmetric bonding at the surface atoms and the reduced number of nearest neighbors compared to those of bulk atoms, the atomic mean vibrational amplitudes at surface are different from bulk atoms. This gives clues why different surface packing density [(100), (110) and (111)] exhibits difference surface disorder temperature. For a fcc metal, an atom on the {110} surface has 7 nearest neighbors compared to 12 nearest neighbors for bulk atoms. For Pb(110) surface, the reversible order-disorder transformation was observed to begin at a temperature as low as 150 K below the bulk melting temperature (T_m = 600.7 K) [2.21]. The atoms on Pb (100) surface have 8 atoms as nearest neighbors. The packing density is in the intermediate to Pb(110) and Pb(111). Pb(100) surface shows limited disorder for temperatures high than 500 K, while Pb(111) surface remains in order up to T_m – 0.05 K [2.21].

The orientation dependent structure disorder of surfaces has been thoroughly studied for Pb. The premelting is particularly visible in open surfaces. Only the free (111) surface has possibility to remain ordered up to near the bulk melting point or even superheat [2.22,2.23]. Molecular dynamics modeling of fcc metals showed good agreement with the experimental data on Pb(100), Pb(110) and Pb(111). The Pb(111) surface was observed to superheat up to T_m + 120 K [2.22]. Pb(100) showed evidence of residual order above T_m.

2.2.3. Phase transition of metal surface

In recent years, it has been determined that in many cases atoms in the surface layer of a crystal do not occupy the positions that would be expected from simple continuation of the bulk lattice structure. Small shifts in atom position either normal or parallel to the surface of the crystal can be made with relatively little expenditure of energy by a surface atom that is constricted on three sides. Because the bonding configurations of the surface atoms are quite different from that of the bulk atoms, a substantial increase in bonding energy may be obtained by a slight shift in position from the "normal" lattice site. Thus, the movement of surface atoms can result in a net lowering of the energy of the system. The energy of the system is lowered by "relaxation" or "reconstruction" of the surface layers so that the dangling bonds can overlap somewhat each other.

The surface is formed by cutting through the solid parallel to a chosen plane or atom. If the atoms are not disturbed from their bulk equilibrium positions by this operation, the surface can be considered as a bulk exposed plane, as shown in Fig. 3(a) in Chapter 1. The loss of nearest neighbor atoms on one side of surface will change the electronic states near and at the surface, and thus surface electronic properties differ from bulk. This disturbance will result in new equilibrium positions for the atoms in and near the surface.

Bonding to *d* orbital, however, is in general more complexes, and because transition metals play such an important role in surface chemistry, the topic warrants

more detailed investigations. The (110) surface of transition metals with face center cubic (fcc) symmetry belong to two different classes. The first class, including the 3*d*-elements Cu, Ni and the 4*d*-elements Rh, Pd and Ag, has a nonreconstructed (1×1) ground state for the clean surface, i.e. they keep the bulk termination (they exhibit however large oscillatory interlayer-relaxations). The second class of fcc metals, including the 5*d*-elements Ir, Pt and Au, exhibits a reconstructed (1×2) ground state. The nature of the (1×2) reconstruction has been studied extensively by a number of different experimental techniques and there is a general agreement now that the (1×2) phase of all three 5*d*-metals is a missing row geometry [2.24] with every second close packed [110] row missing, as shown in Fig. 4.

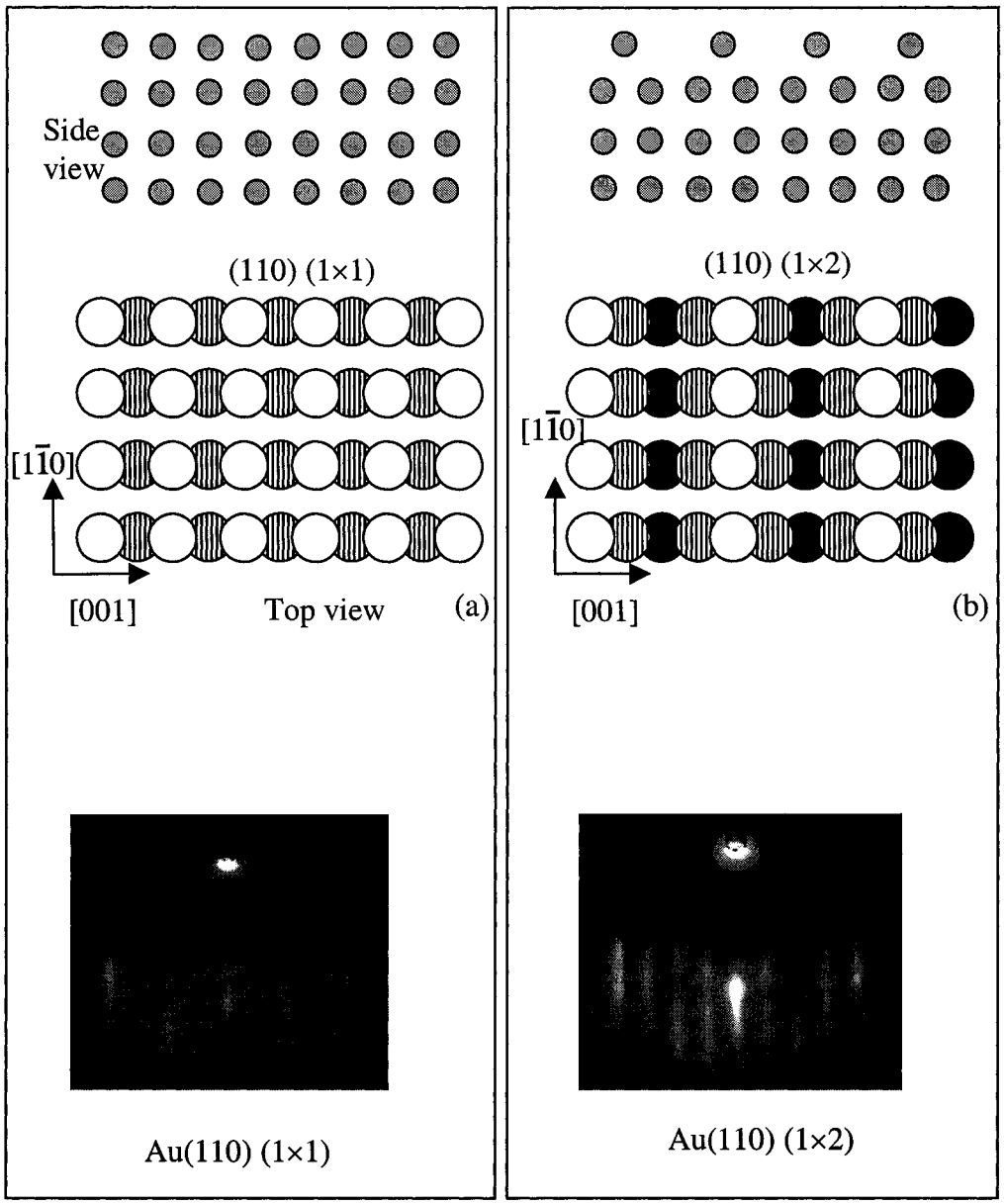

Figure 4. Unreconstructed and reconstructed (110) surface of face-centered cubic metals.

Chapter III

FUNDAMENTALS OF TIME-RESOLVED REFLECTION HIGH-ENERGY ELECTRON DIFFRACTION (RHEED)

3.1 Surface structure and surface lattice dynamics

3.1.1 The surface structure of indium(111)

The primitive unit cell is the simplest periodically repeating unit that can be identified in an ordered array - the array in this instance being the ordered arrangement of surface atoms. By repeated translation of a unit cell, the whole array can be constructed. There are five possible two-dimensional (2D) Bravais lattices, as shown in Fig. 5.

Let us consider the clean surface structures of the low index surface planes of fcc metals. We will use indium as an example. The reciprocal lattice can be obtained by using the real lattice basis vectors as follows:

$$\mathbf{a}^*_1 = 2\pi\mathbf{a}_2\times\mathbf{n}\,/A \qquad (3.1a)$$

$$\mathbf{a}^*_2 = 2\pi\mathbf{n}\times\mathbf{a}_1\,/A \qquad (3.1b)$$

with

$$A = \mathbf{a}_1\cdot(\mathbf{a}_2\times\mathbf{n}) \qquad (3.2)$$

The $\mathbf{a}_i$'s and $\mathbf{a}_i^*$'s are the basis vectors of the real and reciprocal net, respectively. $\mathbf{n}$ is a unit vector normal to the surface and A is the area of the unit mesh.

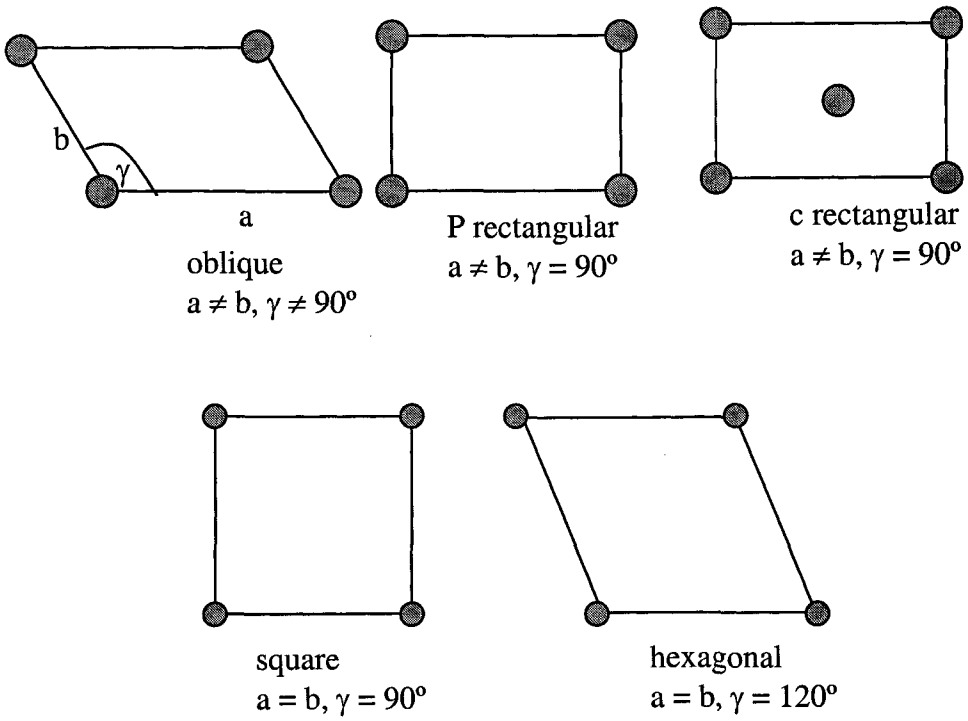

Figure 5. Schematic diagram of five possible two-dimensional (2D) Bravais lattices.

Indium structure has a distorted fcc structure or, more precisely, a face-centered tetragonal (fct) structure with a = b = 4.5912 Å and c = 4.9355 Å [3.1]. Figure 6 shows a diagram of the three faces of fcc(100), fcc(110) and fcc(111) surfaces. The crystalline net of the indium (111) surface is a close-packed hexagonal array. The surface net and its reciprocal net are shown in Fig. 7(a) and Fig. 7(b) respectively, with RHEED patterns at different azimuths. The reciprocal lattice is rotated 28.79 degrees from real net of indium. The basic vectors of the real net are chosen as a_1 = 3.371 Å and a_2 = 3.247 Å, a face-centered tetragonal (fct) structure. The unit vector normal to the surface is in the direction of **n** = (1,1,1). By using equation (3.1) and (3.2), we have

$$a^*_1 = 2\pi \mathbf{a_2}\times\mathbf{n} / \mathbf{a_1}\bullet(\mathbf{a_2}\times\mathbf{n}) = 2.217 \text{ Å}^{-1}$$

$$a^*_2 = 2\pi \mathbf{n}\times\mathbf{a_1} / \mathbf{a_1}\bullet(\mathbf{a_2}\times\mathbf{n}) = 2.21 \text{ Å}^{-1}$$

3.1.2 Surface lattice dynamic

It is well known that the intensity of the diffraction peaks in the RHEED experiment decreases as the surface temperature is raised while the intensity of the diffraction pattern in the diffuse background becomes higher [3.2]. The reason is that the individual atom of the crystal is vibrating independently around their equilibrium position with vibration amplitude that increases with temperature. If I_0 is the intensity of the elastically scattered beam at T = 0 K, then I is the diffraction intensity at temperature T.

$$I_n(T) = I_n(0)\exp(-\alpha\langle u^2(T)\rangle\xi) = I_n(0)\exp(-W_{DW}T) \qquad (3.3)$$

where $I_n(T)$ is the n_{th}-order diffraction intensity at temperature T and $I_n(0)$ is the n_{th}-order diffraction intensity at temperature T = 0 K, ξ is a reciprocal lattice vector, and W_{DW} is the known as the Debye-Waller factor. $\langle u^2(T)\rangle$ is the mean square amplitude of vibration

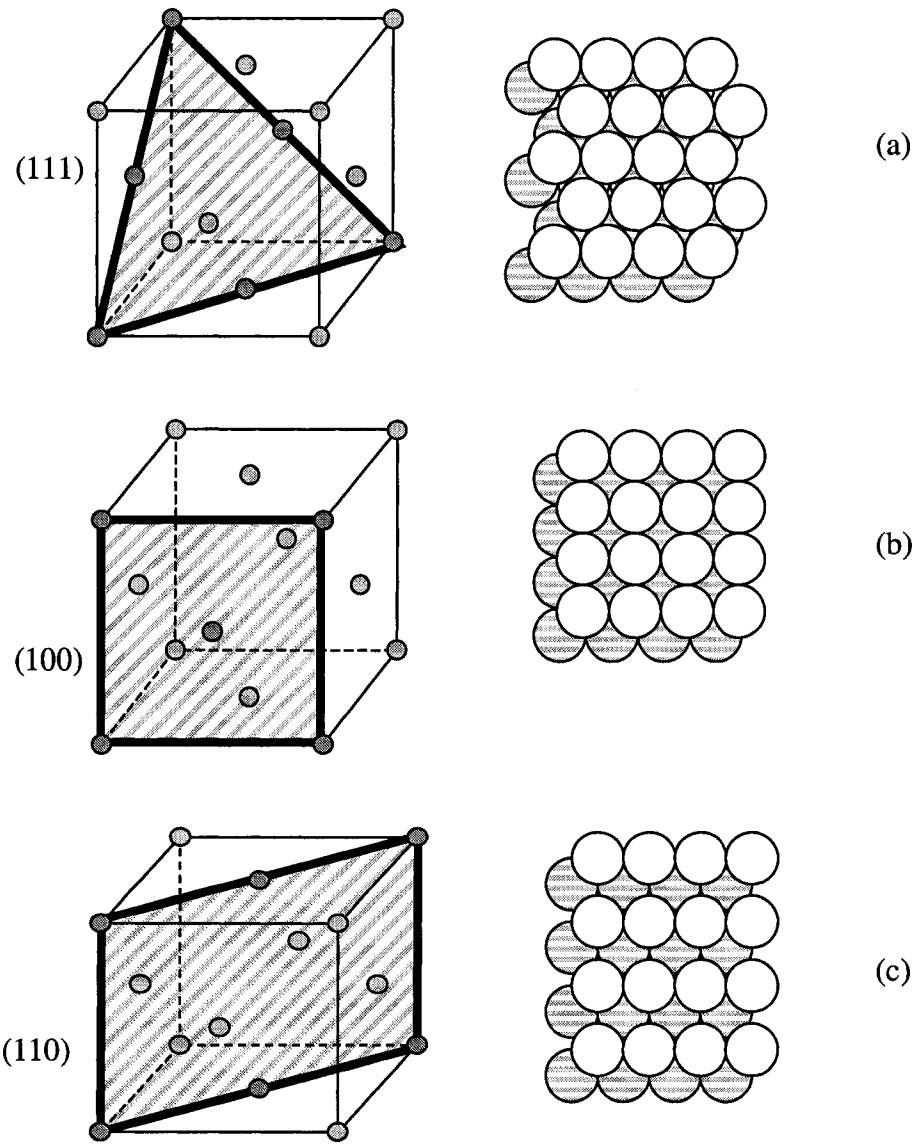

Figure 6. Schematic diagram of the surface parking of the three low-index faces of a fcc crystal.

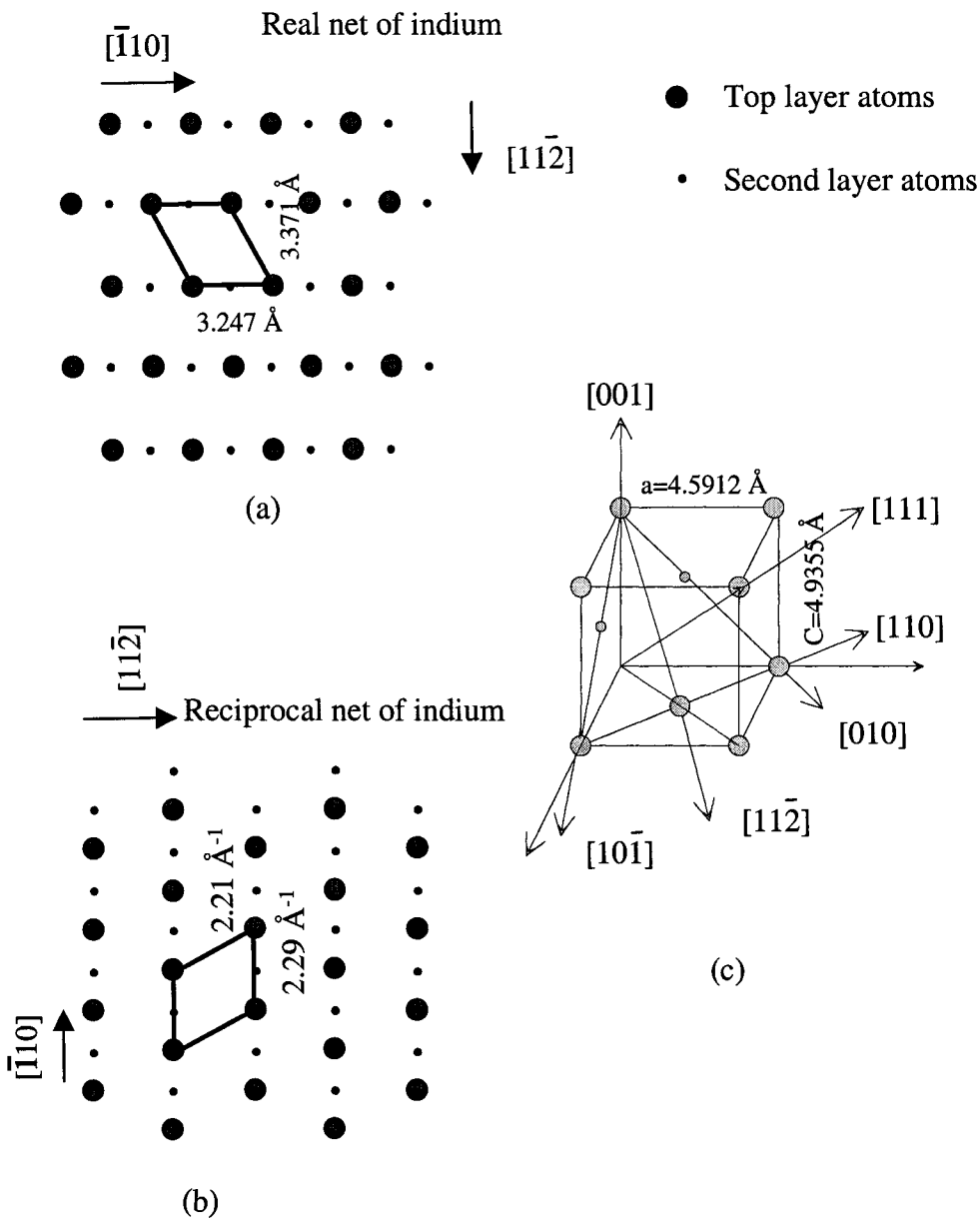

Figure 7. (a) The real nets of the indium (111) face; (b) The reciprocal nets of the indium (111) face; (c) The indium face-centered-cubic lattice, with some planes and directions of interest to RHEED.

in the direction of ξ and α is a constant whose value depends upon the number of dimensions in which the atoms are vibrating. In general, the vibration amplitude of surface atoms perpendicular to the surface is larger than that parallel to the surface. For the low-order streaks (e.g., 00 and 01), ξ in the RHEED geometry is almost perpendicular to the surface.

By using the Debye model of the solid, the Debye-Waller factor W_{DW} can be derived from theory and can be written as [3.2]

$$W_{DW} = [\,|\Delta k_n|^2/|\Delta k_0|^2]\,(4\pi \sin\theta/\lambda)^2(3\hbar^2/mk_b\Phi_D^2) \qquad (3.4)$$

In this Equation, $\hbar$ is Plank's constant divided by 2π, k is Boltzmann's constant, the incident angle θ is defined from the plane of the surface, Δk is the momentum which is in a direction perpendicular to the crystal surface, λ is the electron wavelength of incident beam and Φ_D is the surface Debye temperature. The ratio of $I_n(T)/I_n(0)$ can be experimentally measured. Therefore, the effective Debye temperature, or equivalently $\langle u^2(T)\rangle$ in the direction $\Delta\mathbf{k}$ can be obtained. For instance, the Debye temperature of 49±10 K is obtained from In(111) compare to 108 K for bulk indium [3.1, 3.3].

3.2. Fundamentals of diffraction -- time-resolved reflection high-energy electron diffraction (RHEED)

Reflection high-energy electron diffraction (RHEED) is a surface analysis technique that used to examine the structure of surfaces [3.2-3.4]. Because RHEED can provide information on the surface structure and morphology, it has been used as a probe of the crystal structure and thin film growth.

3.2.1. Fundamentals of diffraction

Let us consider the elastic scattering of radiation with momentum k_0 from a rigid cubic crystal with lattice points

$$\mathbf{r_j} = m_1\mathbf{a} + m_2\mathbf{b} + m_3\mathbf{c} \qquad (3.5)$$

where m_1, m_2, and m_3 are integers and a, b, and c, are the lattice constants. The intensity at the given momentum transfer $\mathbf{S} = \mathbf{k} - \mathbf{k_0}$ is given by [3.4]

$$I(s) = |F(\theta,E)|^2 J(\mathbf{S}) \qquad (3.6)$$

where $F(\theta,E)$ is the structure factor and $J(\mathbf{S})$ is the interference function, $\mathbf{k_0}$ is the scattered wavevector of the incident electron beam, $\mathbf{k}$ is the wavevector of the incident electron beam. For three-dimensional infinite crystal, the interference function is periodic with $\mathbf{G_{hkl}}$, the reciprocal lattice vector and $|\mathbf{G_{hkl}}| = 2n\pi/d_{hkl}$. d_{hkl} is the distance between (hkl) planes. By using the deviation parameter $\mathbf{s} = \mathbf{S} - \mathbf{G_{hkl}}$ and the crystal with limited dimensions N_1a, N_2b and N_3c, the interference function $J(\mathbf{S})$ can be written as [3.2]

$$J(G_{hkl} + s) = \frac{\sin^2[\frac{1}{2}N_1(G_{hkl}+s)\bullet a]}{\sin^2[\frac{1}{2}(G_{hkl}+s)\bullet a]} \frac{\sin^2[\frac{1}{2}N_2(G_{hkl}+s)\bullet b]}{\sin^2[\frac{1}{2}(G_{hkl}+s)\bullet b]} \frac{\sin^2[\frac{1}{2}N_3(G_{hkl}+s)\bullet c]}{\sin^2[\frac{1}{2}(G_{hkl}+s)\bullet c]} \qquad (3.7)$$

when $s = 0$ or $\mathbf{S} = \mathbf{G_{hkl}}$, $\mathbf{J(S)}$ reaches its maximum. $\mathbf{S} = \mathbf{G_{hkl}}$ is called the Laue condition. The interference function $J(\mathbf{S})$ describes the diffraction effects due to scattering.

Other expressions for the Laue condition are

$$\mathbf{S}\cdot\mathbf{a} = 2\pi h,\ \mathbf{S}\cdot\mathbf{b} = 2\pi k,\ \mathbf{S}\cdot\mathbf{c} = 2\pi l, \text{ or } (\mathbf{k}-\mathbf{k_0})\cdot\mathbf{r_j} = 2\pi m \qquad (3.8)$$

where $\mathbf{r_j} = m_1\mathbf{a} + m_2\mathbf{b} + m_3\mathbf{c}$

Another useful method for geometric interpretation the diffraction pattern is the Ewald sphere construction which is a geometric interpretation of the conservation of energy for elastic scattering, i.e. momentum transfer $|\mathbf{S}| = 0$ or $|\mathbf{k}| = |\mathbf{k_0}|$. The magnitude of the vector **k** is

$$|k| = 2\pi/\lambda \tag{3.9}$$

where λ is the electron wavelength, which can be obtain from the relativistic expression [3.5]

$$\lambda = \hbar/\{2m_0qV\,[1 + qV/(m_0c^2)]\}^{1/2} \tag{3.10}$$

where $\hbar$ is Plank's constant divided by 2π, m_0 is the electron rest mass, q is the electron charge, V is the accelerating voltage, and c is the speed of light.

Figure 8 shows the Edwald construction for the elastic diffraction of low energy electrons. Figure 9 shows the RHEED geometry. As the energy or the angle varies, diffraction spots will appear or disappear.

3.2.2. Diffraction from surfaces

In equ. (3.7), $N_3 = 1$ and the third term equals one, the interference function has a constant value for all values of $(\mathbf{G_{hkl}} + \mathbf{s})\cdot\mathbf{c}$. The reciprocal lattice consists of a set of infinitely narrow rods normal to the crystal surface and spaced by $2\pi/a$, $2\pi/b$ apart, where a, b are the inter-row distances in the x, y directions. For a perfect surface, the reciprocal lattice is a set of rods normal to the plane of surface. If the plane is a finite surface and Na×Mb extent in x and y, the widths of the reciprocal-lattice rods broaden.

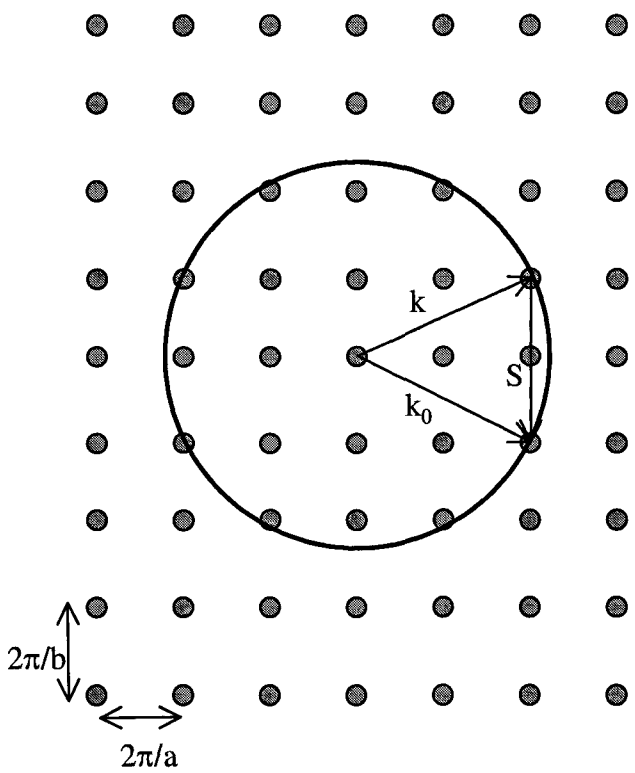

Figure 8. Reciprocal lattice for a single plan of atoms and Ewarld construction for the elastic diffraction of low energy electrons. The diameter of the sphere is k and $k = 2\pi/\lambda$.

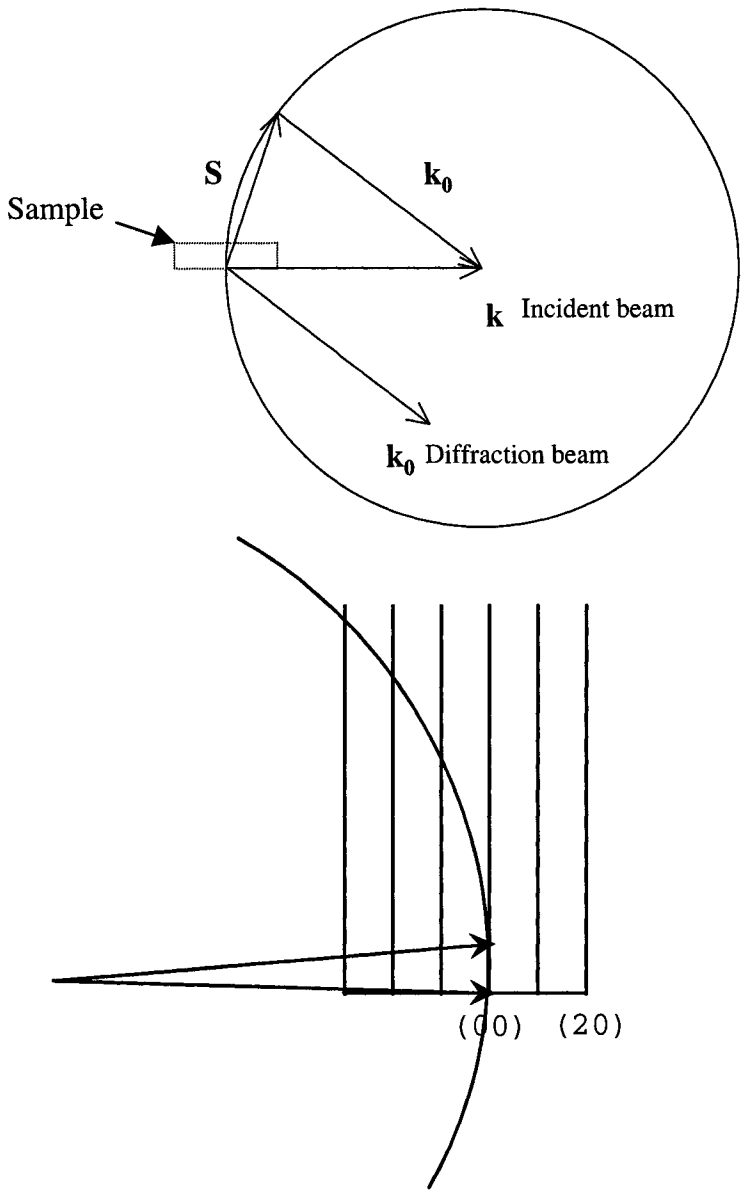

Figure 9. The Ewarld construction for the elastic diffraction of high energy electron. The point of incidence of the beam is the origin of k space.

3.2.3. The experimental geometry of RHEED

The experimental arrangement for RHEED is shown in Fig. 10. The incident electron beam strikes the sample surface at near-grazing angle 1°~3° and is reflected onto a fluorescent screen. The RHEED pattern is recorded via the fluorescent screen and a charge coupled device camera observing the screen and stored in a computer for subsequent analysis. The electron gun and fluorescent screen are positioned remotely from sample and do not interfere with sample. Electrons with energies 5-100 keV range are used. These energies correspond to de Broglie wavelength of λ~0.17-0.04 Å, suitable for probing the structure of the crystal lattices.

3.2.4. Analysis of surface structure from RHEED pattern

The direction and deBroglie wavelength of the incident electron beam are given by,

$$\mathbf{k} = \mathbf{p} / \hbar \text{ with magnitude } k_0 = |\mathbf{k}| = 2\pi/\lambda$$

where p is the momentum of the electrons, $\hbar$ is Planck's constant divided by 2π, and λ is the wavelength of the incident electron beam. The electron beam is incident on the sample surface with a **k** vector and the scattered electrons emerge from the sample surface with a $\mathbf{k_0}$ vector due to elastic scatter, as shown in Fig. 8. The maximum intensity of the diffraction beam is determined from von Laue diffraction condition [3.6].

$$(\mathbf{k} - \mathbf{k_0}) \cdot \mathbf{r} = n \cdot 2\pi \qquad (3.11)$$

where n can be positive or negative integer. The Ewald sphere construction in RHEED is schematically shown in Fig. 10. The radius of Ewald sphere is determined by the $2\pi/\lambda$, λ is the wavelength of the incident electron beam. The electron wavelength is given by equation (3.10) or :

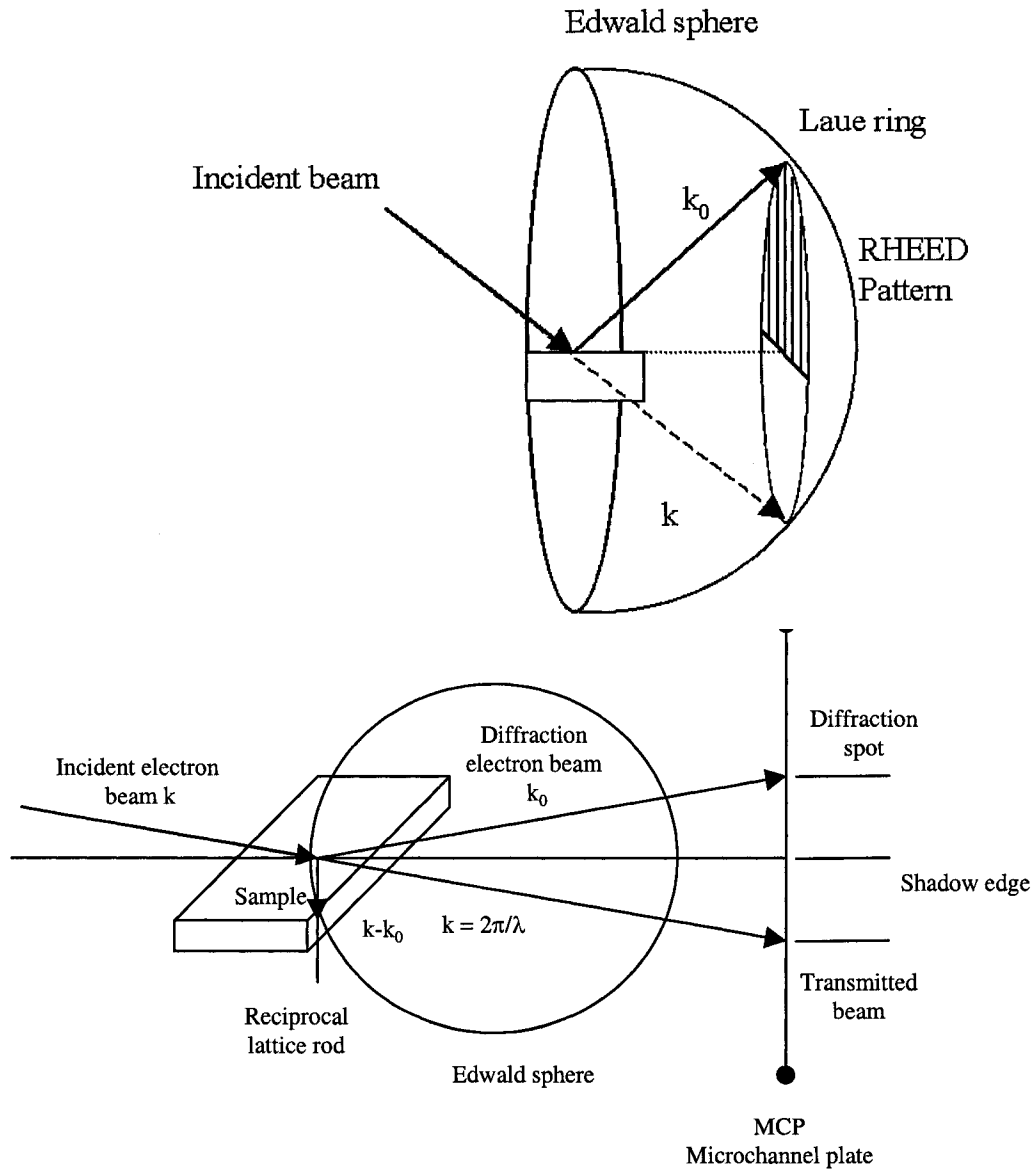

Figure 10. Ewald sphere construction of Laue circle in RHEED. The Ewald sphere construction is determined by the direction and energy of the incident electron beam. The diffracted beam k_0 determines the diffraction spot on the screen.

$$\lambda = 12.3 / [V(1 + 1.95\times10^{-6} V)]^{1/2} \text{ Å} \qquad (3.12)$$

In our indium experiment, V is 21 kV which corresponds to λ = 0.082 Å and Ewald sphere radius = $|\mathbf{k}| = 2\pi/\lambda = 75$ Å^{-1}. The lattice spacing for a metal such as indium is a = 4.5912 Å which gives $2\pi/a \sim 1.4$ Å^{-1} in the reciprocal space. Therefore, the radius of the Ewarld sphere in the case of RHEED is much larger than the reciprocal lattice spacing.

The streaking in RHEED is schematically shown in Fig 9. The Ewald sphere of the reciprocal lattice illustrating the Laue condition $\mathbf{G} = \mathbf{k} - \mathbf{k_0}$. In the reciprocal space, $G_{hkl} = 2\pi n / d$, as shown in Fig. 11(a) and Fig. 11(b).

$$G_{hkl} = 2\pi n / d = 2k_0 \sin\theta \qquad (3.13)$$

Where d is the monolayer height, θ is the angle of incident electron beam and n is integer. And thereby obtain the Bragg equation

$$2d \sin\theta = n\lambda \qquad (3.14)$$

The condition that n is integer is called the Bragg condition, or in-phase condition that the maximum sharp specular streaks of RHEED are formed. If the scattering angle of incident electron beam is corresponding to the number that equals to (n+1/2), this condition is called the out-of-phase condition. For an idealized single crystal, diffraction maxims in the form of sharp spots are predicated in a RHEED pattern. However, streaks are frequently observed due to diffraction from a non-ideal surface. Streaks are caused by instrumental response and sample effects. Because an electron beam has some divergence, spread in kinetic energy and width, the instrumental broadening occurs. Sample broadening occurs because the finite thickness of the reciprocal lattice rods due to surface steps, roughness, irregularities and disorder [3.7]. The analysis of a

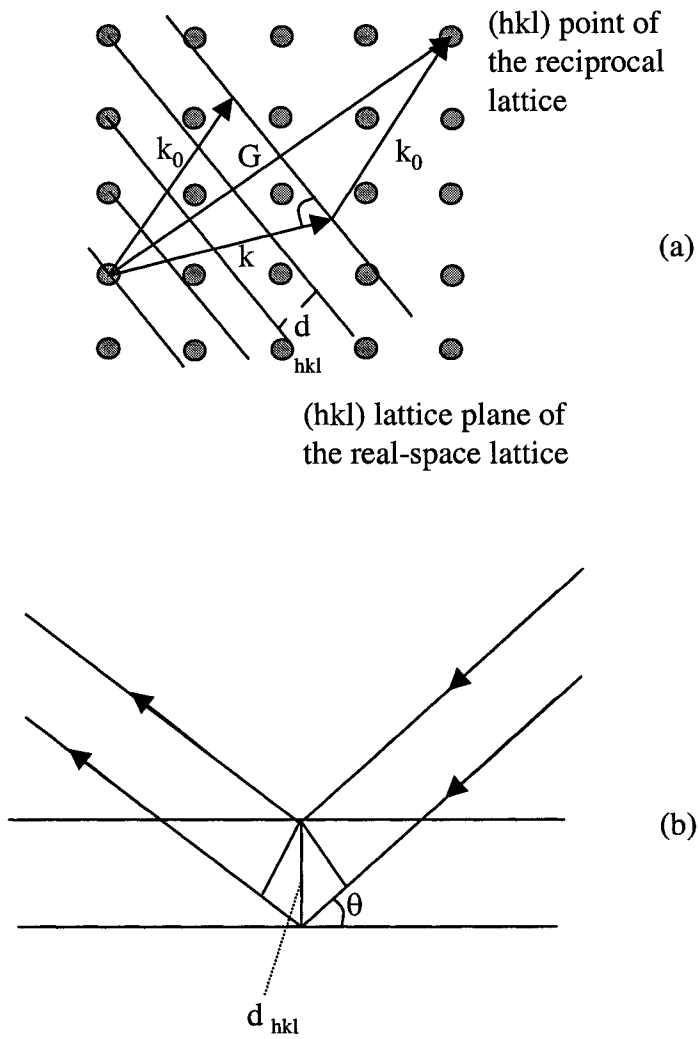

Figure 11. The Bragg interpretation of the scattering condition.
(a) Real space and reciprocal space are superposed here.
(b) Derivation of the Bragg condition. $\lambda = 2\, d_{hkl} \sin\theta$.

symmetrical RHEED pattern can provide information on the lattice structure. We will mainly use indium (111) as an example to discuss.

3.2.5. Lattice spacing can be determined by the streak spacing of RHEED pattern

Figure 12 shows the geometry of the reciprocal lattice spacing between the (00) and (01) diffraction spots. The radius of the Ewald sphere, 76.5 $Å^{-1}$ in our experiment, is much larger than the reciprocal lattice spacing ~ 2.3 $Å^{-1}$. The streak spacing can be obtained from Fig. 12 using the equation:

$$a^* = w\,|k| / L = 2\pi\, w / \lambda\, L \qquad (3.15)$$

Where w is the observed streak spacing in RHEED pattern, L is the distance between sample and screen and λ is the wavelength of incident electron beam. In our experiment, for example, the In(111) surface has lattice spacing $a^* = 2.3$ $Å^{-1}$; the incident electron energy is 21 keV which corresponds to $\lambda = 0.082$ Å and L = 23 cm. The streak spacing of 7 mm on the screen is predicted and is consistence with experimental measurement.

3.2.6. The incident angle of the electron beam

The measurement of incidence angle of the electron beam can be used to obtain in-phase and out-of-phase conditions and order of Laue rings. Figure 12 shows how the electron beam angle at incidence is obtained from relation

$$\varphi = \tan^{-1}(d/L) \qquad (3.16)$$

where d is the distance between the specular spot and the shadow edge of the RHEED screen, and L is the distance between the sample and the screen. An angle of 1°-3° is typically used in RHEED. When the incident angle of the electron beam is scanned, a

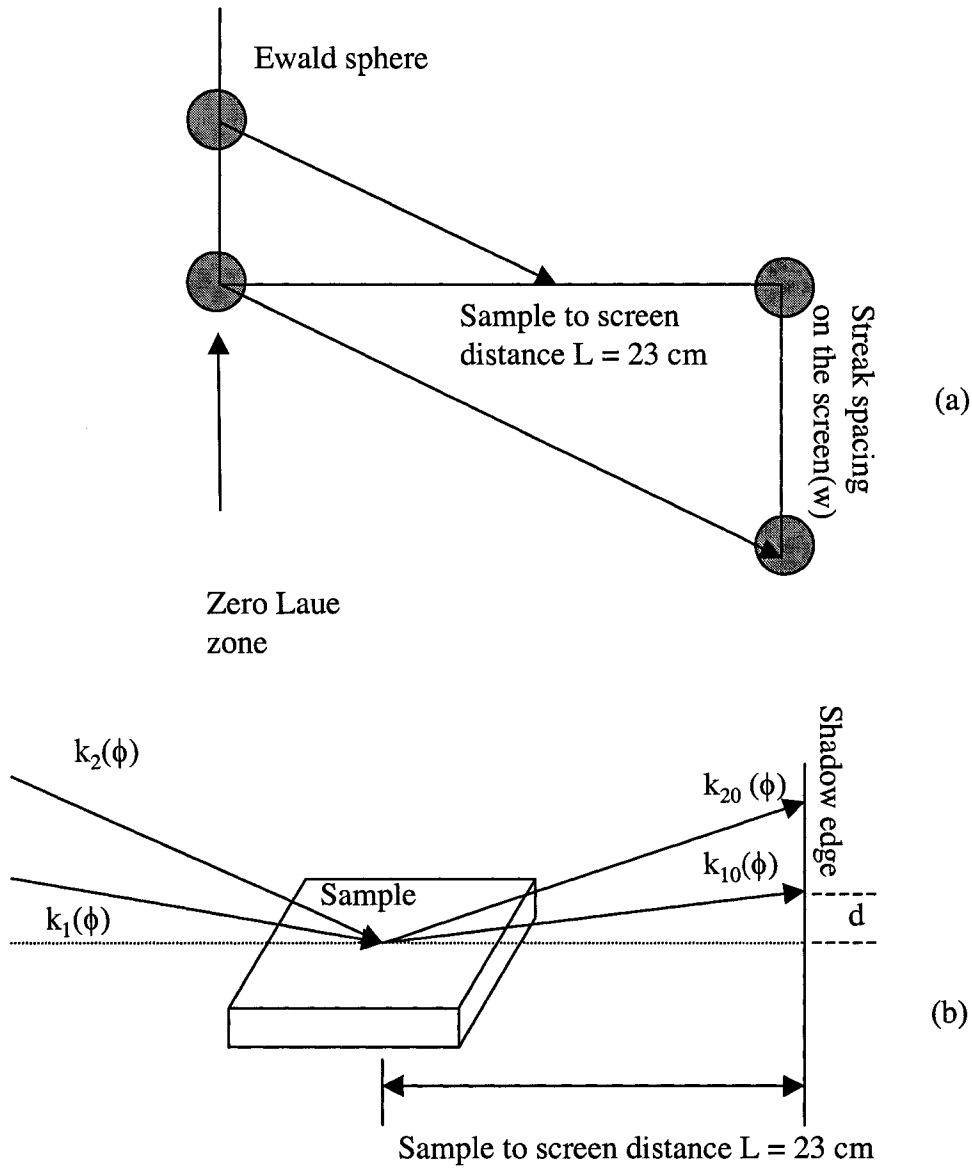

Figure 12. (a) The streak spacing w can be obtained from $a^* = 2\pi w/\lambda L$. (b) The angel of incidence beam can be obtained from the distance between the specular beam and the shadow edge, $\tan(\phi) = d/L$, ϕ is the angle of incidence and k_0 is the momentum vector of the specular beam.

rocking curve is obtained. The surface relaxation information can be extracted from rocking curve. In our Au(110) experiment, a top layer contraction of 22% is observed.

For In(111) , when the electron beam is incident along the [110] direction, the radius of the Laue ring is calculated using Fig. 13(a) and Fig. 13(b). The first Laue ring rod intersects the Ewald sphere at the point B. The Ewald sphere radius, $|k| = 2\pi/\lambda$ is 76.5 $Å^{-1}$ in our experiment (21 keV electron beam). Applying Eq. (3.15), the first Laue ring, AD = (00) – (11) and spacing in the reciprocal lattice can be obtained.

If we observe RHEED in the out-of-phase condition, the information on surface steps and roughness can be extracted from line profile analysis of the RHEED pattern. The intensity of the RHEED streak has two components. The formation of RHEED streak is partially due to the long range order of atoms over the surface and partially due to the surface steps, or roughness. In the out-of-phase condition, the RHEED streak intensity is most sensitive to surface steps or roughness. The vicinal surface consists of terraces arranged in the form of a staircase, and with the electron beam incident down the staircase, the intensity profile of the RHEED along the (00) streak in the out-of-phase condition shows split peaks, as shown in Fig. 14. The spacing of the two split peaks is inversely proportional to the terrace width.

3.3. Time-resolved RHEED: experimental technique

If we change the RHEED continuous electron gun into a pulsed electron gun synchronized with a pulse laser, we will be able to obtain time-resolved information on the surface in a pump-probe experiment. By introducing the time-resolved RHEED

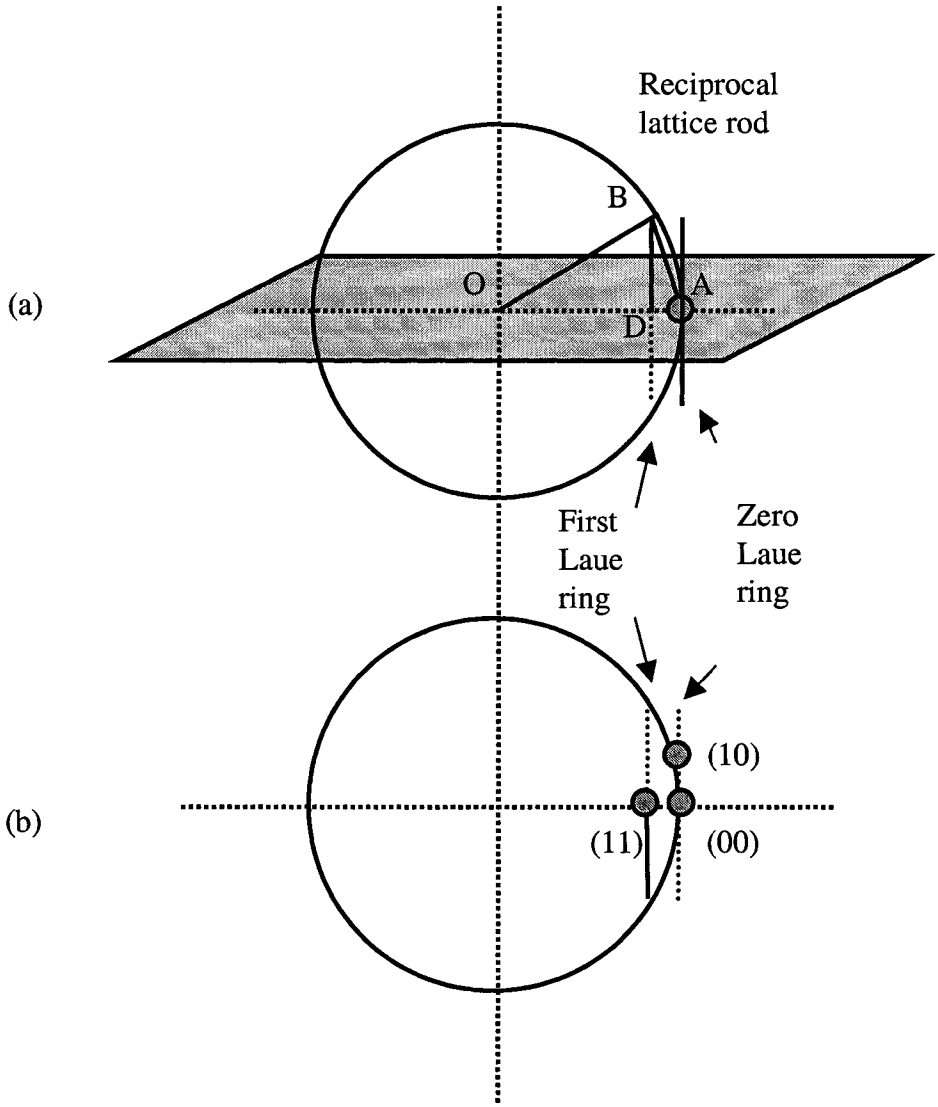

Figure 13. The reciprocal lattice and the Ewald sphere construction (a) cross section (b) plan view.

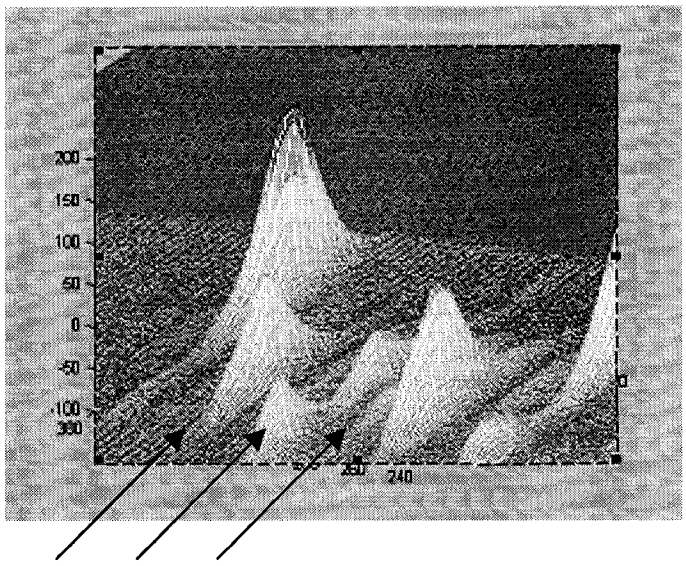

(0,-1) (0,0) (0,1/2)

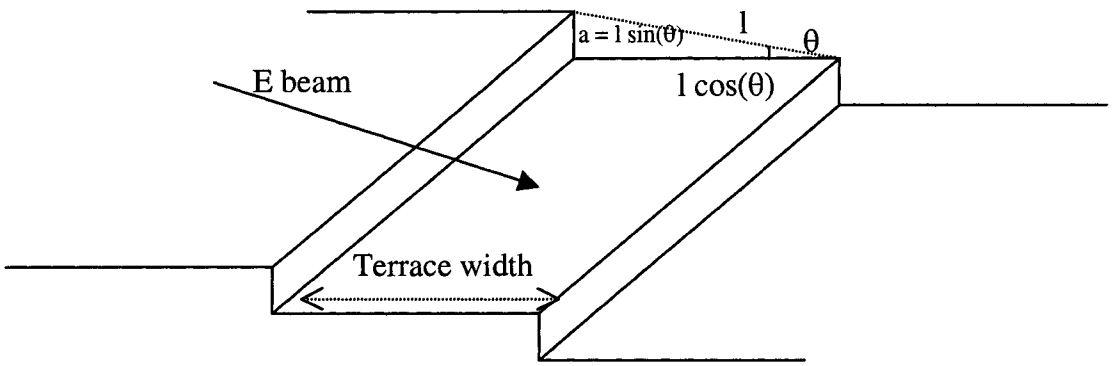

Figure 14. The schematic diagram of vicinal surface and RHEED pattern.

technique, the dynamic behavior of the surface structure can be studied. A schematic diagram of the experimental set-up is shown in Fig. 15. A mode-locked laser produces ~100-ps laser pulses. These pulses are amplified to 30 mJ at 50 Hz repetition rates by two steps, a cw pumped Nd:YAG regenerative amplifier and a pulsed single-pass amplifier. The long-term fluctuation of pulse to pulse is within ± 8%. The fundamental beam of the Nd:YAG laser (λ = 1.06 μm) is split into two beams. One beam interacts with the crystal surface at near normal incidence angle and is used as a transient heating source. The other beam is frequency quadrupled to the ultraviolet (λ = 0.266 μm) and strikes the cathode of a photoactivated electron gun, generating a pulsed electron beam synchronized with the heating laser pulse. The temporal width of the electron pulse is comparable to heating laser pulse. The electrons are accelerated to energy up to 21 keV in a photoactivated electron gun. Thus, by delaying the laser heating pulse relative to the probing electron pulse, it is possible to probe the dynamic behavior of surface structure.

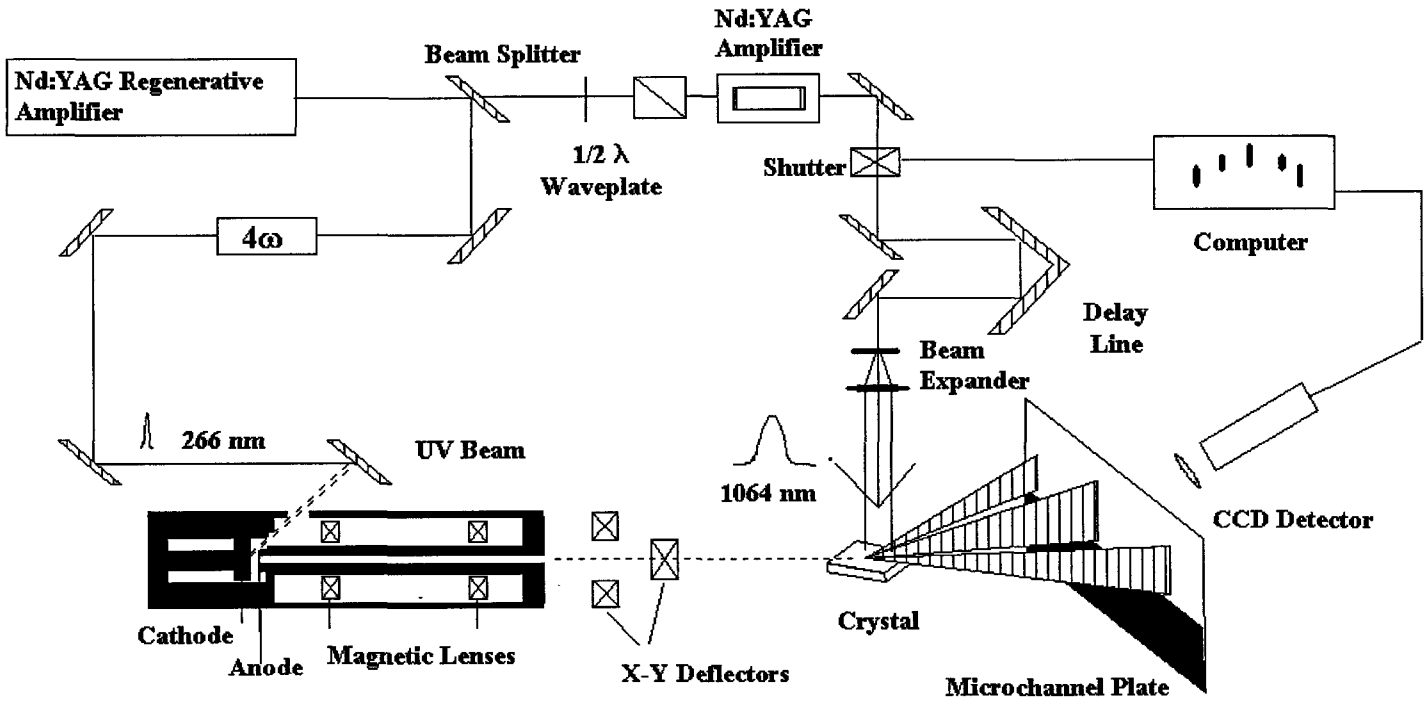

Figure 15. The schematic diagram of time-resolved RHEED experimental.

Chapter IV

TIME-RESOLVED REFLECTION HIGH-ENERGY ELECTRON DIFFRACTION STUDY SURFACE MORPHOLOGY AND SUPERHEATING OF In(111)

4.1. Introduction

It is well established that melting is initiated at surfaces and extended defects [4.1]. The solid-liquid interface plays an important role in melting and crystallization, especially in the kinetics of the phase transition [4.2]. From a thermodynamic point of view, the solid phase and the liquid phase may coexist, while the kinetics of the phase transition indicates that melting occurs because of a structural instability upon heating [4.3]. One of the characteristics of melting is the observed lack of symmetry between undercooling of the liquid during crystallization and superheating of the solid during melting. Liquids can be easily undercooled; however, superheating of solids is observed only under special conditions. For metals, because of the low viscosity of the melt, the liquid-solid interface propagates rapidly into the bulk, precluding superheating of the solid under usual heating conditions [4.4]. Moreover, several metal surfaces have been shown to premelt below the bulk melting point (T_m) thus, providing a vast nucleation site for melting [4.5-4.8]. Surfaces that do not premelt were shown to superheat [4.9-4.14]. Heating the surface by 200-ps laser pulses and observing its structure with time-resolved

reflection high-energy electron diffraction (RHEED), the Pb(110) surface was shown to reversibly disorder below T_m [4.11]. In contrast, the Pb(111) surface was observed to superheat up to T_m + 120 K [4.12]. Pb(100) showed evidence of residual order above T_m [4.13]. In addition to Pb(111), a face-centered crystal, Bi(0001), a rhombohedral structure, was also shown to superheat by ~90 K using 200-ps time-resolved RHEED [4.15]. Molecular dynamic (MD) simulations studied superheating of close-packed metal surfaces [4.16-4.19]. Questions remain on the conditions under which a surface or a solid can be superheated and the limits of superheating.

Theoretical studies estimated the limits of superheating crystals. Fecht and Johnson proposed that when the entropy of a superheated crystal exceeds that of the liquid phase, the superheated solid becomes unstable and melts [4.20]. For Al, W, and Nb, this proposed entropy catastrophe is predicted at $1.38T_m$, $1.18T_m$, and $1.43T_m$, respectively [4.20]. According to Lele et al., the superheating temperature can be as high as $2.0T_m$ for alkali metals [4.21]. Lu and Li introduced a new kind of instability involving a massive homogeneous nucleation of the melt which reduced the superheating temperature to $1.2T_m$ [4.22]. Using nonclassical nucleation theory, Iwamatsu obtained a maximum superheating temperature of $1.11T_m$ by examining the homogeneous nucleation of melting in a superheated crystal [4.23].

We report on the temperature dependence of the surface structure and morphology of In(111). For slow heating, In(111) does not premelt up to the highest temperature studied, 4 K below T_m. When the temperature is raised, the surface vacancy density increases; however, the average surface random step terrace width does not change from its room temperature value. When heated with a 100-ps laser pulse, In(111)

transiently superheats. Transient superheating differs from the thermodynamic superheating studied in Refs. [4.20-4.23] in that it is a metastable phase.

Indium was selected because of its relatively low bulk melting point (T_m = 430 K) and its low vapor pressure near T_m. The vapor pressure of indium 211 K above T_m is ~ 10^{-11} Torr. This allows for measuring the surface structure with negligible vapor pressure near the surface [4.24]. Unlike Pb which is fcc and Bi which is rhombohedral, indium has a face-centered-tetragonal structure. Indium is one of the few elements whose surface free energy anisotropy is well measured [4.25]. The ratio between γ_{sv} for the *hkl* facet to the {111} facet, $\gamma_{sv}\{h\,k\,l\}/\gamma_{sv}\{111\}$ has a shape similar to that measured for Pb. Our time-resolved RHEED measurements show that the In(111) surface can be transiently superheated up to 73 ± 9 K (1.17 ± 0.021T_m).

4.2. Experimental methods

The experiment is performed in an ultrahigh vacuum chamber with a base pressure in the low 10^{-10} Torr. Time-resolved RHEED, described in detail elsewhere [4.26-4.28], was used to investigate surface melting and superheating [4.11-4.15, 4.29 and 4.30]. A Nd:YAG laser produces 100-ps, 30 mJ pulses at 50 Hz repetition rate. The fundamental beam of the laser, λ = 1.06 μm, is split into two beams. One interacts with the In(111) surface at near normal incidence and is used for transient heating. The other is frequency quadrupled to λ = 0.266 μm and strikes the cathode of a photoactivated electron gun, generating an electron pulse synchronized with the heating laser pulse and with a temporal width comparable to it. The heating laser pulse-to-pulse and long-term

fluctuations are within ± 8%. The heating laser beam at the surface of the sample is ~8 mm in diameter, measured at full-width at half-maximum (FWHM); large enough to cover the 6-mm square sample. The spatial nonuniformity of the laser beam is ± 12% across the surface as measured by a scanning pinhole 100 μm in diameter. The photoactivated electron gun produces 21-keV pulsed electrons for RHEED [4.29]. The diffraction pattern is detected by a micro-channel plate and phosphor screen assembly and lens coupled onto a charge-coupled device camera for intensity analysis. A total of 3000 laser pulses are used for each datum. By changing the optical delay between the heating laser pulse and that activating the photocathode, the time evolution of surface structure can be investigated. The photoactivated RHEED gun can also be operated using a continuous ultraviolet source, e.g., a mercury high-pressure lamp, to activate the photocathode.

Two In(111) samples were used. The single crystals were grown from indium of 99.999% purity and cut to within ± 1° of the In(111) surface, as characterized by the manufacturer. Before placing the indium single crystal into the ultrahigh vacuum chamber, the surface was cleaned in a mixture of 30% HNO_3 and 70% ethanol. Because indium is a very soft metal, we took extreme care in mounting it by using soft Ta sheet springs. A thermocouple was placed between the retaining clip and the surface of the indium. The thermocouple and temperature controller were calibrated to the freezing and boiling temperatures of water and the melting temperature of a small piece of indium. The temperature measurement uncertainty was estimated to be ± 2 K with a stability of ± 0.5 K. The crystal surface was cleaned by Ar-ion bombardment (1.0 - 1.5 keV) at near normal incidence. We first Ar-ion bombarded the surface at room temperature for a day.

Then, we raised the sample temperature to ~ 410 K and continued bombardment of the surface for another day. The last step in surface preparation was annealing the sample for one day at near T_m. This procedure was repeated several times until no contamination was detected by Auger electron spectroscopy and a clear RHEED surface pattern was obtained. During the experiment, Ar-ion bombardment and annealing treatments were repeated periodically in order to avoid slow accumulation of surface impurities. Figure 16 shows the Auger spectrum of sample before cleaning. It is clearly seen that the surface is contaminated by carbon and oxygen. Figure 17 shows the Auger spectrum after Ar^+ sputtering and annealing cleaning. The only peaks on the Auger spectrum are indium.

4.3. Experimental results

RHEED patterns were obtained from a clean In(111) for different electron beam incident angles off the surface ranging from 0.5° to 5.0°. Fig. 18 shows the measured RHEED rocking curve for the specular beam obtained at room temperature with the 21-keV electron beam incident along the [110] direction. In the kinematic diffraction approximation, intensity maximum in the rocking curve corresponds to the in-phase Bragg condition in which electrons scattered from different surface layers interfere constructively. An intensity minimum in the rocking curve corresponds to the out-of-phase condition; electrons scattered from different surface layers interfere destructively. In the out-of-phase condition the diffraction is most sensitive to surface defects [4.31].

In Fig. 18, two peaks, A and B, correspond to the in-phase condition for m = 2 and 3, respectively. The measured angles for the in-phase condition, 2.0° and 4.3°, are

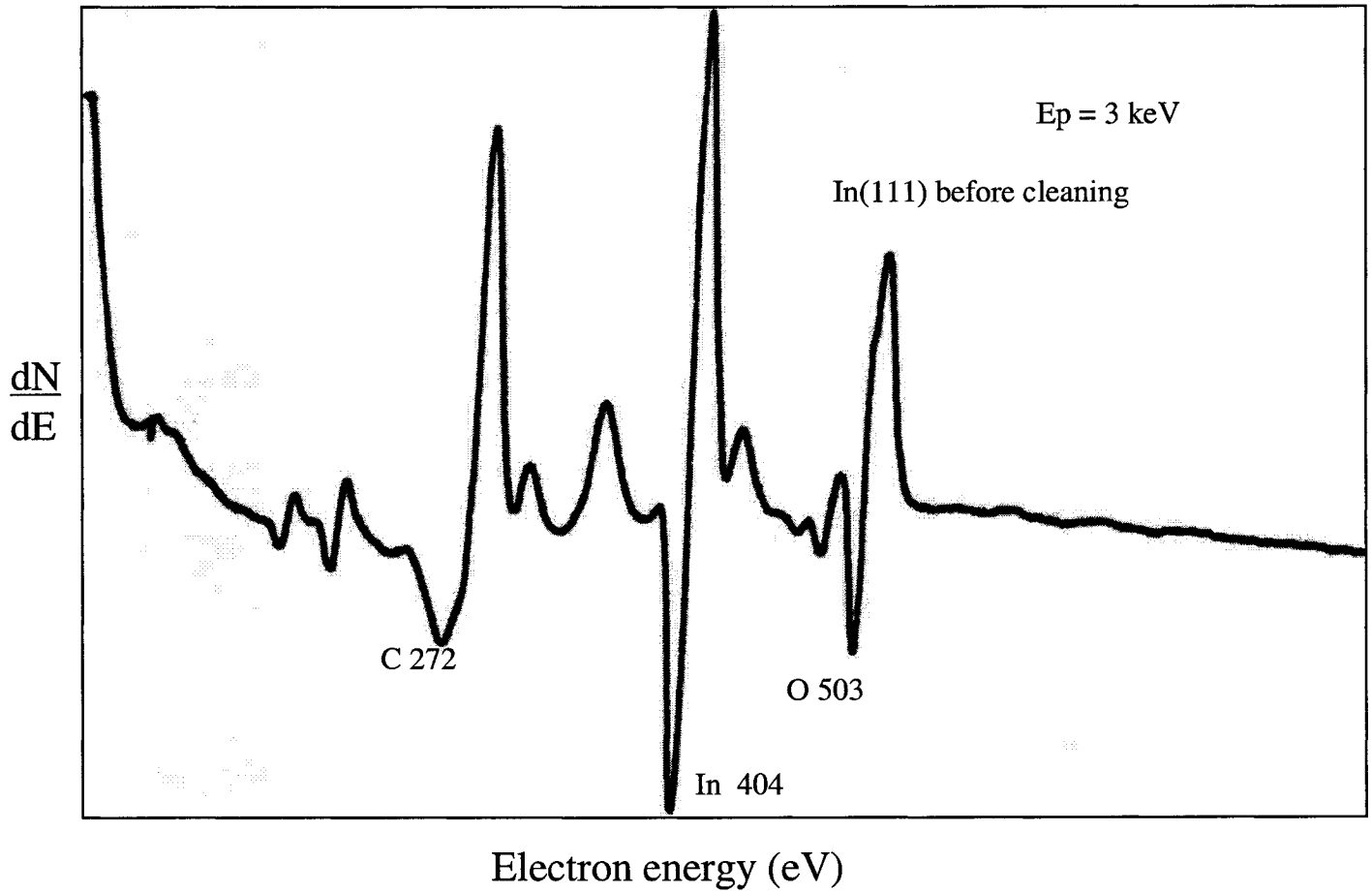

Figure 16. Auger spectrum of the indium surface before Ar^+ sputtering cleaning. The Auger peaks include those from indium, carbon and oxygen.

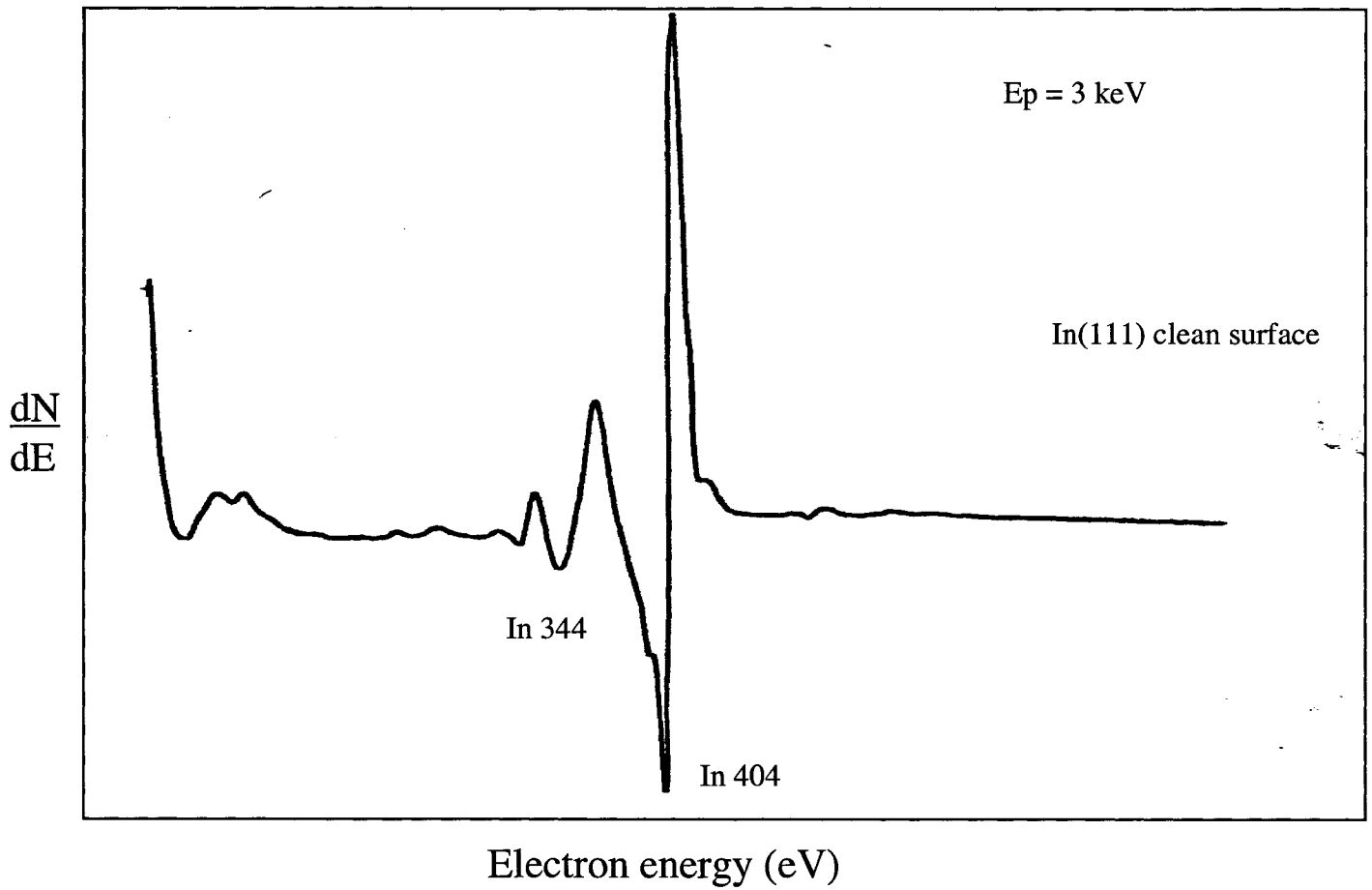

Figure 17. Auger spectrum of a indium surface after Ar^+ sputtering cleaning and annealing. The peaks of Auger spectrum include only from indium.

larger than the calculated angles of 1.87° and 3.92° perhaps due to the contraction of the top surface layers. A spacing between two In(111) layers of 2.72 Å and an inner potential of 12.75 eV are used in the calculation [4.32, 4.33]. The RHEED pattern in the insert of Fig. 18, taken at an electron incident angle of 4.3°, shows 1×1 structure of the clean In(111) surface.

The surface Debye temperature is obtained from the temperature dependence of the specular peak intensity for an electron beam incidence angle corresponding to the in-phase condition. The indium sample was heated from 300 to 426 K (T_m-4 K). The electron beam was incident at an angle of 2.0° from surface, leading to a probed depth of about two monolayers. Fig. 19 shows the results where the intensity of the RHEED specular beam, normalized to its value at 300 K, is in agreement with the exponential Debye-Waller behavior up to T_m-4 K, which is the highest temperature studied. This indicates no surface premelting below T_m. Lack of premelting of In{111} facets was previously observed in a study of the equilibrium shape of small In crystals [4.34]. From the slope of the curve in Fig. 19, the surface effective Debye temperature is determined to be 49 ± 10 K compared to 108 K for bulk indium. The Debye temperature is related to the mean square atomic vibrational amplitude; $\Phi_{Dsurface} \propto [\langle x^2 \rangle]^{-1/2}$, where $\langle x^2 \rangle$ is the projection of the vibrational amplitude of surface atoms along the direction of electron momentum transfer. As expected, the surface atoms have an out-of-plane component of mean-square vibrational amplitude larger than bulk atoms at the same temperature.

The surface Debye temperature $\Phi_{Dsurface}$ relates the diffraction intensity to surface temperature. In time-resolved RHEED, diffraction intensities during and after surface

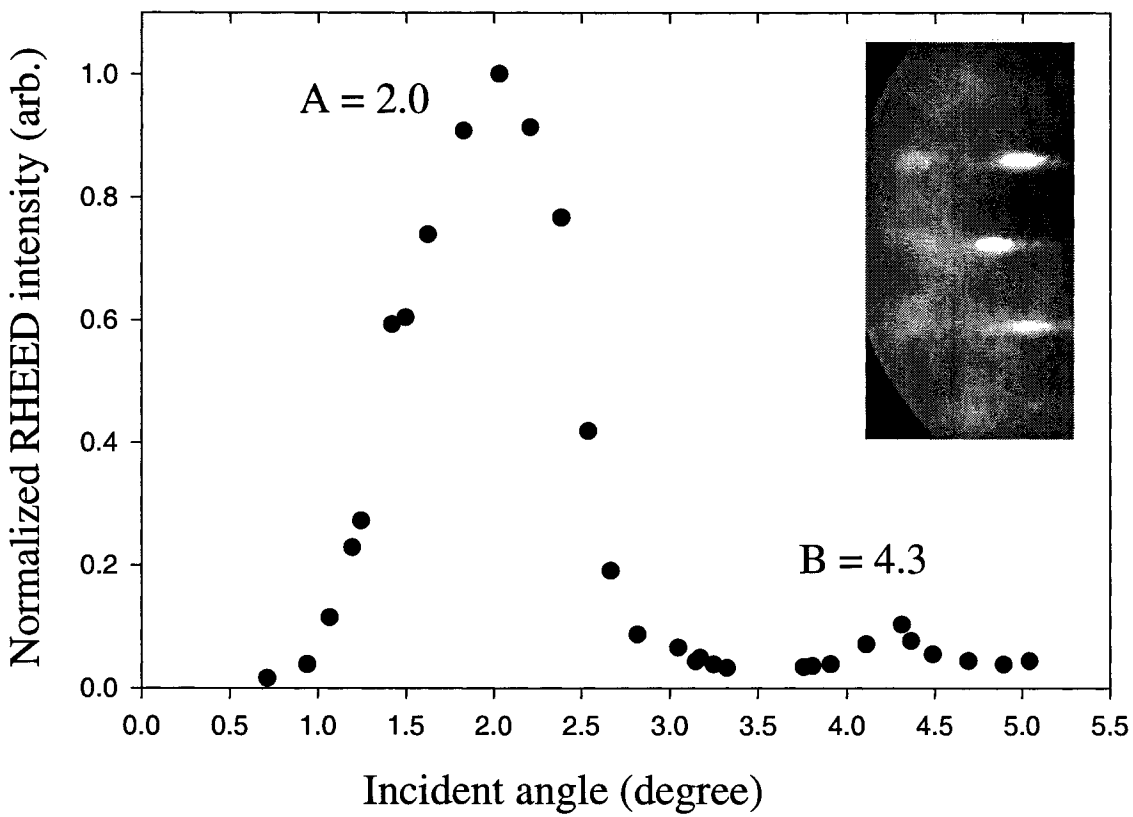

Figure 18. Rocking curve peak intensity of RHEED streak of the (00) beam for the clean In(111) surface obtained at room temperature. The electron beam is incident along the [110] direction. The two peaks A and B, A = 2.0° and B = 4.3°, correspond to the in-phase condition for m = 2 and m = 3, respectively. The inserted picture shows a clear RHEED pattern of the 1×1 structure.

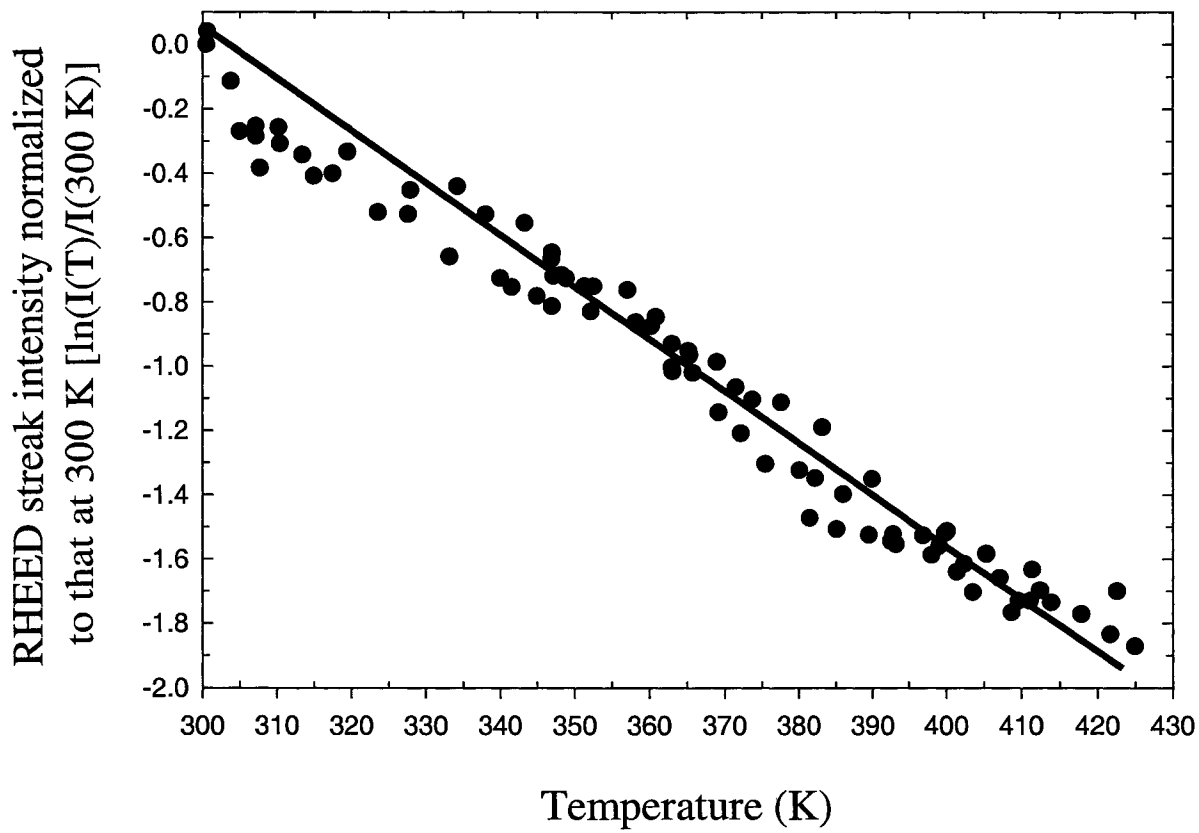

Figure 19. Peak intensity of RHEED streak of In(111) normalized to that at 300 K versus temperature. The behavior of peak intensity of RHEED streak as a function of surface temperature is consistent with the Debye-Waller effect throughout the temperature range studied. From the slop of this curve, the surface Debye temperature of In(111) is determined to be 49±10 K.

laser heating are obtained with 100 ps temporal resolution. We use $\Phi_{Dsurface}$ with time-resolved RHEED to obtain the temporal evolution of the surface temperature as a result of laser pulse heating. This temperature measurement is valid only for time scales longer than that needed for the electrons and phonons to reach equilibrium with themselves and with each other which is expected for the time scale considered [4.35]. Moreover, the transient temperature measurement assumes that the laser is operated at a fluence that does not induce a surface phase transition, and that the Debye harmonic oscillator assumption is valid. Deviation from the exponential Debye-Waller behavior is not observed in the slow heating experiments up to T_m - 4 K, which was the highest surface temperature for slow heating. Deviation from this exponential behavior in laser transient heating is interpreted as the onset of surface melting. The depth that RHEED probes is limited to a few atomic layers; much less than the laser absorption depth. Thus, the probed layer has a uniform temperature although heat diffusion transports heat from the laser surface absorption region to the bulk of the sample during and after the heating laser pulse.

In the time-resolved RHEED experiments, the indium sample was kept at a base temperature of 426 K on the heating stage, and transiently heated by ΔT that depends on the peak laser fluence I_p. The RHEED specular beam intensity normalized to that at T_{base} = 426 K was obtained at t_0, where t_0 is the time of maximum modulation of the normalized specular beam intensity. The time t_0 occurs after the peak of the laser heating pulse but before the laser pulse is terminated. Fig. 20 shows a semi-logarithmic plot of the normalized RHEED intensity ($I_{laser\text{-}heated}/I_{base\text{-}temp}$) at t_0 versus laser fluence. In Fig. 20, there are two regions that relate to melting and superheating. The linear region, for

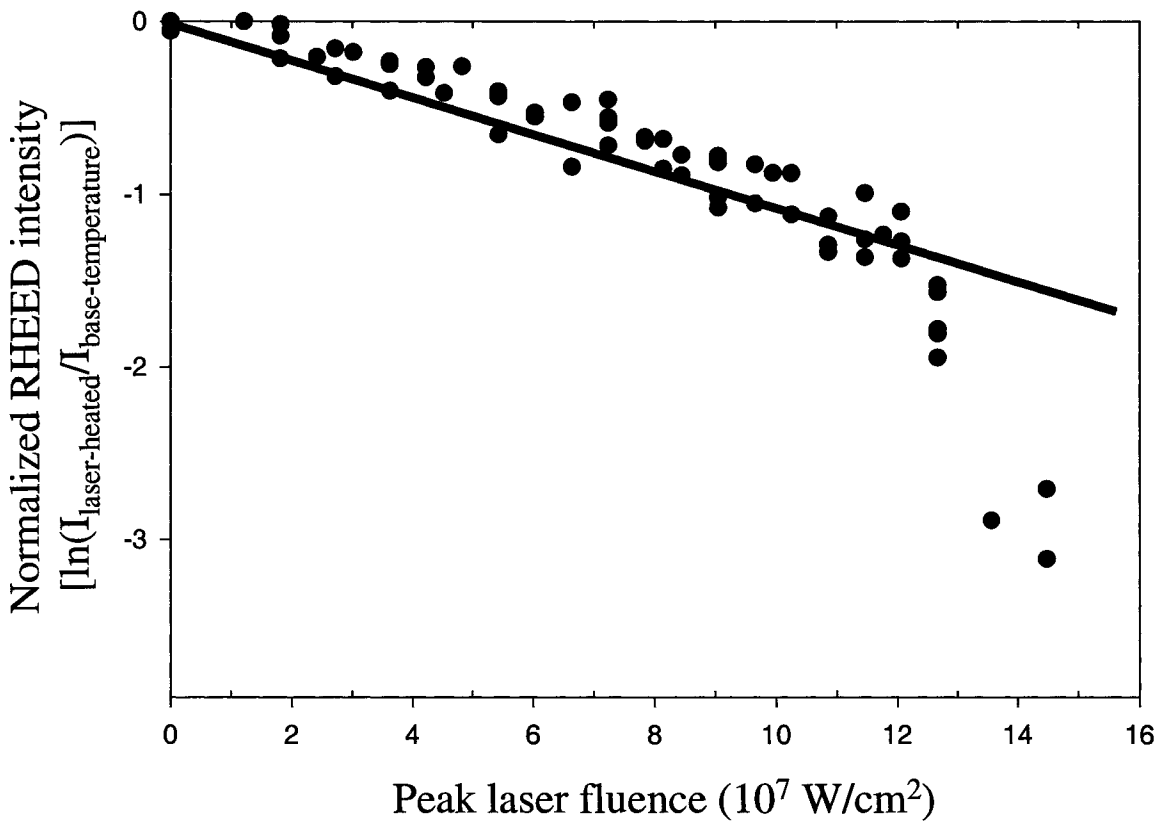

Figure 20. The peak intensity of RHEED streak of In(111) normalized to that at 426 K versus peak laser fluence. A plot of the data on a semi-logarithmic scale showing deviation from Debye-Waller behavior at I_p = 1.2×10^8 W/cm^2. The corresponding temperature is 503±9 K, which is approximate 73±9 K above T_m.

$I_p<1.2\times10^8$ W/cm^2, follows the Debye-Waller behavior with $\Phi_{Dsurface}$ about equal to that measured below T_m. In the second region, $\ln(I_{laser\text{-}heated}/I_{base\text{-}temp})$ significantly deviates from the Debye-Waller behavior. This indicates that the In(111) surface remains solid at t_0 for $I_p < 1.2\times10^8$ W/cm^2. For higher fluences, the surface experiences disorder consistent with melting. The peak temperature jump ΔT is taken to be directly proportional to I_p since the thermal conductivity and optical properties of indium are only weakly dependant on temperature, thus, are assumed constant for the studied temperature range. From Fig. 19 and Fig. 20, a maximum surface superheating temperature of ~T_m + 73±9 K is obtained, corresponding to $I_p = 1.2\times10^8$ W/cm^2.

We next discuss the temporal evolution of the specular RHEED beam intensity. The normalized specular beam intensity was obtained at different base temperatures and different heating laser fluences for various delay times between the arrival of the laser heating pulse and the electron probe pulse at the surface. The indium sample was raised to a base temperature of 313 K on a heated stage and a peak laser fluence of 0.9×10^8 W/cm^2 was used to transiently heat the surface. Fig. 21 shows the result of our measurement and a computer simulation using a one-dimensional heat diffusion model [4.27]. The material parameters used for indium were: heat capacity C = 1.726×10^6 J/m^3 K; thermal conductivity κ = 84 W/m K; absorption coefficient at λ = 1.06 μm α = 9.4×10^7 m^{-1}; and reflectivity at λ = 1.06 μm R = 0.897 [4.36]. The solution of the heat diffusion model (solid line in Fig. 21) is consistent with the experimental results (open circles) within the experimental error. Fast heat diffusion to the bulk limits the surface superheated time to a few hundred picoseconds. The duration of 1/e-time of the

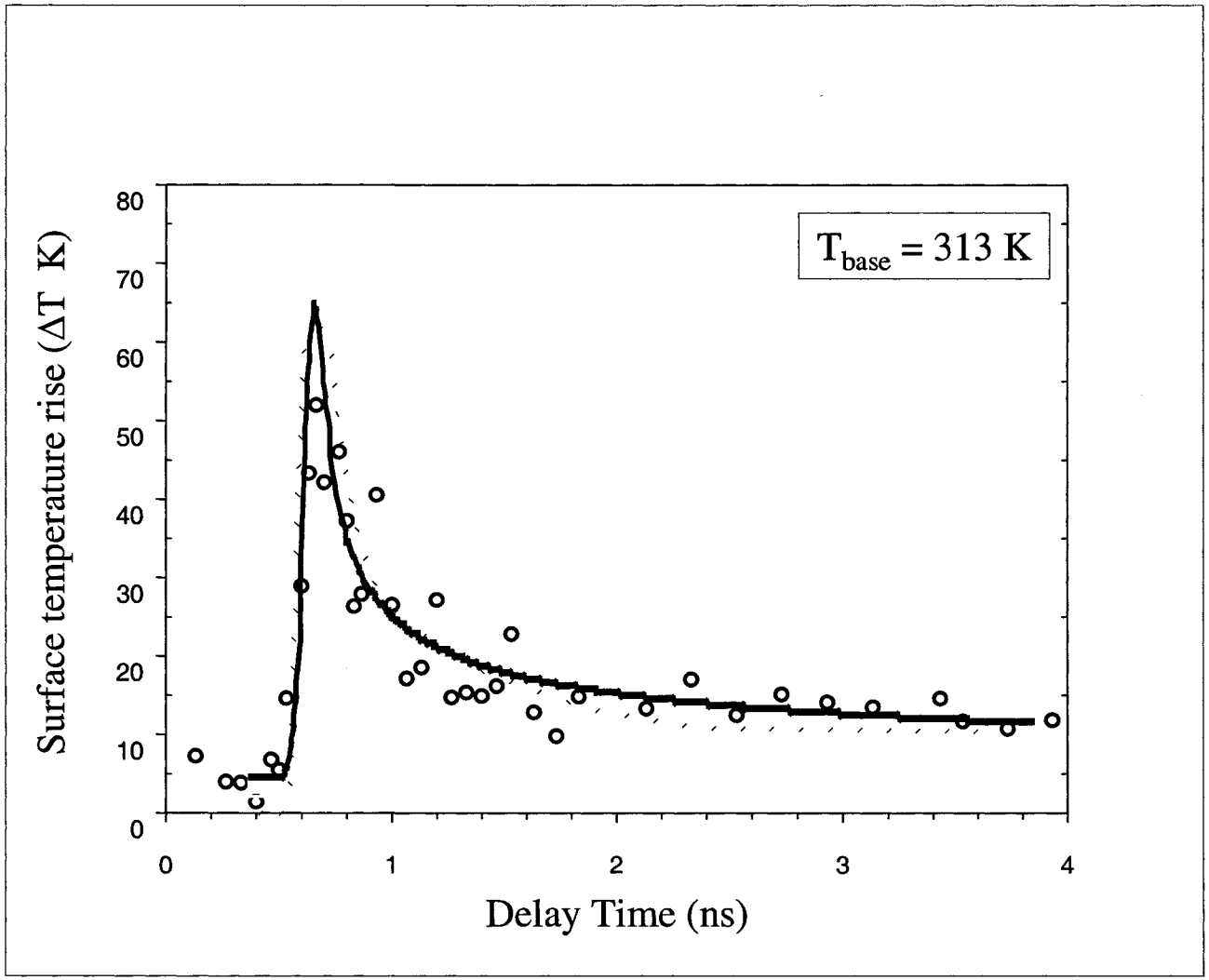

Figure 21. The transient temperature rise of In(111) surface as measured from time-resoved RHEED with FWHM of 100-ps pulse and a peak laser fluence of 0.9×10^8 W/cm^2. The experimental results (open circles) were obtained from the (00) streak. The line curve is the prediction of one-dimensional heat diffusion model. C = 1.726×10^6 J/m^{3}K is the heat capacity; K = 84 W/mK is the thermal conductivity; $\alpha = 9.4\times10^7$ m^{-1} is the absorption coefficient; R = 0.897 is reflectivity at λ = 1.06 μm. I_p is the peak laser fluence in W/cm^2.

exponential decrease vs. base temperature has been measured, as shown in Fig. 22. The duration of 1/e-time is increased with base temperature.

Fig. 23 shows ($I_{laser\text{-}heated}/I_{base\text{-}temp}$) versus delay time t between the heating laser pulse and the electron probe pulse. For T_{base} = 333 K and $I_p = 1.27\times10^8$ W/cm^2 (Fig. 23(a)), when the laser pulse heats the surface a fast decrease in the diffraction intensity is initially observed. This decrease is followed by a rapid intensity recovery as the heat diffuses to bulk. The rise in surface temperature ΔT at $t = t_0$ is ~77 K, causing a peak surface temperature of 410 K, which is below T_m. For Fig. 23(b), we raise the sample temperature on the heated stage to 413 K and use a laser fluence of 1.27×10^8 W/cm^2 to transiently heat the surface. In this case the surface is superheated to a peak temperature of ~ T_m + 60 K. For Fig. 23(c), the surface temperature is raised on the heated stage to 426 K, 4 K below T_m, and a laser fluence of 1.2×10^8 W/cm^2 transiently heats the surface. This is the highest laser fluence that does not cause surface melting at time t_0 at this base temperature. For T_{base} = 426 K and $I_p = 1.34\times10^8$ W/cm^2 (Fig. 23(d)) the maximum superheating temperature is exceeded and the In(111) surface is melted. In this case, the diffraction intensity shows an initial fast rise, similar to that seen in the nonmelting sets. When the maximum superheating temperature is exceeded, melting occurs and the diffraction intensity fails to recover to what is expected from heat diffusion. This lack of recovery of the diffraction pattern lasts for at least several nanoseconds, but the pattern recovers before the next laser heating pulse. The time of recovery depends on the rate of surface recrystallization upon cooling by heat diffusion to the bulk. Measuring this time would require extending the optical delay. We note that even at a laser fluence below 1.2×10^8 W/cm^2 it is expected that some nucleation of melting is occurring particularly in

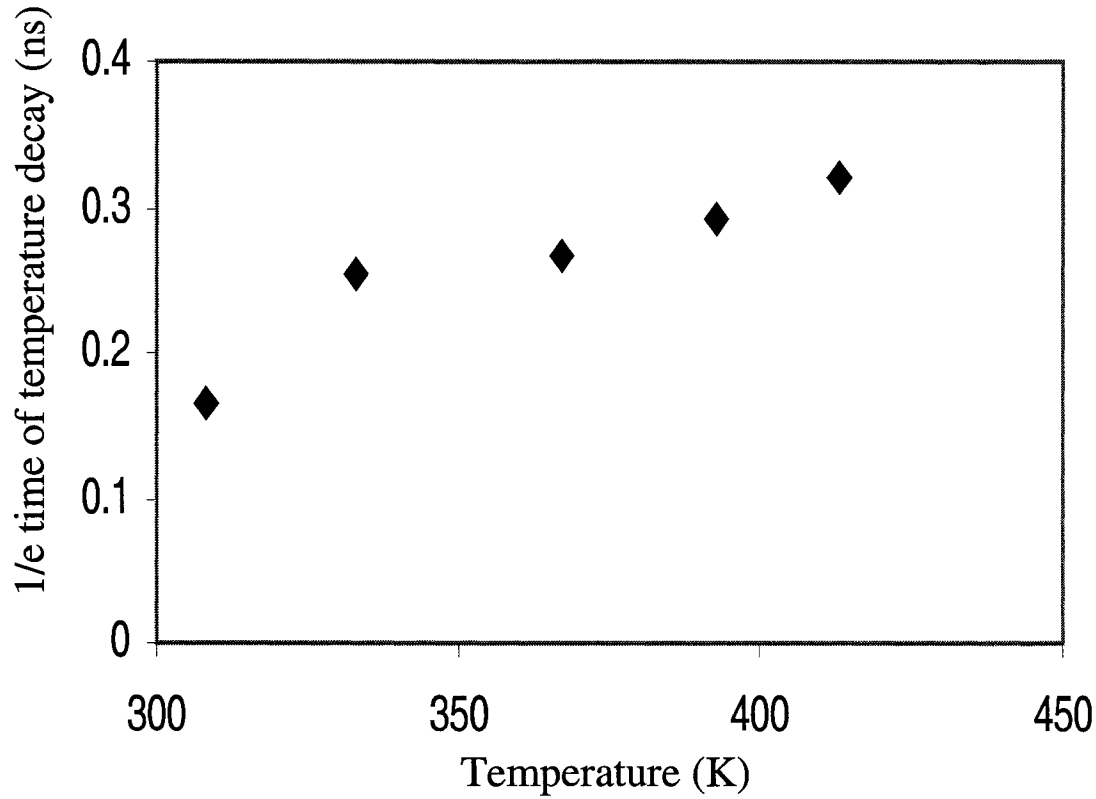

Figure 22. The duration of 1/e time of exponential decay as a function of base temperature obtained from the fitting of the experimental data to one-dimensional heat diffusion model.

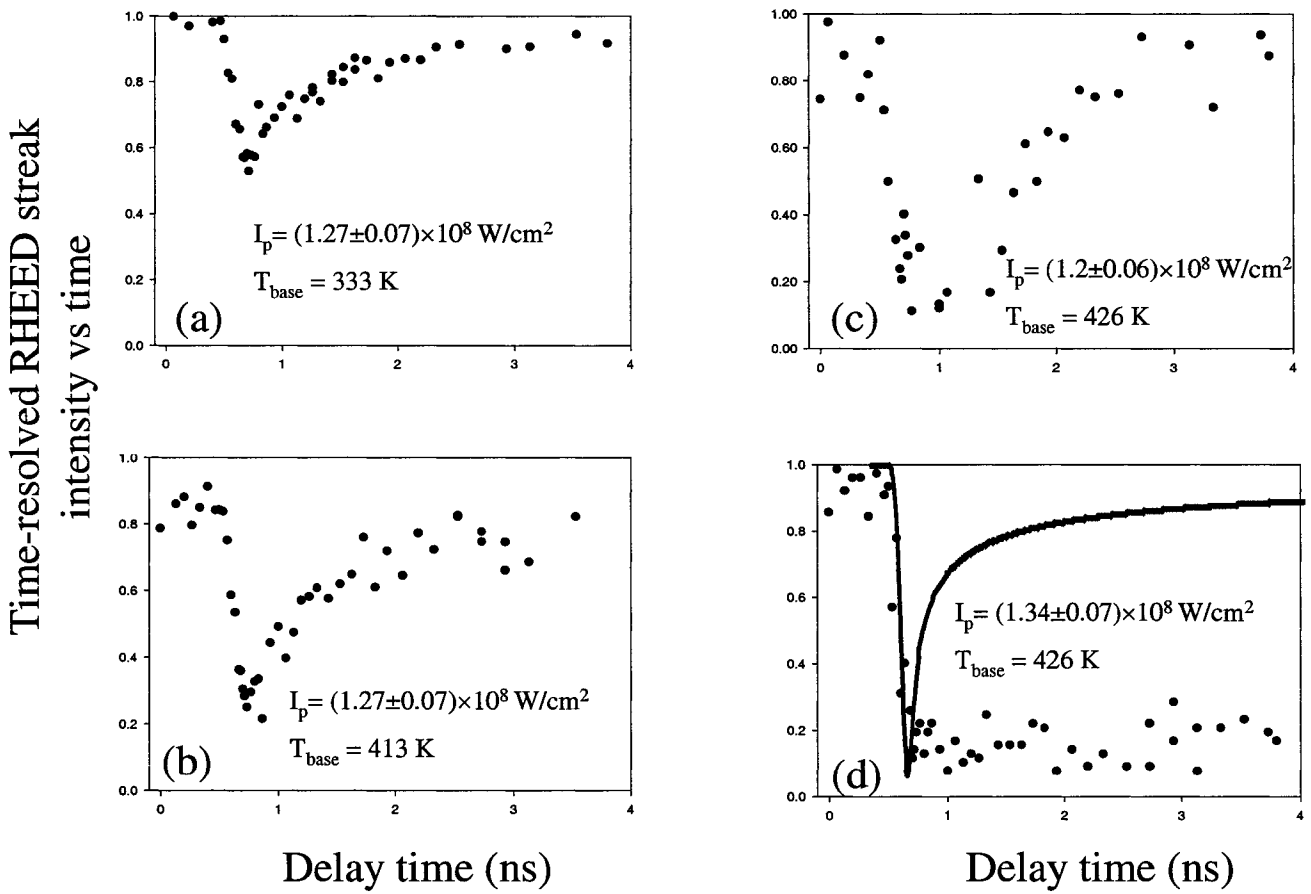

Figure 23. The normalized intensity of time-resolved RHEED of In(111) irradiated with Nd:YAG (λ = 1.06 μm) laser pulses with different base temperature and peak laser fluences. At the temperature jump below the maximum superheating temperature, the behavior is consistent with classical heat diffusion model, (a) - (c). When higher peak laser intensities were applied to the In(111) surface, the surface begins to melt and this is observed in (d) as a deviation from classical heat diffusion.

surface hot spots caused by nonuniformity of the laser spatial profile. This is evident from the increase in the recovery time of the diffraction intensity as the surface temperature is raised. Partial surface melting does not, however, affect the conclusion that most of the surface is transiently superheated at t_0 since the diffraction intensity, at that time, continues to follow Debye-Waller exponential behavior with temperature.

The effect of laser superheating on the surface morphology of the In(111) surface was studied using quantitative RHEED. For these studies we used a 7-kV commercial continuous electron gun with a thermionic emitter. The stronger signal compared to that obtained from the photoactivated electron gun makes it possible to perform quantitative RHEED at high temperatures, where the inelastically scattered electron background in the diffraction pattern becomes large particularly at the out-of-phase condition. The diffraction pattern at an out-of-phase condition was obtained at different azimuths to check for the occurrence of a split peak in the specular beam. A split peak is produced from a vicinal surface with regular monoatomic steps when the electron beam is incident at some angle down the staircase [4.31]. Unlike the vicinal Pb(111) surface [4.37], no split peak in the specular beam was observed at the out-of-phase condition. This indicates that the surface of our In(111) sample does not have regular steps [4.31]. Fig. 24(a) shows intensity profiles of the specular beam taken parallel to the electron beam direction at different temperatures ranging from 304 to 426 K. The solid line is a Lorentzian fit to the data. The diffraction beam profiles parallel and perpendicular to the electron beam direction are well described by a Lorentzian consistent with surface steps that are monatomic in height [4.31]. When temperature is raised the intensity is reduced due to enhanced thermal vibration and surface vacancy generation; in addition the peak of the

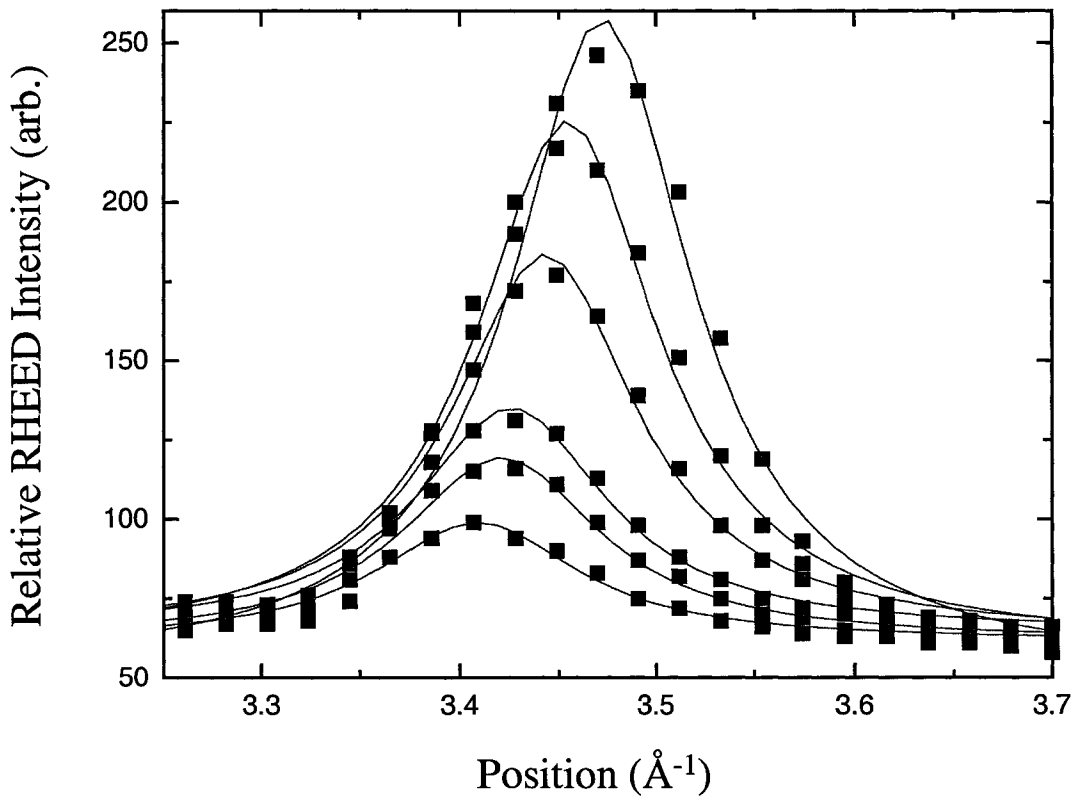

Figure 24 (a). Line profiles of the RHEED specular beam taken along the (00) streak at the out-of-phase condition plotted for sample temperatures of 304, 324, 345, 375, 383, 425 K (solid spots). The peak intensity of RHEED profile is reduced with temperature. The curves are Lorentzian fit to the data.

profile in Fig. 24(a) is shifted towards the shadow edge due to thermal expansion normal to the surface [4.38]. The FWHM of the RHEED profile at the out-of-phase condition remains almost constant with temperature; FWHM = 0.112 ± 0.008 $Å^{-1}$ at 304 K and 0.118 ± 0.016 $Å^{-1}$ at 426 K. This indicates that the average surface random step terrace width does not change noticeably with temperature, as shown in Fig. 24(b). Figure 25 shows the out-of-phase thermal expansions from the position shift of the (00) RHEED streaks at temperature range from 304 K to 425 K. The results show that the thermal expansion coefficient of the In(111) perpendicular to the surface is 3.17%, compare with 0.4% for the bulk indium over the same temperature range. Therefore the surface thermal expansion perpendicular to the surface of In(111) is about 8 times larger than that of the bulk.

Based on kinematic diffraction theory, when a two-dimensional surface has only vacancies, the background intensity increases with the vacancy density without broadening the diffraction profile [4.31, 4.37, 4.39 and 4.40]. Fig. 26 shows the dependence of the ratio $R = I_{back}/(I_{peak}-I_{back})$ on temperature. Here, I_{peak} is the intensity of the specular spot in the out-of-phase condition, while I_{back} is the background intensity measured between the (00) and (01) streaks also in the out-of-phase condition. The ratio R is related to vacancy density by $R \propto [(2n-1)^{-2}-1](1+2M)$ at the out-of-phase condition, where n is the surface vacancy density and 2M = wT is the Debye-Waller factor [4.31, 4.37, 4.39 and 4.40]. Therefore, the vacancy density is given by $n \propto (1/2)[R/(1 + 2M) + 1]^2 + 1/2$. We obtain w = 0.0144 K^{-1} from the Debye-Waller curve of Fig. 19. The vacancy density change is $\Delta n = n/n_{initial}-1$, where n is the surface vacancy density at some temperature and $n_{initial}$ is the initial surface vacancy density before heating. From Fig. 26,

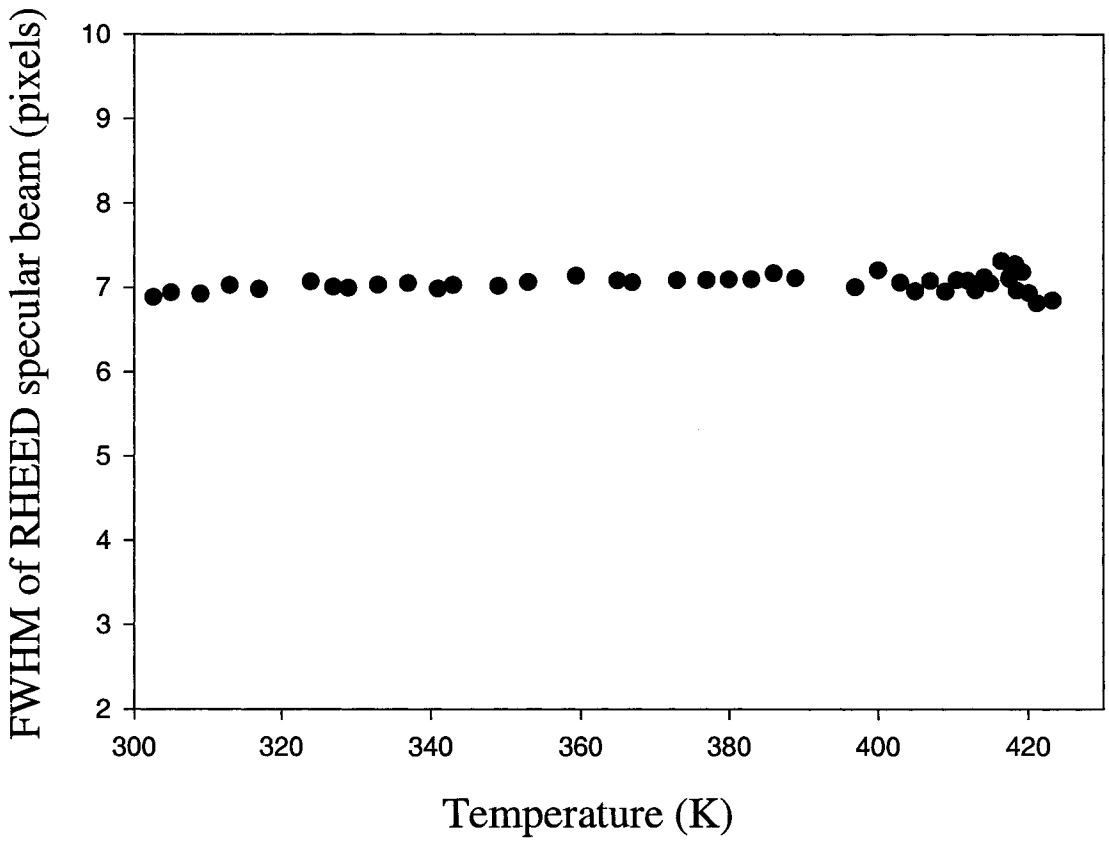

Figure 24(b). FWHM of the RHEED profile at the out-of-phase condition is plotted as a function of temperature. The incident angle of the electron beam was 3.2°, which is at the out-of-phase condition.

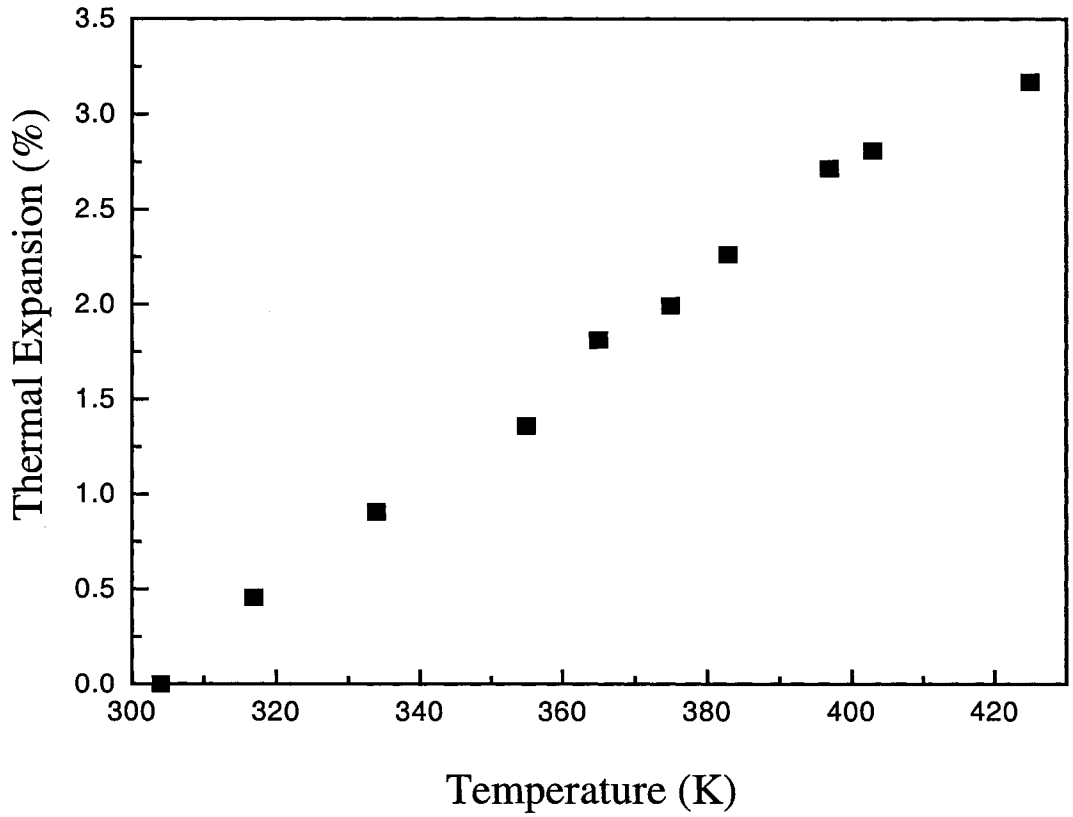

Figure 25. The thermal expansion normal to the In(111) surface derived from the measurement of the RHEED streak shift. The coefficient of linear thermal expansion is $32.1/K^{-1}*10^6$ for bulk indium [4.44]. Therefore the thermal expansion coefficient of bulk indium over temperature 304-425 K is 0.4 %, compared with the surface coefficient of thermal expansion of 3.17 %.

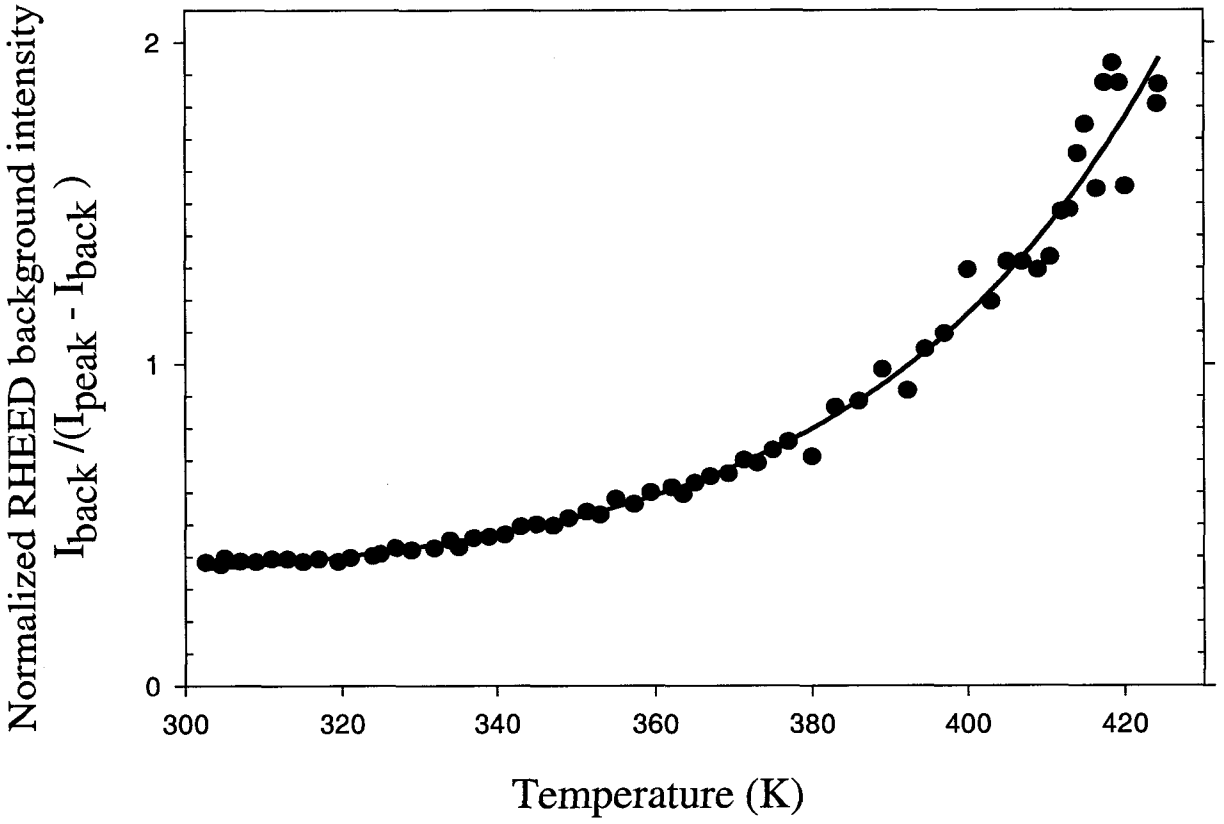

Figure 26. When the temperature is raised, an increase in the RHEED background is observed. The increase in the ratio $I_{back}/(I_{peak} - I_{back})$ measured at the out-of-phase condition indicates an increased surface vacancy density.

we calculate a surface vacancy density increase of ~ 22% when the temperature is raised from 300 to 426 K. When Fig. 26 is converted into relative vacancy density versus temperature, a one exponential curve does not fit the data. Using low-energy-electron diffraction, thermal disordering of the In(100) and In(110) surfaces was previously studied [4.32]. In(100) was found to remain solid up to T_m. In(110), however, does not show surface roughening at high temperatures, but disorders due to a transition from large surface anharmonic vibrations to a quasi-liquid state via increased density of vacancies and adatoms. For In(111), some vacancy and adatom creation on the solid surface are observed, Fig. 26, but no step roughness is detected, Fig. 24(b). The In(111) surface is observed to remain solid with the surface atoms vibrating in what appears as a harmonic Debye-Waller manner up to the highest studies temperature in slow heating, T_m - 4 K. Vacancy creation when heating from 300 to 426 K leads us to believe that surface atom vibration is somewhat anharmonic; however, this anharmonicity is not detected in the Debye-Waller curve of Fig. 19, which is obtained at an in-phase condition. The lack of observation of anharmonic behavior in Fig. 19 could be explained by its small value; thus, it is within the experimental error. For In(111) the surface vacancy density increased by ~ 22% when the temperature is raised from 300 K to near its T_m, while in a previous study of Pb(100) the vacancy density increased by ~ 300% with some deviation from exponential behavior apparent in the specular beam intensity versus temperature at the in-phase condition [4.37].

The interpretation of the above data relies totally on kinematic treatment which is known to be inadequate to describe the diffraction intensity [4.41, 4.42 and 4.43]. Precise analysis of the diffraction pattern requires dynamical treatment that includes multiple

scattering and surface and bulk resonances. Dynamical effects are not expected to affect the conclusion of surface superheating because that conclusion is simply based on the observation of the laser-induced surface temperature at which deviation from Debye-Waller behavior is observed. If dynamical effects were significant, then the observed temperature dependence of the specular beam intensity in the in-phase condition (Fig. 19) would have deviated from exponential. For surface defect measurements, performed at the out-of-phase condition, the validity of quantitatively interpreting diffraction intensities could be affected by not accounting for dynamical effects. However, these do not affect the conclusion that when heating In(111) from room temperature to near T_m the surface step density remains almost unchanged with some increase in vacancy density.

In a MD simulation of the structure of laser heated Cu(110) and Cu(111), the superheating of Cu(111) was observed for laser heating conditions that lead to melting of Cu(110) [4.44]. A Cu(111) surface with high vacancy and adatom concentration was shown to anneal during laser superheating by a mechanism in which the adatoms settle in the top layer occupying vacancy sites [4.44]. To measure the effect of laser superheating on surface defect density on In(111), the RHEED background intensity was observed after subjecting the surface to different laser fluences. The surface was raised to a base temperature of 426 K using the heating stage while the 100-ps pulsed laser transiently heated it. Figure 27 shows the measured ratio $R = I_{back}/(I_{peak}-I_{back})$ at the out-of-phase condition as a function of peak laser fluence after heating with 1000 laser pulses at 50 Hz repetition rate at each fluence. The ratio R does not change for $I_p < 1.2\times10^8$ W/cm^2. Above that fluence, the ratio R begins to increase indicating a slight increase in the

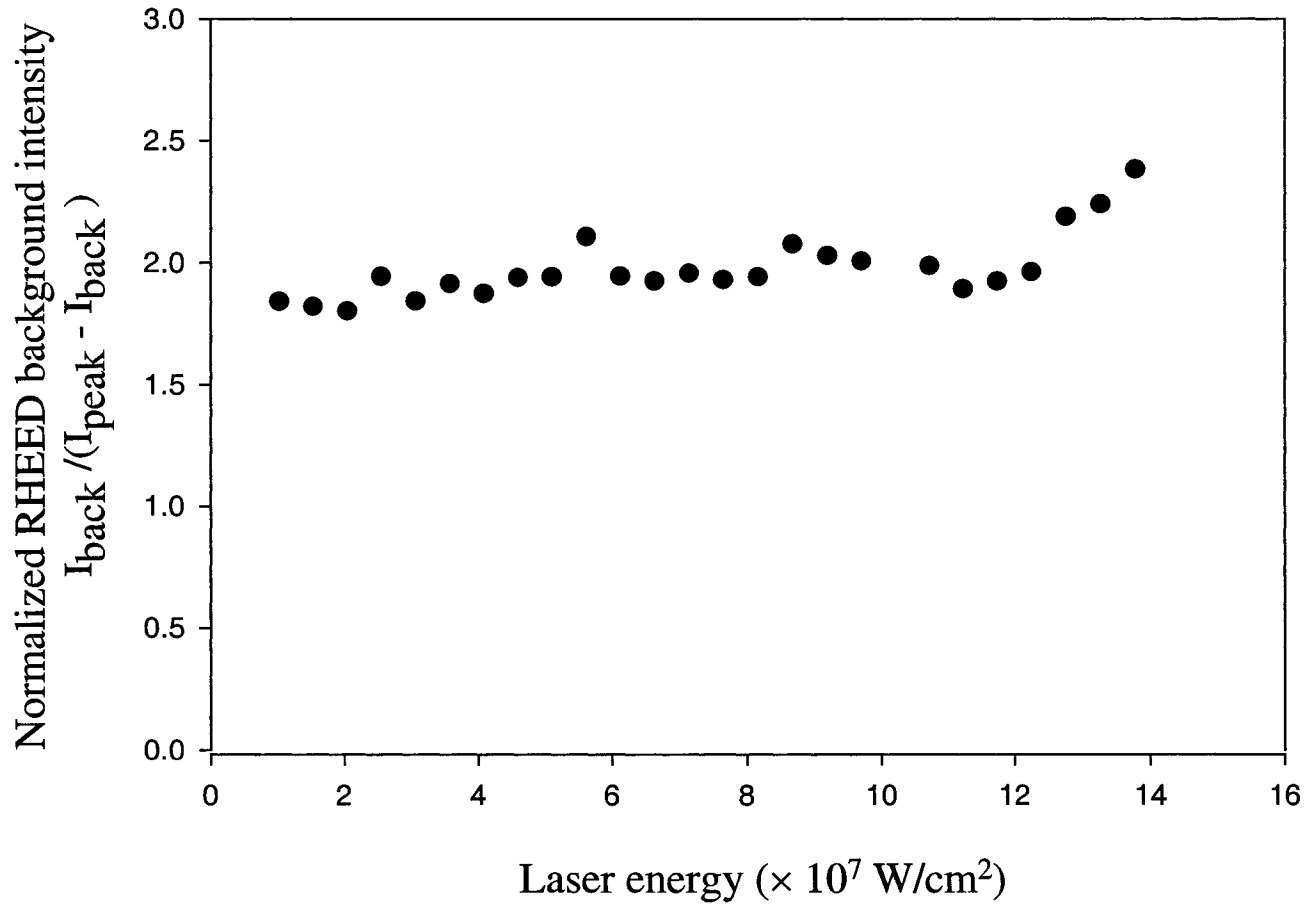

Figure 27. The changes of the ratio R = $I_{back}/(I_{peak}-I_{back})$ as a function of peak laser fluence at out-of-phase condition. The In(111) was based at 426 K while 100-ps pulsed laser was used to transiently heat the indium surface. The total of 1000 pulses was used at each data. The ratio R remains unchanged below a peak laser fluence of 1.2×10^8 W/cm^2. Above that fluence, R begins to increase.

surface vacancy density. No change is observed in the FWHM of the specular beam profile parallel or perpendicular to the [110] electron beam incidence direction, when measured at the out-of-phase condition, indicating that the surface step density does not change after laser heating. The results show that laser superheating of the studied In(111) surface does not anneal surface vacancies. The slight increase in vacancy density after the maximum superheating laser fluence is exceeded ($>1.2\times10^8$ W/cm^2) is thought to be due to fast quenching of the melted layer by rapid heat diffusion to the bulk. Similar surface damage after melting was observed for Pb(100), although annealing by surface melting subsequent to superheating was observed for Pb(111) [4.37].

4.4. Conclusion

The high temperature behavior of the In(111) surface was investigated using conventional and 100-ps time-resolved RHEED. For slow heating, In(111) remains solid up to the highest temperature studied, T_m - 4 K. Transient superheating of In(111) by 100-ps laser heating is observed up to T_m + 73±9 K. Raising the surface temperature above the maximum transient superheating temperature results in RHEED intensity reduction from that expected from Debye-Waller behavior. The transient surface superheating could be somewhat higher than stated above because we do not consider convolution effects since the electron probe pulse width is about equal to the laser heating pulse width. Because of the fast change of RHEED intensity near its peak reduction, this effect tends to reduce the maximum temperature measured. With temperature rise, an increase in vacancy density on In(111) is observed with no noticeable change in the FWHM of the RHEED profile at the out-of-phase condition indicating that the random

step terrace width does not change with temperature. Transient superheating of the In(111) surface with a laser fluence below the melting threshold does not change the surface morphology.

Chapter V

REFLECTION HIGH-ENERGY ELECTRON DIFFRACTION STUDY OF SURFACE MORPHOLOGY OF VICINAL Au(110) THROUGHOUT THE (1x2) DECONSTRUCTION PHASE TRANSITION

5.1. Introduction

It is well known that the fcc(110) surfaces of transition elements reconstruct to give diffraction patterns indicative of a missing row (MR) [5.1]. The Au(110) surface undergoes a reversible (1x2) MR reconstruction with the clean configuration of Au(110) at room temperature (1x2) reconstructed. With heating, Au(110) undergoes a (1x2) to (1x1) phase transition which is associated with, or followed by, a roughening transition below the melting point [5.2, 5.3].

The reconstruction of Au(110) was studied by low-energy electron diffraction (LEED) [5.4], ion scattering spectrometry (ISS) [5.5], x-ray diffraction at grazing incidence [5.6, 5.7], high-resolution electron microscopy (HREM) [5.8], scanning tunneling microscopy (STM) [5.9-5.12], He atom beam scattering [5.13], and scattering and recoiling imaging spectrometry (SARIS) [5.14]. The Au(110) surface shows a (1×2) MR reconstruction at room temperature. Upon heating, the half-order diffraction spots begin to fade, and the pattern reverts to (1×1) in the temperature range between 650 K and 735 K [5.7, 5.13, 5.15-5.17]. The Au(110) MR reconstruction is believed to belong to the 2D Ising universality class based on the critical exponents evaluated at the (1x2) to

(1x1) transition temperature [5.1, 5.18]. Several structural models for this transition has been proposed [5.1, 5.19]. In addition, the observed surface relaxation has attracted interest and the results are controversial. While, high-resolution electron microscopy and early x-ray study showed an expansion of the top-layer spacing [5.8, 5.20], other experiments provided strong evidence of contraction of the top-layer spacing [5.21-5.24].

When the surface temperature of Au(110) is increased to the (1x2) to (1x1) transition temperature and above, the Au(110) surface roughens. Other fcc(110) surfaces have also shown a 3-D roughening transition at temperatures well below the bulk melting point [5.19]. The roughening transition was first observed in experiments on ^{4}He crystal growth [5.25], but has also been found to occur on several metal surfaces. A typical Au(110) surface has steps even at low temperatures. If the step-step interactions repel each other, the ordered phase is stable. If the surface temperature is increased and the interaction is not too strong, entropy is gained by increasing the number of steps leading to surface roughening at a temperature T_R, lower than the surface melting temperature. Villain and Vilfan in their calculation [5.26], found that the roughening transition occurs approximately 100 K higher than the Ising transition in Au(110). The Au(110) roughening transition was studied by x-ray diffraction [5.7] and thermal-energy ion scattering [5.17]. The roughening transition temperature T_R lies between 752 and 784 K as measured by Keane *et al.* [5.7]. The Ising transition occurs around 650 K and the roughening transition occurs around 690 K [5.17].

Several structural models of this Ising transition have been proposed. Campuzano *et al.*, in a Monte Carlo simulation predicted that Au(110)-(2x1) undergoes a continuous order-disorder phase transition characterized by random distribution of the topmost (1×2)

atoms to sites between the original and missing-row sites [5.27]. Villain and Vilfan pointed out that surface roughening should play a role in the transition in which the 2-D order-disorder transition is characterized by random distribution of the top reconstruction layer and step excitations [5.26]. When step-step interactions are strong, the surface undergoes an Ising transition and at higher temperatures a roughening transition, while for weak interactions both deconstruction and roughening occur at the same temperature. Den Nijs's introduced a chiral four-state clock-step model to describe deconstruction and roughening of MR fcc(110) facets [5.2]. According to this model, surface roughening induces a simultaneous deconstruction which for weak chirality, such as proposed for Au(110), shows both Ising and conventional roughening critical exponents. The transition has a character of a Kosterlitz-Thouless-type roughening superimposed on an Ising deconstruction [5.2].

Sturmat *et al.*, investigated the roughening and deconstruction transition of Au(110) by STM [5.10]. They found that the missing row structure is stable up to the roughening temperature. The disorder processes preceding the roughening transition were confined to step edges, while the missing row configuration on terraces and at step edges remained stable up to the roughening transition. More recently, Rost and Frenken concluded that STM measurements of surface roughness of Au(110) are affected by the high mobility of atoms at step edges and that STM speeds down to the ms range is needed to observe the roughening and deconstruction transition [5.12]. They concluded that Sturmat *et al.* did not observe the atomic scale mechanism of the roughening and deconstruction transition. Höfner and Rabalais studied the Au(110)-(1×1) surface using variable temperature scattering and recoiling imaging spectroscopy (SARIS) [5.14]. They

also claimed that the theoretical model of an order-disorder transition via lattice gas formation is invalid. The basic features of the missing row reconstruction were observed near 700 K where the roughening transition begins. SARIS is sensitive to short-range order of the surface, for instance, <10 Å.

We report on a study of surface deconstruction and roughening on a stepped Au(110) surface using reflection high energy electron diffraction (RHEED). The reconstruction and deconstruction of Au(110) were observed. Although LEED has been extensively used to measure critical parameters of phase transitions, using RHEED to measure critical parameters is not common. We apply temperature-dependent RHEED intensity and profile measurement in the in-phase condition to estimate some critical parameters of the deconstruction phase transition. The surface atomic mean vibrational amplitude of Au(110) perpendicular to the surface is also obtained. Analysis of the RHEED intensity profile at the out-of-phase condition gives the average surface step terrace size [5.28-5.30]. Changes in the step terrace width are observed as changes in the RHEED intensity profile [5.28-5.30]. The results suggest that changes in surface step density and step edge roughness accompany surface deconstruction. Surface relaxation at room temperature is obtained from the RHEED rocking curve and compared to previous measurements. In addition to clarifying the nature of surface roughening during the Au(110) deconstruction transition, the present kinematic RHEED interpretation of a well-studied surface phase transition provides data to further explore the validity and limitations of the kinematic approach.

5.2. Experimental methods

The experiment was performed in an ultrahigh vacuum chamber equipped with a RHEED system and Ar^+ sputtering. The details of the system were described previously [5.30-5.33]. The base pressure was in the low 10^{-10} Torr. The electron beam energy used for RHEED was 9 keV. This relatively low energy allows the use of grazing angles of 1° to 5°, while still maintaining high surface sensitivity. The RHEED pattern, displayed on a fluorescent screen, is recorded using a charge coupled device (CCD) camera interfaced to a computer for subsequent analysis. The sample was a 2-mm thick, 6-mm diameter single crystal grown from gold of 99.999% purity and cut to expose the Au(110) surface with misalignment less than 1° as characterized by the manufacturer and verified by our RHEED measurement of the average terrace widths. The surface was polished to mirror finish. Cycles of (1-1.5)-keV Ar^+ bombardment were used to sputter clean the surface at room temperature followed by annealing at 450 °C for 20 hours. The reconstructed Au(110)-(1×2) structure was clearly observed in the RHEED pattern after annealing. In order to obtain accurate temperature measurement, a type-K thermocouple was placed between the retaining clip and the surface of the Au crystal. The distance between the thermocouple and the position that the electron beam strikes the surface was less than 3 mm. The thermocouple and the temperature controller were precisely calibrated at the freezing and boiling temperatures of water. The temperature uncertainty was estimated to be within ±3 K, and temperature stability within ±1 K was attained using a temperature controller. During the experiment, Ar^+ bombardment and annealing treatments were repeated periodically.

5.3. Results

5.3.1. Surface relaxation

Figure 28(a) is a RHEED pattern taken at 310 K of the Au(110) surface after cleaning. The (1×2) structure was obtained with the 9-keV electron beam incident along the [001] direction. Figure 28(b) is a (1×1) RHEED pattern obtained at 670 K, just above the (1x2) deconstruction phase transition temperature. The half-order streaks are clearly visible in Fig. 28(a). Upon heating, the diffraction pattern intensity decreases due to enhanced surface mean vibrational amplitude and the half-order streaks disappear at ~ 650±10 K indicating the loss of long range order in the (1x2) structure [5.21-5.23].

As an initial step to characterize the structure of the Au(110) surface, a RHEED rocking curve was obtained at room temperature. Early studies using x-ray scattering [5.24] and LEED [5.21] indicated a contraction of the top two atomic layers by approximately 32% and 29%, respectively. Low and medium energy ion scattering studies showed a smaller contractions of ~ 20-26% [5.22, 5.23]. However, direct imaging by high-resolution electron microscopy (HREM) indicated an expansion of the topmost layer spacing by 20±5% [5.8], and an x-ray diffraction studied concluded that the top two atomic layers are expanded by 40±30% of the bulk-terminated structure [5.20]. In our experiment, the rocking curve of the clean Au(110) surface was obtained at room temperature with the 9-keV electron beam incident along the [001] direction, as shown in Fig. 29. The top layer spacing can be obtained from the rocking curve. Two peaks are present in Fig. 29, which correspond to the in-phase condition of m = 1 and 2, respectively. The measured angle for the m = 1 Bragg condition is $\theta_1 = 2.6^\circ$, which is bigger than the calculated bulk-terminated angle of $\theta_1 = 1.6^\circ$. An inner potential of 5.51

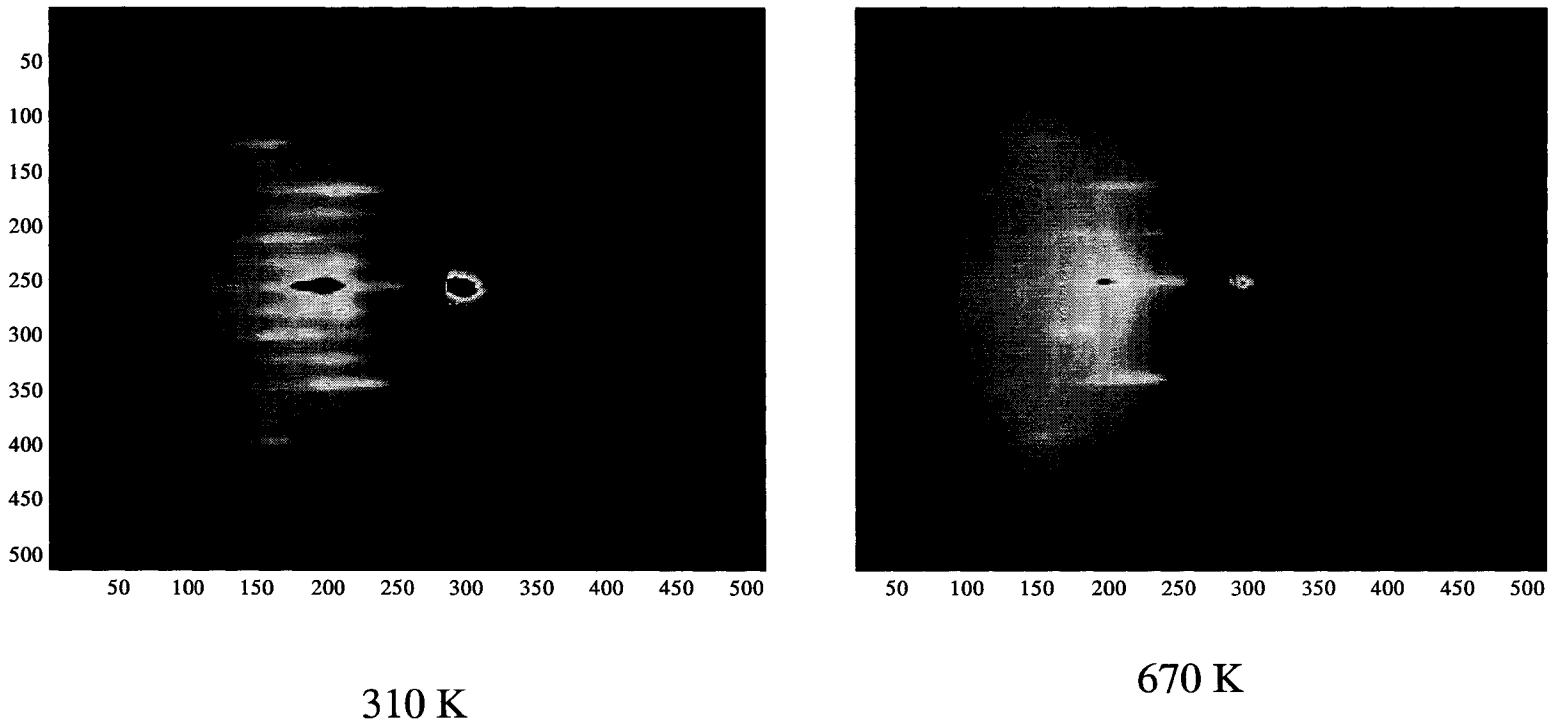

Figure. 28. (a) RHEED pattern of Au(110) taken at 310 K shows the (2×1) reconstruction. (b) RHEED pattern of Au(110) at 670 K shows (1×1) structure. The 9 keV electron beam was incident along the [001] azimuth at an angle of ~ 2.8° from surface.

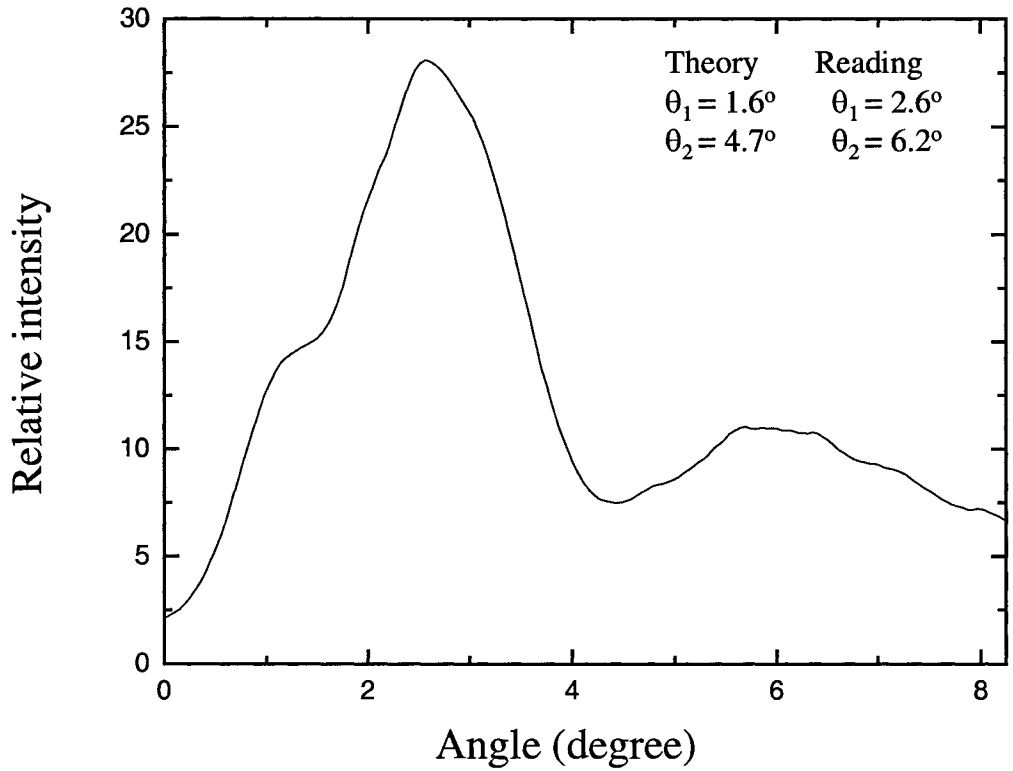

Figure. 29. Rocking curve of RHEED specular beam intensity of the Au(110)-(2x1) surface obtained at room temperature. The electron beam is incident along the [001] direction. The two peaks, at $\theta_1 = 2.6^o$ and $\theta_2 = 6.2^o$, correspond to the in-phase condition for m = 1 and m = 2, respectively.

eV was used in the calculation [5.34]. This indicates that the interlayer distance between the top layer and the second layer is contracted by 0.31 ± 0.03 Å or ~ 22%; in agreement with low and medium energy ion scattering results [5.22, 5.23]. The Bragg condition of m = 2 is at $\theta_1 \sim 6.2^\circ$ compared to a calculated value of 4.7° for a bulk-terminated structure resulting in an estimated ~ 0.3 Å contraction, although the lattice spacing obtained from m = 2 peak is not reliable because of the broad nature of that peak.

5.3.2. Surface Debye temperature

To characterize the temperature dependence of the Au(110) surface structure, the RHEED streak intensity versus temperature was measured. The electron beam was incident along the [001] azimuth at an angle of ~ 2.6° from the crystal surface (in-phase condition m = 1), resulting in a probed depth of ~ 3 Å, corresponding to the top two layers of Au(110). Results are shown in Fig. 30, where the RHEED specular beam intensity is normalized to that at 308 K and plotted in semilogarithmic scale. The specular beam intensity versus temperature curve exhibits an exponential Debye-Waller extinction with temperature, $exp(-2MT)$, where $2M$ is the Debye-Waller factor. From the slope, a Debye temperature of 65±6 K is measured compared to a bulk Debye temperature of Au, θ_{Dbulk} = 170 K. Above ~730 K, the intensity measurement shows increased data scattering off the Debye-Waller fit which is related to surface roughening discussed below.

The intensity versus temperature of the (0,1/2) order from the reconstructed Au(110)-2x1 is also observed along with the specular peak in Fig. 30. The intensity of the (0,1/2) order also shows an exponential Debye-Waller extinction, $exp(-2MT)$ at temperatures lower than the (2x1) to (1x1) transition. However, the Debye temperature calculated from the (0,1/2) order is 43±4 K. The solid line fit to the (0,1/2) intensity is

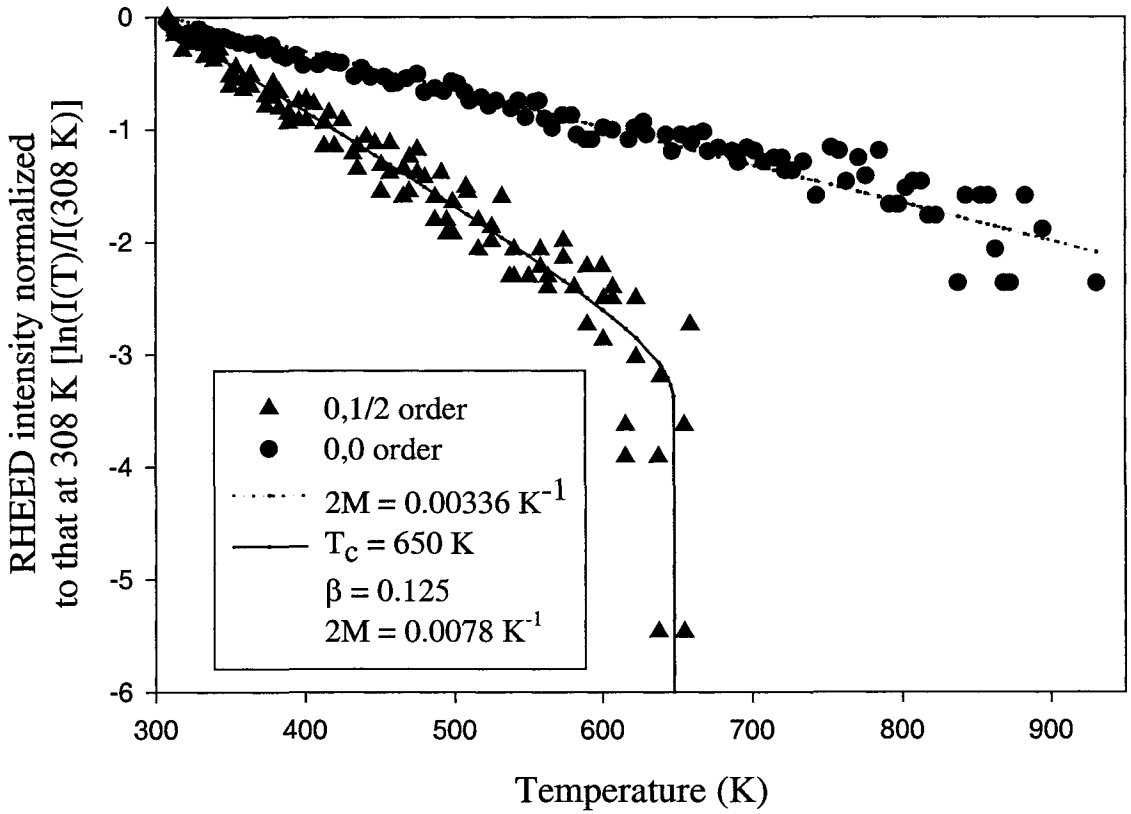

Figure. 30. RHEED beam intensity of (0,1/2) (triangles) and (0,0) (circles) orders of the Au(110) surface normalized to that measured at 308 K versus temperature. The dotted line is a Debye-Waller fit to the intensity of the (0,0) order. The solid line is a fit to the intensity of the (0,1/2) order that includes attenuation due to Debye-Waller effect and the phase transition at T_c = 650 K.

obtained as discussed in Section 5.3(c). The surface Debye temperature is a measure of the mean vibrational amplitude and is given by $\theta_{Dsurface} = [3\,\hbar^2 T/Mk_B\langle x^2\rangle]^{1/2}$, where $\hbar$ is Planck's constant, k_B is Boltzmann's constant, M is the atomic mass, and $\langle x^2\rangle$ is the projection of the mean square vibrational amplitude of surface atoms along the electron momentum transfer Δk [5.35]. In the RHEED geometry, for the specular beam, Δk is mainly normal to the surface. The lower Debye temperature obtained from the (0,1/2) order compared with that obtained from the specular beam, indicates that the top layer of in the (1x2) structure has a mean vibrational amplitude higher than the (1x1) layer underneath it. We calculate the surface vibrational amplitude from the specular beam $\sqrt{\langle x^2\rangle}$ = 0.24 Å and 0.35 Å at 300 K and 635 K, respectively, while those calculated from the (0,1/2) order are 0.36 Å and 0.52 Å at 300 K and 635 K, respectively. These values are higher than those used in simulating the variable temperature images obtained by scattering and recoiling imaging spectrometry (SARIS) [5.14], and could be one of the reasons why the SARIS experimental images are broader than the simulated images. The intensity of the (0,1/2) spot disappears as the surface temperature is raised above 650±10 K, indicating surface deconstruction in agreement with previous experimental results [5.21-5.24]. The phase transition is continuous and reversible.

5.3.3. Critical parameters

It is well known that order-disorder transitions on surfaces fall into a few classes characterized by their critical properties [5.36]. Near such an order-disorder equilibrium phase transition, all thermodynamic quantities scale according to the power laws of reduced temperature $t = (T_c - T)/T_c$. Close to the transition temperature, the diffraction

intensity for momentum transfer $\boldsymbol{q}$, close to the reciprocal lattice vector $\boldsymbol{q_0}$ can be written as

$$I(q,t) = \rho^2(t)\delta(\boldsymbol{q} - \boldsymbol{q_0}) + \chi(\boldsymbol{q} - \boldsymbol{q_0},t), \quad (5.1)$$

where ρ stands for the order parameter and the first term represents the Bragg peaks due to long-range order, whereas, the second term accounts for critical scattering due to correlations in short-range order fluctuations [5.37, 5.38]. The order parameter ρ varies at T_c as $\rho \sim t^{\beta}$, while short-range order fluctuations vary as $\chi \sim |t|^{-\gamma}$. Thus, for the superstructure peaks above T_c, only the second term contributes to diffraction intensity and determines the peak shape. The correlation length diverges at T_c as $\xi \sim |t|^{-\nu}$. The theoretical critical exponents for the Ising universality class are $\beta = 1/8$, $\gamma = 7/4$, and $\nu = 1$ [5.38].

To check if the RHEED intensity can give information on the class of this phase transition, the intensity of the (0,1/2) order beam measured at various temperatures was fit to:

$$I(T) = I(0)\, t^{2\beta}\, exp(-2MT), \quad (5.2)$$

where $t^{2\beta}$ gives the dependence of long-range order on the reduced temperature t, and $exp(-2MT)$ accounts for the Debye-Waller reduction in intensity. The solid line is a solution of Eq. (5.2) with $\beta = 0.125$, phase transition critical temperature $T_c = 650$ K, and Debye-Waller factor $2M = 0.0078$ K^{-1}.

The exponent ν in the correlation length can be estimated from the fractional order beam profile with temperature measured above the critical temperature T_c. Ideally, the Lorentzian contribution to correlation length fluctuations should be deconvolved from the Gaussian instrumental broadening of the diffraction peak. However, due to the small

beam divergence, the maximum (0,1/2) order angular spread in a direction perpendicular to the surface was only ~ 0.2^{o} making precise determination of the (0,1/2) order profile not possible. The full-width at half-maximum (FWHM) of the (0,1/2) order and (0,1) order are plotted in Fig. 31. The results show significant scatter due to the limitations in the accuracy of the instrumentation. However, the FWHM of the (0,1/2) order clearly increases above T_c, while that for the (0,1) order remained unchanged. The FWHM was obtained from the RHEED pattern using a Lorentzian curve fit to the intensity profile of each RHEED order. The solid line is a fit to the equation $FWHM \sim |t|$ for temperature higher than the estimated critical temperature $T_c = 650$ K.

We note that the above analysis of the data to estimate critical parameters is limited by the kinematic treatment. It has been shown previously that, for low-energy electron diffraction, kinematic analysis of peak intensities can lead to large enough errors to prevent clear assignment of the phase-transition to a known universality class [5.39]. The reason behind this is that the intensity of the diffuse scattering includes effects due to statistical fluctuations in order in addition to fluctuations in the scattering amplitudes. When multiple scattering is important, the scattering amplitude of identical atoms depends on their location. Changes in the density of domain boundaries during the phase transition, cause changes in the effective scattering amplitudes. The large RHEED background at the phase transition temperature prevented us from obtaining an estimate of the critical parameter γ. Further developments in the RHEED technique that could include energy-filtered diffraction acquisition and dynamical analysis are needed for accurate determination of critical parameters.

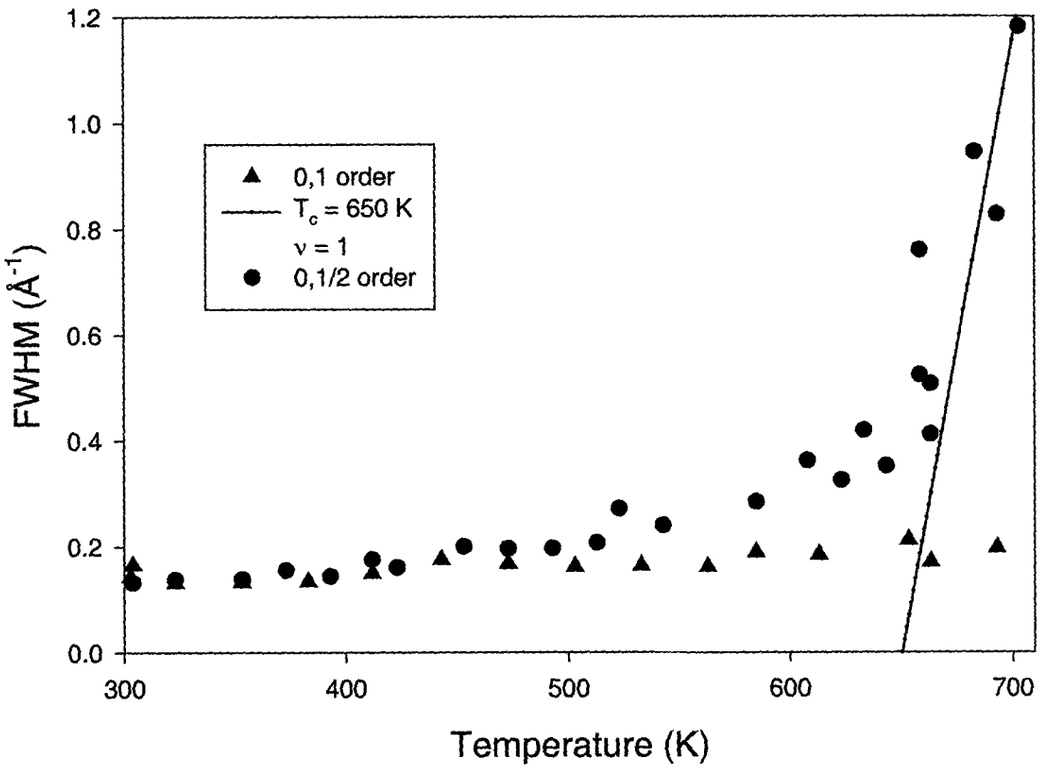

Figure. 31. The FWHM of the (0,1) order and (0,1/2) order plotted as function of surface temperature. The solid line is a fit to the equation $FWHM \sim |t|$. for temperatures higher than the estimated critical temperature $T_c = 650$ K.

5.3.4. Surface roughening

Lineshape and intensity analysis of the Au(110) RHEED patterns at an out-of-phase condition were investigated at different temperatures in order to study surface defects. Figure 32(a) is a RHEED pattern taken at the out-of-phase condition at room temperature with the 9-keV electron beam incident along the [001] direction. The angle of incidence of the electron beam was ~ 4°, corresponding to an out-of-phase condition as shown in Fig. 29, in which the (00) beam profile is most sensitive to surface steps and vacancies. Figure 32(b) is a three-dimensional RHEED intensity profile. The probed depth is ~ 4 Å, which corresponds to the top 2-3 layers. A splitting specular peak was observed and had a maximum splitting along the [001] direction of the Au(110) surface. This indicates that the surface is vicinal [5.28] with the step edge perpendicular to the $[1\bar{1}0]$ direction. Thus, the electron beam was incident at a direction down the surface staircase. Lineshape analysis of the (00) peak at an out-of-phase condition can be used to obtain the average terrace width and string length at terrace edges. The terrace width is defined as the distance of a flat surface between an up and a down pair of steps. The string length is the length of a straight line of atoms at a step edge, bounded by an up and a down atomic step at a step edge [5.28]. The spacing between the two splitting peaks along the [001] direction is measured to be 0.075 $Å^{-1}$. Taking into account the instrumental response of 0.023 $Å^{-1}$, measured from the specular peak profile in the $m = 1$ in phase condition, the vicinal terrace width of the studied Au(110) surface is obtained to be 120 Å at room temperature, corresponding to a miscut angle of 0.5°. The instrumental response is obtained from the full-width at half-maximum (FWHM) of the (00) beam at the in-phase condition [5.28, 5.40]. The intensity profile perpendicular to the [001]

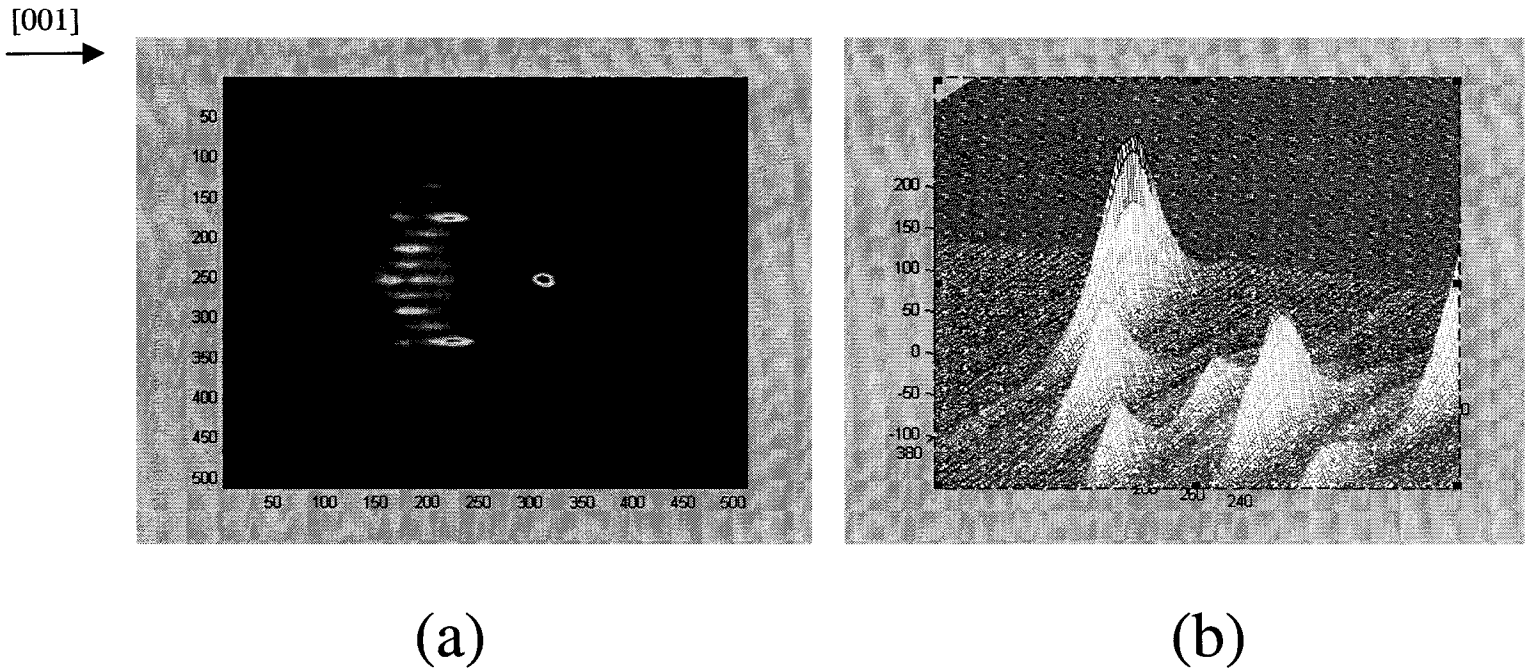

Figure. 32. (a) RHEED pattern from Au(110)-(1×2) surface at room temperature with an electron energy of 9 keV incident along the [001] direction. The angle of incidence of the electron beam is ~4°, corresponding to the out-of-phase condition. The average vicinal terrace width on Au(110) at room temperature is 120 Å. The average string length at vicinal step edge at room temperature is more than 280 Å. (b) Three-dimensional view showing the relative intensities of the diffraction peaks.

direction at the out-of-phase condition gives information on kinks and meanders at the step edge. Fitting the intensity profile of the (00) beam to a Lorentzian, A FWHM of 0.33 $Å^{-1}$ was obtained at the out-of-phase condition, which is about the same as that measured at the in-phase condition. Therefore, in the present experiment the string length is longer than can be determined with the instrumental resolution, >280 Å.

The spacing between the two split peaks at the out-of-phase condition was obtained as a function of surface temperature. This split peak spacing is used to obtain the average surface terrace width as shown in Fig. 33. The average vicinal terrace width remains ~ 120 - 140 Å from room temperature till 625 K, in agreement with results from x-ray diffraction by Keane *et al.* [5.7] and the scanning tunneling microscopy study of Sturmat *et al.* [5.10]. As Au(110) was heated over 625 K but below 740 K, an increased average vicinal terrace width was observed. The maximum average step terrace widths increase to ~ 173 Å, at 683 K, which is (34±10)% larger than measured at room temperature. This result is consistent with the picture that atoms originally forming the (1×2) reconstruction move and cause increased average step terrace widths. When the temperature was increased above 740 K, the surface average step terrace width was reduced to below that measured at room temperature and surface roughening increases with temperature. The estimated error bar in Fig. 33 corresponds to the stability of the incident electron beam, the noise of the CCD camera, and the minimum special resolution of the CCD camera.

The intensity profile of the specular peak perpendicular to the [001] direction is related to kinks and meanders at the step edge and variations in mean terrace size [5.28, 5.29]. From Fig. 33 we see that variations in the mean terrace size were small over the

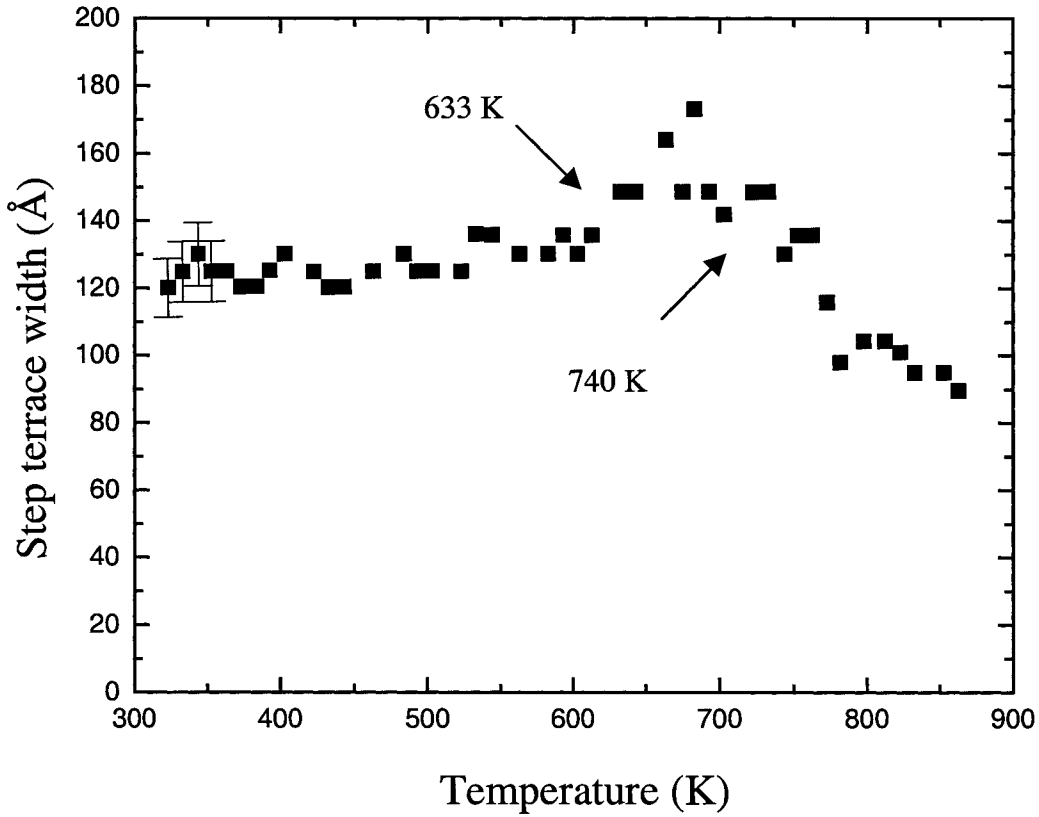

Figure. 33. The average surface step terrace widths are plotted as a function of temperature. An increase in the average step terrace width followed by a reduction with temperature is observed near T_c of the (2x1) to (1x1) phase transition.

studied temperature, thus, the intensity profile perpendicular to the [001] direction is expected to be predominantly affects by step edge roughness. The FWHM at the out-of-phase condition versus surface temperature is shown in Fig. 34. The average string length at the step edge is about ~ 140 Å at a surface temperature of 425 K. With further increase in surface temperature from 425 K to 700 K, the average string length remains almost unchanged in agreement with previous HRLEED results [5.3]. When the surface was heated over ~ 700 K, the average string length showed a dramatic reduction characteristic of a roughening transition consistent with the HRLEED observation of Romahn *et al.* [5.3]. The increased step edge roughness for temperatures higher than ~ 700 K corresponds to the decrease in terrace step size also shown in Fig. 34.

Electron thermal diffuse scattering at surfaces is enhanced by defects such as vacancies, adatoms, and steps [5.41]. This effect has been used in a LEED experiment to monitor thermal-induced vacancy generation in Pb(100) [5.42]. The temperature-dependent adatom/vacancy density on the vicinal Au(110) surface can be probed using the ratio $R = I_{back}/(I_{peak}-I_{back})$ obtained at the out-of-phase condition where I_{back} is the RHEED background intensity measured at a location away from the diffraction peaks and I_{peak} is the peak intensity of a diffraction order. Both I_{peak} and I_{back} are measured at the out-of-phase condition. Based on kinematic diffraction theory, for a two-dimensional surface with only adatoms and vacancies the background intensity increases with the adatom/vacancy density. The ratio R is related to adatom/vacancy density n by $R \propto [(2n-1)^{-2} - 1] (1+2M)$ at the out-of-phase condition, where $2M$ is the Debye-Waller factor. Therefore, the adatom/vacancy density is given by $n \propto (1/2)[R/(1+2M) + 1]^2 + 1/2$. The vacancy density change is $\Delta n = n/n_{initial} - 1$, where n is the surface adatom/vacancy

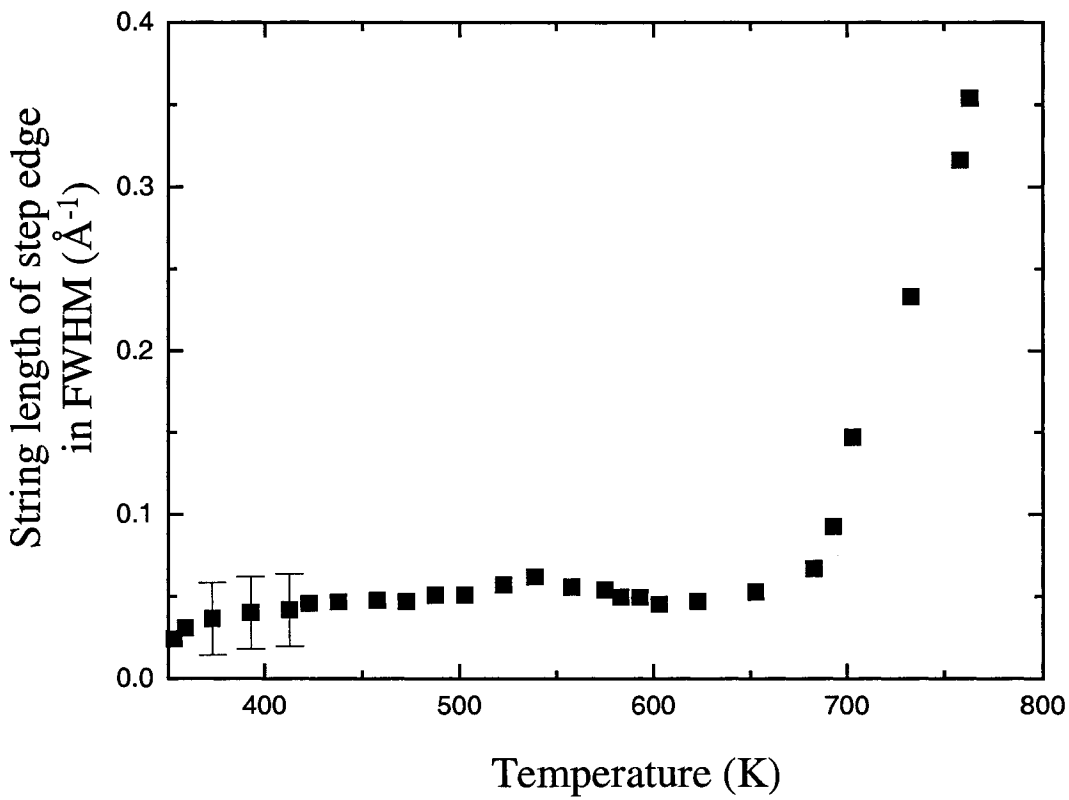

Figure. 34. The average string lengths at step edge are plotted as a function of surface temperature. Significant step edge roughness is observed for temperatures higher than ~ 700 K.

density at some temperature and $n_{initial}$ is the initial surface adatom/vacancy density before heating. Figure 35 shows the ratio R with temperature. The closed circles are taken during heating, open circles during cooling. In the inset, the calculated Δn is shown. The solid lines are exponential linefit to R and Δn below 650 K. We note that possible effects of terrace width and terrace edge roughness changes with temperature on the background intensity were neglected. These effects should be small below 650 K, but might contribute to the background at higher temperatures. However, the background enhancement due to adatoms and vacancies increases the uniform background, while that due to terraces gives broad diffuse intensity localized in the vicinity of the diffraction peak [5.41]. In our case, we measure the background midway between two diffraction orders to give a good representation of the uniform inelastic background intensity. The adatom/vacancy density on surface terraces increases slowly with temperature over the range of 300 K to ~ 650 K. Over that temperature range only 20% increase in adatom/vacancy density is measured. The increase in the equilibrium terrace adatom/vacancy density over the temperature range 300 K to 650 K is exponential. A vacancy formation energy E_f ~ 0.18 eV is extracted from the Arrhenius equation $n \propto exp(-E_f/kT)$, where k is Boltzman's constant. For temperatures higher than ~ 680 K, there is a noticeable enhanced temperature dependence on the adatom/vacancy density. Thus, changes in the average surface step terrace width, observed in Fig. 33, and the strong reduction in the step edge roughness for temperatures higher than ~ 700 K, observed in Fig. 34, are accompanied by increased defect density on terraces in Fig. 35. The collapse of steps during the (1x2) to (1x1) deconstruction phase transition produced significant disordered atoms on terraces in agreement with previous results [5.3, 5.43].

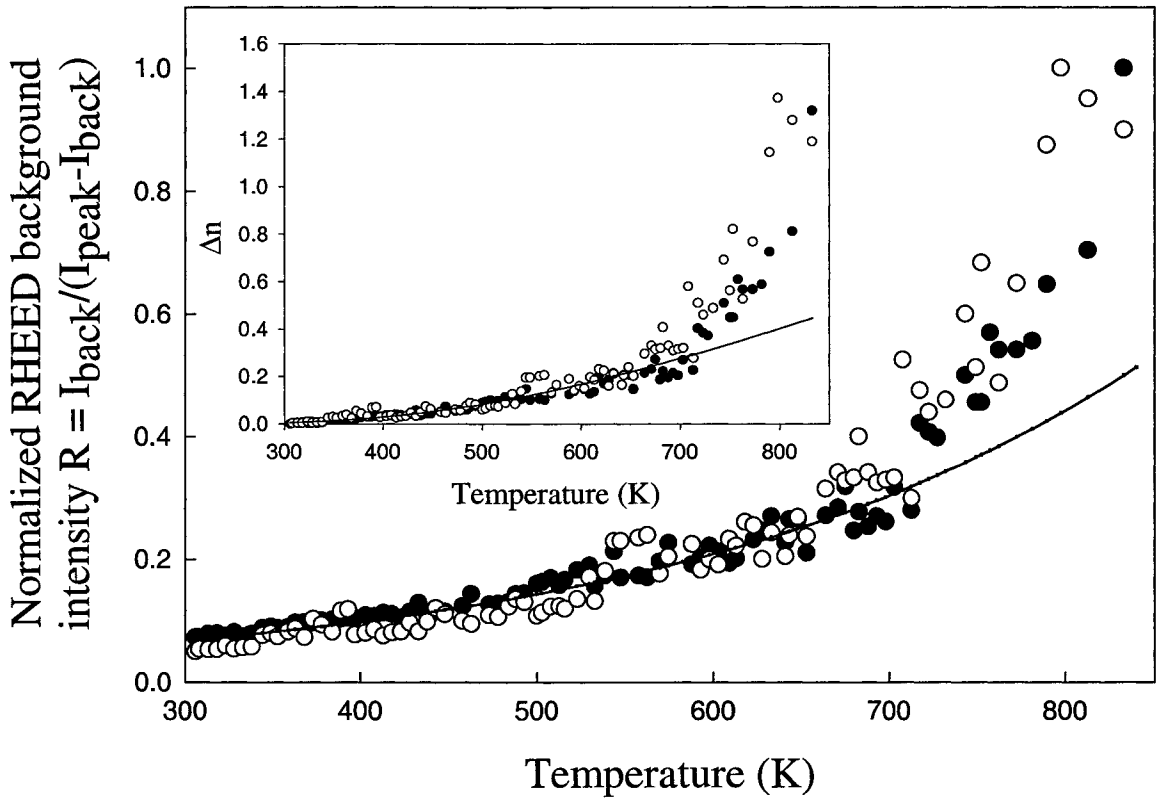

Figure. 35. The ratio $R = I_{back}/(I_{peak}-I_{back})$ is measured at out-of-phase condition as a function of surface temperature. When the surface temperature is raised, an increase in the RHEED background is observed. The increase in the ratio R measured at the out-of-phase condition indicates an increased surface adatms/vacancies. The solid lines are exponential linefit to data below 650 K. The inset shows change in the adatom/vacancy density upon heating from 300 K. The closed circles are taken during heating, open circles during cooling.

It is interesting to note that the considerable increase in the high temperature surface roughness in Au(110) was not accompanied by enhanced anharmonicity in the atomic vibration of the surface atoms forming the (1x1) structure. Any increase in surface anharmonicity would have been detected in the Debye-Waller curve of the (0,0) order in Fig. 30. This intensity versus temperature curve continues to follow the expected exponential dependence up to ~ 900 K, with some increase in data scatter above ~ 730 K. Thus, we can rule out that surface enhanced anharmonicity is a driving mechanism for the observed roughening transition as was observed in other fcc(110) metals, such as in Pb(110) [5.44].

In the RHEED measurement of surface roughness, we have interpreted all the data in the kinematic approximation. Multiple scattering effects generally do not significantly affect RHEED lineprofile except for some special cases of surfaces with complex crystal structures [5.28]. It has been shown that forward diffuse scattering in the surface layer combined with bulk diffraction can produce strong intensity enhancement in regions of the streaks outside the Laue circle [5.45]. These Kikuchi-like effects were not observed in the present study. Multiple scattering effects can also be present in the lattice relaxation results obtained from Fig. 29 and the adatom/vacancy concentration change in Fig. 35. Several approaches have been proposed to include multiple scattering effects on RHEED intensity calculations [5.46-5.48]. Performing these calculations on a relatively simple and well-studied surface such as the Au(110) could provide more information on the limitations of the kinematic approach.

5.4. Summary

The Au(110) surface structure and morphology throughout the (1x2) deconstruction phase transition is investigated using reflection high-energy electron diffraction. At room temperature, the topmost layer is observed to be contracted by 0.31 ± 0.03 Å or ~22% from a bulk terminated structure. A surface Debye temperature of 65±6 K is measured and no unharmonic effects are observed in the intensity-temperature curve of the (0,0) order up to the highest temperature studied, ~ 900 K. The critical temperature of the (2x1) deconstruction transition is 650 K in agreement with LEED results [5.3, 5.4], but lower than observed by SARIS [5.14] and STM [5.10] that observe the short-range order. Critical exponents of the (2x1)-(1x1) phase transition are consistent with the Ising universality class. The surface morphology was probed throughout the deconstruction phase transition. The average step terrace width of the vicinal Au(110) surface remains roughly constant from room temperature up to ~ 625 K and increases by (34±10)% at 683 K consistent with the picture that atoms originally forming the (1×2) reconstruction move and initially cause increased average step terrace widths. The average surface string length on Au(110) remains basically unchanged up to ~ 650 K and decreases sharply at higher temperatures indicative of a step induced roughening transition. Measurement of adatom/vacancy density on terraces shows a noticeable increase above ~ 680 K. Since the MR structure was previously observed with SARIS near 700 K [5.10], the present results supports that roughness accompany the deconstruction transition and that surface roughness develops as increased step edge roughness and terrace adatom/vacancy density.

Chapter VI

A LASER-DRIVEN PHOTOEMISSION ELECTRON MICROSCOPE

6.1. Introduction

The development of the photoemission electron microscope (PEEM) with time-resolved ability is a valuable research tool for surface science. PEEM is different from most conventional transmission electron microscopes in that the specimen is the source of electrons [6.1-6.5]. PEEM is a high-contrast method rediscovered recently because of its versatility, low surface damage, and surface selectivity [6.1]. Because PEEM has the ability to image as few as one monolayer thick of atoms on the surface, photoelectrons play an important role in the investigation of solids surfaces. PEEM image of a flat sample surface is the two-dimensional maps of the photoelectron yield. The traditional PEEM is a static microscopy; the time resolution is limited by the recording device reaching only milliseconds. Other microscopes like scanning tunneling microscope, scanning atomic force microscope, light interference microscope, reflection electron diffraction microscope [6.6], light reflection microscope [6.7], or photoacoustic signal generation microscope [6.8], can't visually observe local changes of the treated material in real time.

Recently, the real-time observation of the chemical and physical processes at surfaces has become most active research areas [6.9]. Several established electron microscopy techniques can be developed with high temporal resolution. Transmission

electron microscope (TEM) with tens of nanosecond temporal resolution has been used by Bostanjoglo *et. al.* to study phase transformations, including crystallization of amorphous films [6.10]. Reflection electron microscopy (REM) has been widely used to observe the surface morphology [6.11]. In REM, the contrast is due to shadow casting and scattering within the uppermost layer. Electron mirror microscopy was used by Telips and Bauer to observe the surface morphology [6.12]. All of these electron microscopy techniques require the delivery of a fine focussed electron beam to the sample, followed by imaging the objects by objective and projective lenses. In principle, it is possible to construct a time-resolved electron microscope based on any of the above-mentioned techniques. The problem lies mainly in the large number of electrons and large electron current. This makes it difficult to avoid space-charge broadening of the electron pulse, thus, achieving picosecond temporal resolution is complicated.

Surface melting behavior is an interesting topic of research. Several experiments have shown surface superheating. For example, surfaces superheating when heated by 100-180 ps laser pulses have been observed for Pb(111), Bi(0001), In(111) and Ge(111) [6.13-6.16]. A 120 K superheating above the bulk melting temperature of Pb was obtained from time-resolved RHEED experiments on Pb(111) [6.13]. Surface superheating was also demonstrated in molecular dynamic simulation [6.17]. An estimate on the upper limit of surface superheating was theoretically obtained [6.18]. Recently, a time-resolved two-photon photoemission electron microscope was built and used to map the dynamics of photo-excited electrons at a structured metal and semiconductor surface [6.19]. The two-photon photoemission electron microscope is an attractive tool to study surface melting.

In our experiment, a laser-driven photoemission electron microscope was developed and was used to perform an initial study of surface morphology during laser heating of Pb(111) single crystal. The basic idea of this microscope is the use of ~50 ps ultraviolet laser pulse to photoemit electrons from the surface, while a synchronized infrared laser pulse heats the surface and induces surface morphology changes. The photoemitted electrons are imaged using three electrostatic electron lenses on a pair of microchannel plates. Laser induced morphological changes can be observed. The temporal delay between the UV and IR laser pulses could be varied by the delay line in the IR laser pulse to set the time at which the surface morphology is imaged. This design of PEEM has the potential to be used as a time-resolved PEEM. The spatial resolution of this design is found to be 5 μm.

6.2. Microscope construction and basic design

Our design goal was a PEEM with 100 picoseconds temporal resolution and several μm spacial resolution. Since the primary use of this instrument is for surface study, a relatively larger gap between the sample and first electrode (> 5 mm) is needed. A large gap providing the space needed for efficient sample illumination and access for another operation in which the IR laser heating is introduced into the surface of the specimen, while the image is being observed.

There are several factors, such as lens aberrations, electron space charge and shot noise, that limit resolution of PEEM. The first limitation of temporal resolution in the electron pulse is space charge. Space charge can cause transit-time broadening. In order to minimize the effects of space charge broadening, a large extraction field is needed to

quickly accelerate the electrons once emitted from the photocathode. But high-voltage breakdown in vacuum limits the increase of extraction field. Typically, the maximum dc electric fields near the cathode are limited to 10 kV/mm [6.20]. The resolution limit due to space-charge aberrations was estimated by Massey [6.21]. The resolution limit in a laser-illuminated photoelectron microscopy is about 500 Å for 30-keV electrons in a beam of 1-A/cm^2 current density [6.21].

The second limitation of the resolution of photoemission electron microscope is the uncorrected accelerating field. The photoemission electron microscope has the following spacial limitation due to the aberrations of the uncorrected accelerating field [6.20].

$$\Delta x = 1.2\ \Delta E/eF \qquad (6.1)$$

where ΔE is the most probable initial energy, e is electron charge and F is the electric field strength immediately in front of the specimen surface, which is used as cathode. If $h\nu$ is the quadrupled-frequency of the Nd:YAG laser, and $h\nu_c$ is the work function of cathode, we have, according to Einstein's relation for the photo-effect.

$$\Delta E = h(\nu - \nu_c) \qquad (6.2)$$

Where ν_c is cutoff frequency.

For Pb(111), work function is 3.85 eV [6.1]. The quadrupled frequency of the Nd:YAG laser is 266 nm and the E-field at specimen is 5×10^6 V/m. Thus, the resolution limit due to lens aberration caused by electron energy spread is $\Delta x \sim 1$ μm.

In the short pulse photoemission electron microscope, negative space charge and Weingärtnerby shot noise is a factor that limits the spatial resolution. According to Bostanjoglo [6.20]

$$\Delta t \cdot \Delta x^2 \geq \frac{20e\alpha(S/N)^2 d^{1/2}}{\pi C K^2 F^{3/2}} \qquad (6.3)$$

where S/N is the signal to noise ratio that requires a minimum value (S/N>3) to separate two neighboring points; α is the account for detector noise ≥ 1; K equals to $(n_1-n_2)/(n_1+n_2)$ and is the contrast of two regions with n_1 and n_2, the number of electrons; d is cathode-Wehnelt distance = 5 mm. Inserting typical values for the used setup are: F = 5×10^6 V/m, d = 5 mm, C = 2.34×10^{-6} $A/V^{2/3}$, K = 0.2, S/N = 5, α = 1.5 , and imaging time Δt = 100 ps, a spatial resolution of $\Delta x \geq 5$ μm is calculated for the aberration-free pulsed PEEM.

For UHV compatibility, we only use stainless steel and alumina ceramic. The microscope was designed to be mounted on a standard 8 inches con-flat flange and constructed with three electron lenses consisting of a combination of cathode lens, an intermediate lens, and a projector lens, as shown in Fig. 36. In emission microscopy the objective lens is often called the cathode lens, electrons emitted from the sample are accelerated by the cathode lens, and a real image is formed on the micro-channel plates (MCP). The voltage on the sample surface (cathode) is -24.09 kV and the voltage on the Wehnelt electrode is -22.96 kV. We applied -20.8 kV voltage on both the intermediate lens and projection lens. The electrons are imaged on the internal MCP proximally coupled to a phosphor screen to amplify the electron signal and to convert the electron

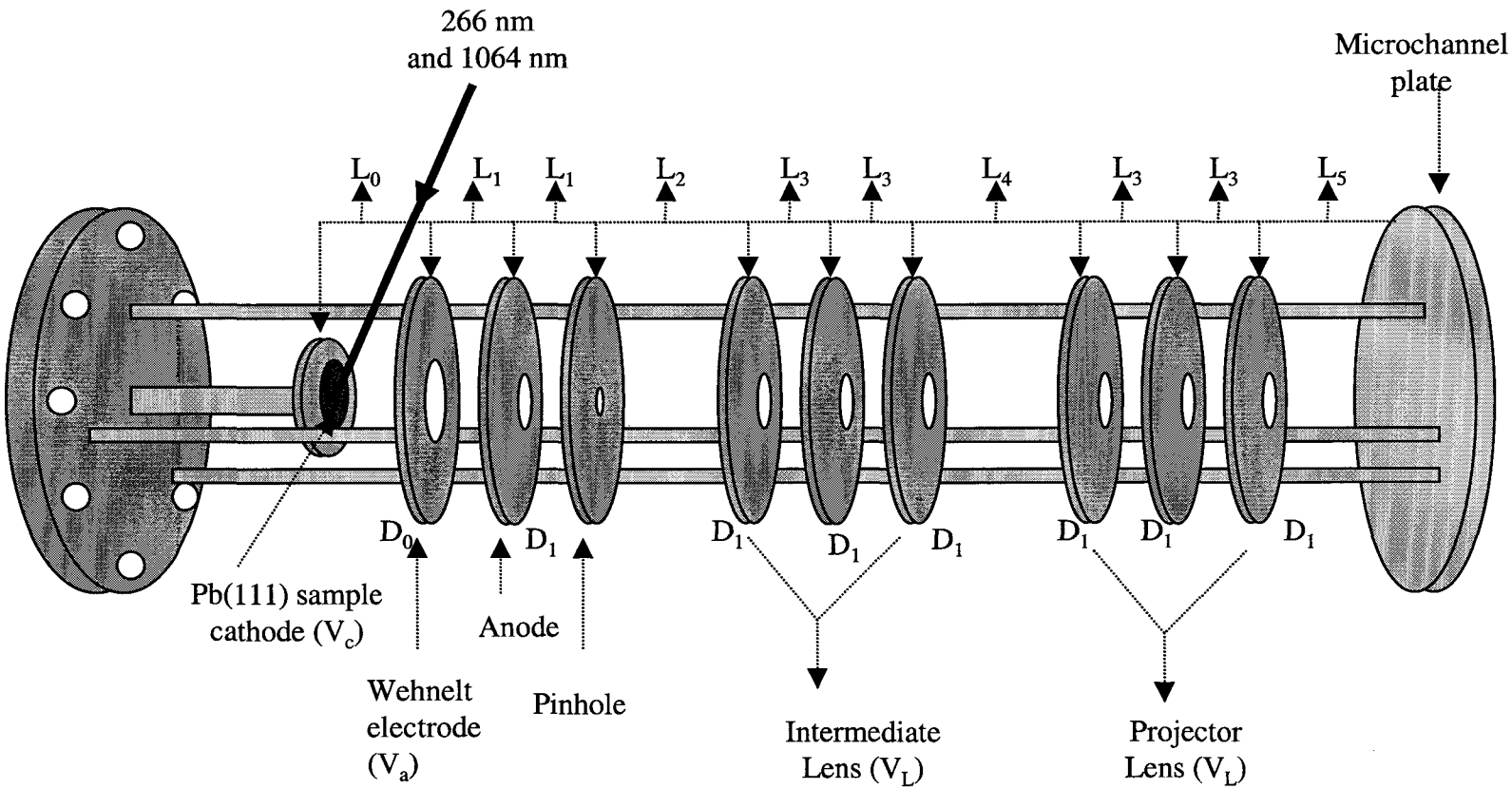

Figure 36. The cross section of designed PEEM. The following parameters are used in this PEEM. V_c = -24.09 kV, V_a = -22.96 kV, V_L = -20.8 kV, L_0 = 5 mm, L_1 =12.8 mm L_2 = 38.5 mm, L_3 = 9.5 mm, L_4 = 57.5 mm, L_5 = 410 mm, D_0 = 15 mm, D_1 = 10 mm.

image to optical image. The optical image from the phosphor screen is recorded by a charge coupled device (CCD) camera, and stored in a computer.

Unipotential Einzel lenses were used to design the PEEM lenses [6.22]. The following abbreviations and suffixes are used in the PEEM lens data: D_x is diameter of the electrode aperture, and L_x is inter-electrode spacing. The cathode lens has two electrodes, which lie in front of the cathode that is the Pb(111) crystal. The first electrode, D_0 = 15 mm in diameter aperture, is the Wehnelt electrode. The distance between cathode and Wehnelt electrode is 5 mm. The second electrode, D_1 = 10 mm and L_1 = 12.8 mm, is an anode which is grounded. The dimensions of an intermediate lens and a projector lens are the same, D_1 = 10 mm, L_3 = 9.5 mm and center electrode thickness = 10 mm. The distance between cathode lens and intermediate lens is L_2 = 38.5 mm and the distance between the intermediate lens and projector lens is L_4 = 57.5 mm. By verify the selected parameters, the Simion software was used. The Simion software simulates electrostatic potential by numerically solving Laplace's equation. An amplification of 240 is obtained from Simion simulation. Figure 37 shows the result of Simion simulation. The diameter of the imaged area is around 160 μm. Since the ratios of the voltages determine the electron-optical properties of the lens system, all the voltages of this design are provided by a single high-voltage power supply with voltage divider. The voltage divider provides the stable voltage ratios and reduces the requirement of absolute stability for the high voltage power supply.

6.3. Performance and application of the PEEM

The PEEM was tested in a vacuum chamber with a base pressure of 10^{-7} Torr. We noted that the surface possible contaminated by oxide at the vacuum level of 10^{-7} Torr in

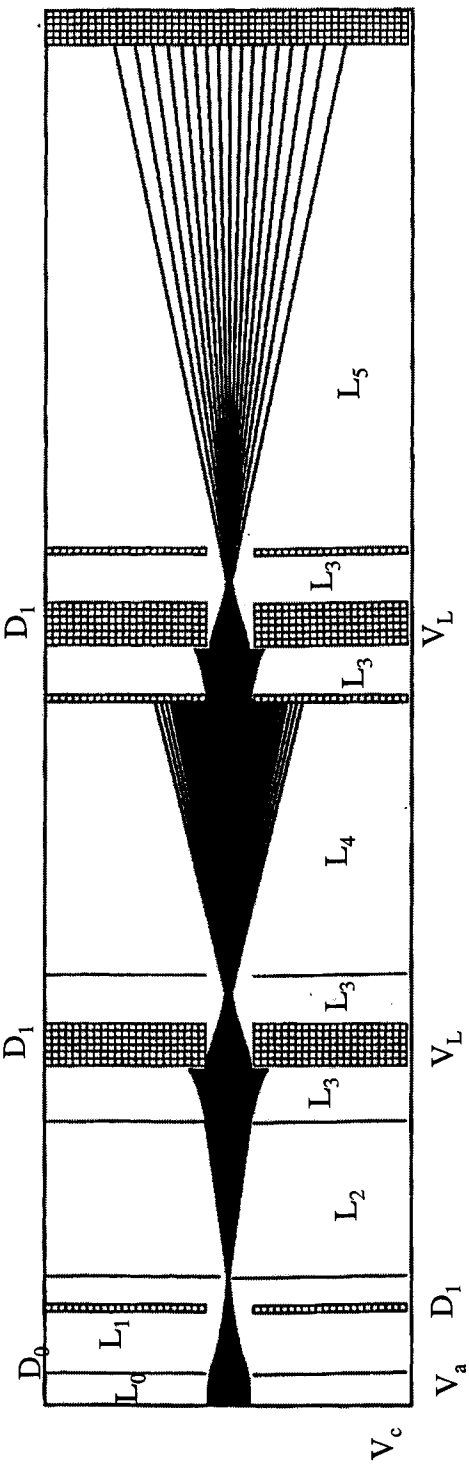

Figure 37. The computer simulation of PEEM is done by Simion software. Amplification of designed PEEM is 240.

this system. The contamination may reduce the electron emission intensity. A quartz window allows UV light passing into the vacuum system onto the cathode, which is a Pb(111) crystal. The UV light was incidence on the sample surface at the angle of 22°. A schematic diagram of the photoemission electron microscope setup with time-resolved ability is shown in Fig. 38. A 100-ps pulsed Nd:YAG oscillator and regenerative amplifier is used. The laser beam is TEM_{00} mode. The fundamental beam of the Nd:YAG laser, $\lambda = 1.06$ μm, is split into two beams. One beam interacts with the Pb(111) surface to provide a transient heating source. The other beam is frequency quadrupled to the ultraviolet ($\lambda = 0.266$ μm) and strikes on the sample surface to produce photoemitted electrons. The UV laser spot size is 1 mm in diameter. The photoemitted electrons are accelerated and imaged on the MCP by three electrostatic lenses. In order to calibrate the spatial resolution of PEEM, we put a silicon wafer with fabricated 50-μm square pattern on it. Figure 39 shows the image of silicon wafer pattern. From this image, the lateral resolution is determined to be 5 μm. The PEEM system also allows a 500 μm field of view as shown in Fig. 39(a). The diameter of the imaged area is between 160 μm and 500 μm. The undistorted image of different amplification can be obtained by the adjustment of the lens potentials.

The surface studied was Pb(111), which was the same sample used in our previous experiment [6.23]. The Pb(111) surface was mechanically polished and then etched in a solution of 80% glacial acetic acid and 20% hydrogen peroxide (30% in water). By only applying UV laser on the sample surface, a clear 3-dimension (3-D) image of the surface of the Pb(111) crystal was obtained, as shown in Fig. 40(a). Figure 40(b) also shows 2-dimension (2-D) image of Pb(111) surface.

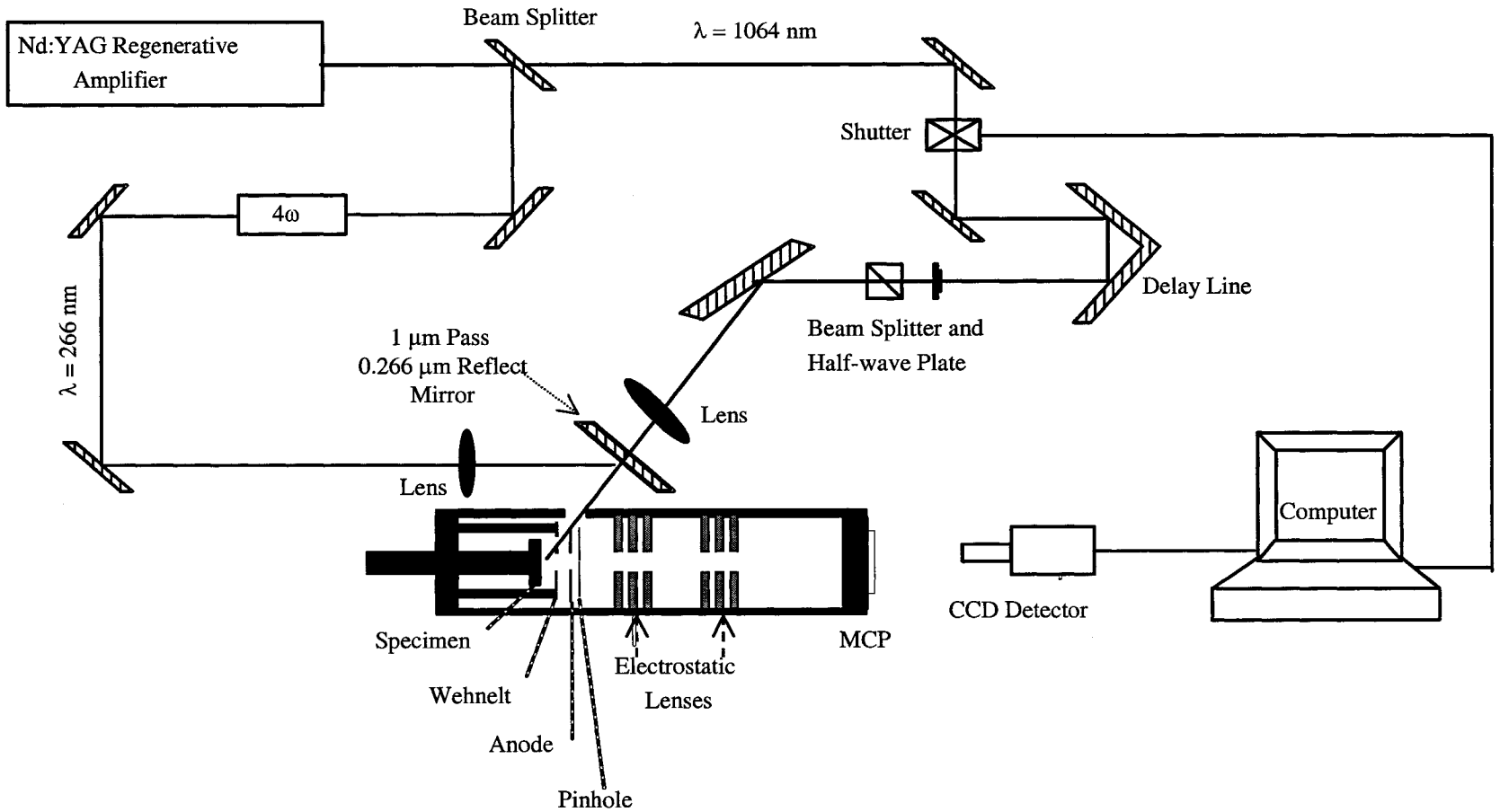

Figure 38. The schematic diagram for a laser-driven photo-emission electron microscope.

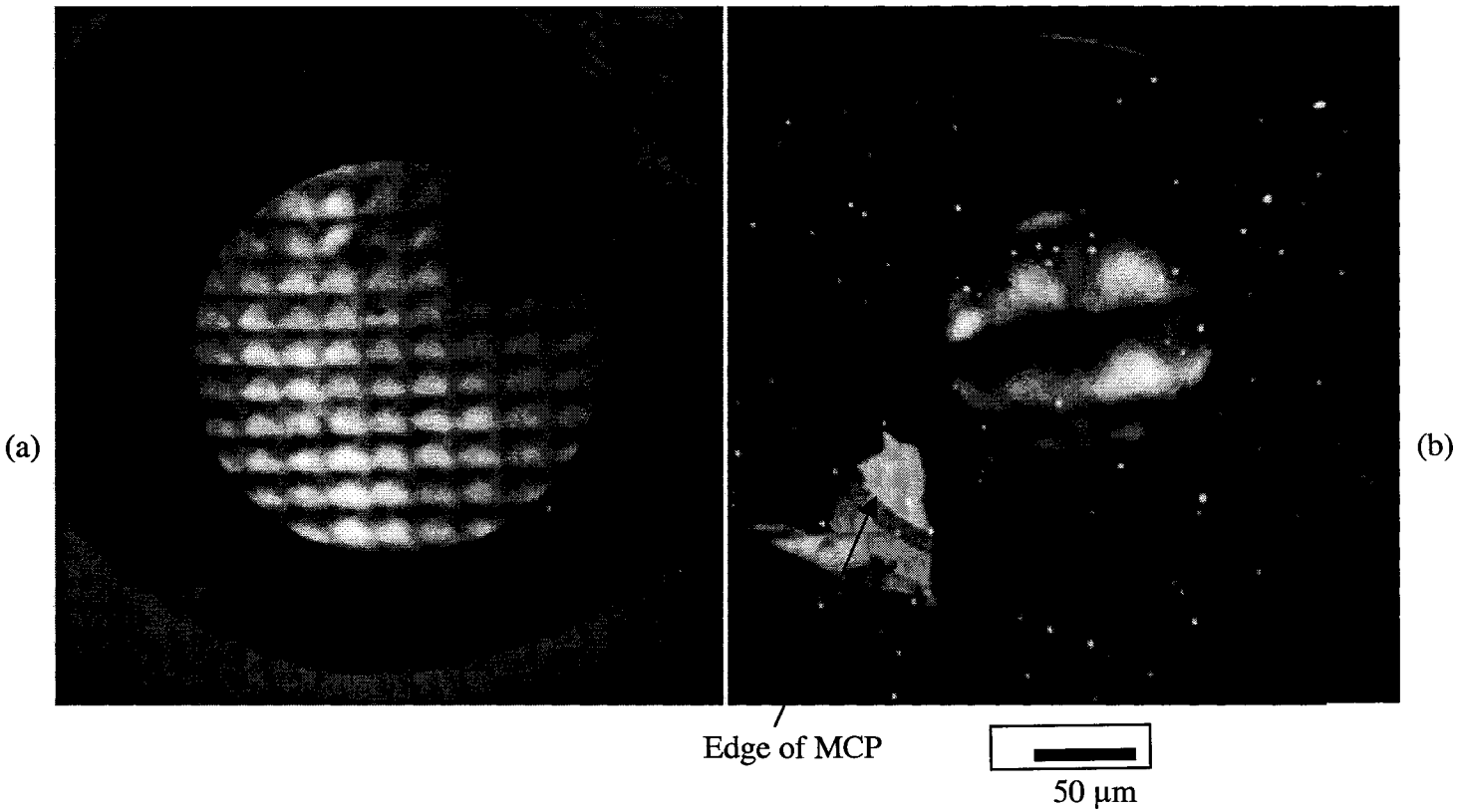

Figure 39. Calibration of photo-emission electron microscope. The image is a fabricated 50 μm mesh on silicon wafer. The excitation laser wavelength $\lambda = 266$ nm. (a) view of 450 μm across image. (b) view of 160 μm. The arrow indicates the edge of the microchannel plate. The view of 160 μm is restricted by a pin-hole that is used to reduce aberration. The scattering bright spots are due to noise in CCD camera.

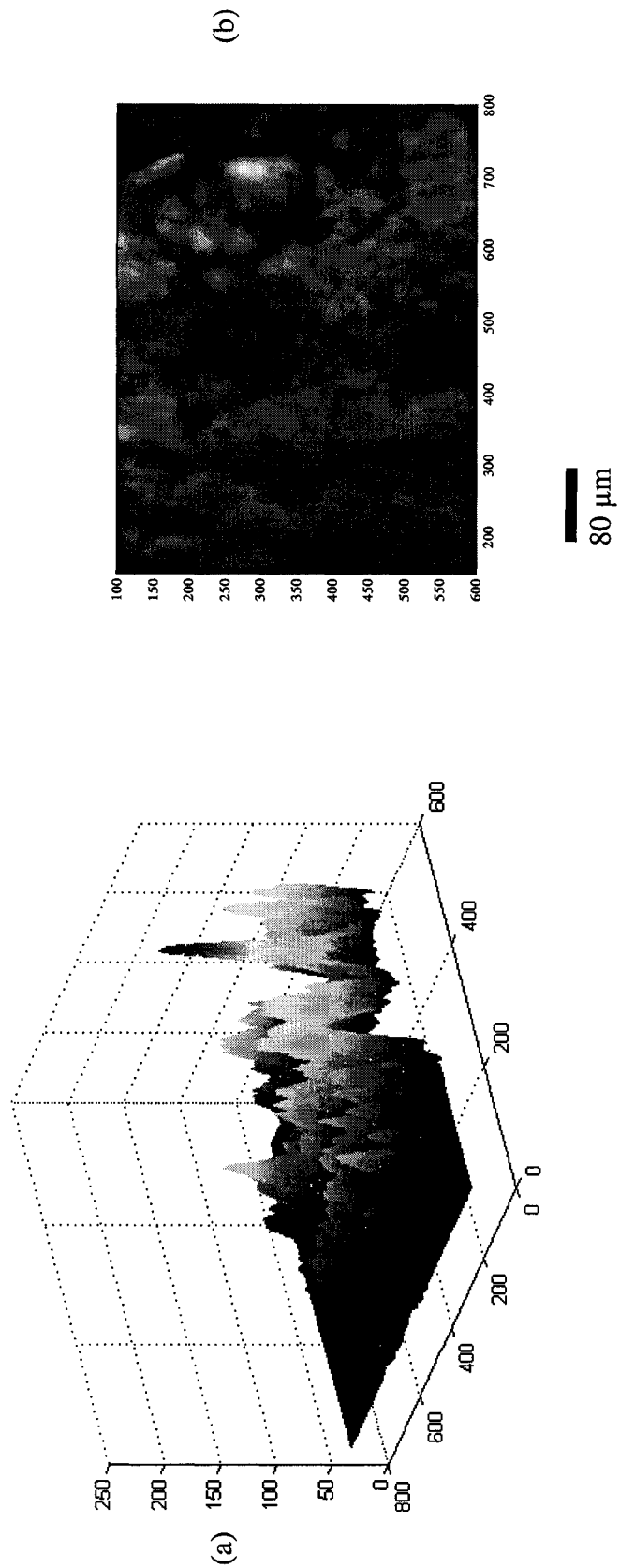

Figure 40. Image of Pb(111) surface. The image is the average of 54 laser pulses. The image was taken before laser heating.

We then applied the IR heating laser pulse to the surface to heat the Pb(111) sample. The spot size of IR laser was 200 μm in diameter. The laser peak fluence was varied from zero to 2.1×10^8 W/cm^2. If we only apply the IR laser pulse without the UV laser pulse on the sample surface, no image is showed on the MCP when the IR laser fluence is below a certain value. According to Richardson-Dushman equation, the thermal electron current density j_{RD} of Pb surface following:

$$j_{RD} = bT^2\exp[-W_{Pb}/(kT)] \qquad (6.4)$$

where k is the Boltzmann constant, W_{Pb} is the work function of the Pb(111) crystal, and $b\leq120$ A/cm^2 K^2. Inserting relevant values, the thermal electrons can be omitted for surface temperature below 2400 K. In our experiment the surface temperature range studied was under 1000 K, so the image was produced by non thermal electrons.

In order to estimate the surface temperature rise induced by laser heating, a one-dimension heat-diffusion model was used.

$$C\frac{dT(z,t)}{dt} = K\frac{d^2T(z,t)}{dz^2} + I_p(1-R)\alpha e^{-\alpha x}f(t) \qquad (6.5)$$

where T(z,t) is the temperature at a distance z normal to the sample surface (z = 0), t is the time, f(t) is the temporal profile of the laser pulse which is taken to be Gaussian in time as confirmed from the autocorrelator measurement; C = 1.58×10^6 J/m^3 K is the heat capacity per unit volume [6.24]; K = 32.2 W/mK is the thermal conductivity; R = 0.81 is the reflectivity; $\alpha = 7.05\times10^7$ m^{-1} is the absorption coefficient; and I_p is the peak laser intensity measured in W/cm^2. We used heat diffusion model to

estimate the temperature jump in previous experiments and found that the results are in agreement with the experimental measurements [6.13-6.16].

Figure 40 to Fig. 46 show the Pb(111) images of PEEM. In this experiment, a cube polarizing beamsplitter and a half-wave plate were used to adjust the laser fluence. The UV and IR laser pulse were fixed to reach the Pb(111) surface at same time by the fixed delay line.

Figure 40(a) shows a 3-D image of Pb(111) surface when only UV laser pulse was incident to the Pb(111) surface without IR laser pulse heating. We also noticed that the bright spot in the right corner is caused by intense UV laser pulse. In Fig. 41 an IR laser fluence of 0.76×10^{8} W/cm^2 was applied to heat the surface, which heats the surface to a temperature of 475 K calculated from heat diffusion model. The heated image in 41 is the same as the original image without IR laser heating. The IR laser fluence was further increased to 1.3×10^{8} W/cm^2 which heats the Pb(111) surface temperature to 598 K, as shown in Fig. 42. This surface temperature is near the Pb bulk melting point, 600.7 K. The PEEM image of the Pb surface is still the same as the image obtained without laser heating, as shown by comparing Fig. 42 with Fig. 40. The observed image was produced by the UV laser pulse only. We further increased laser fluence to 1.5×10^{8}W/cm^2 which heats Pb(111) surface temperature to 660 K, as shown in Fig. 43. This temperature is 60 K above the Pb bulk melting point. Only few spots become bright. When the IR laser fluence was increased to 1.7×10^{8}W/cm^2 which heats the surface to 700 K well above the Pb melting point. More bright spots are shown in Fig. 44. We believe that the bright spots are due to nonuniformity of the laser beam and defects on sample

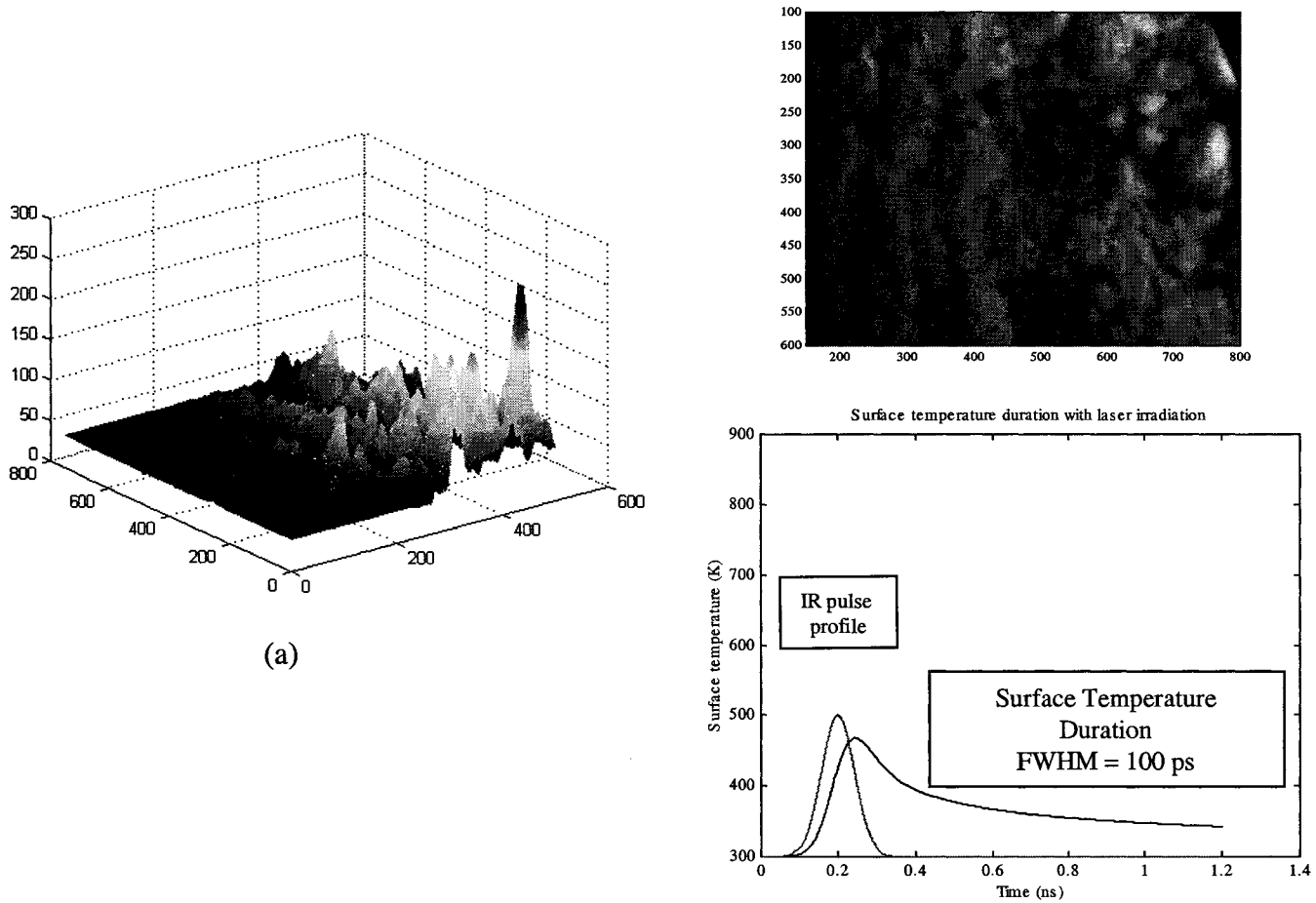

Figure 41. The image was taken with 0.76×10^8 W/cm^2, 90-ps laser pulsed heating. The solution of the heat diffusion equations shows that the surface temperature reaches 475 K.

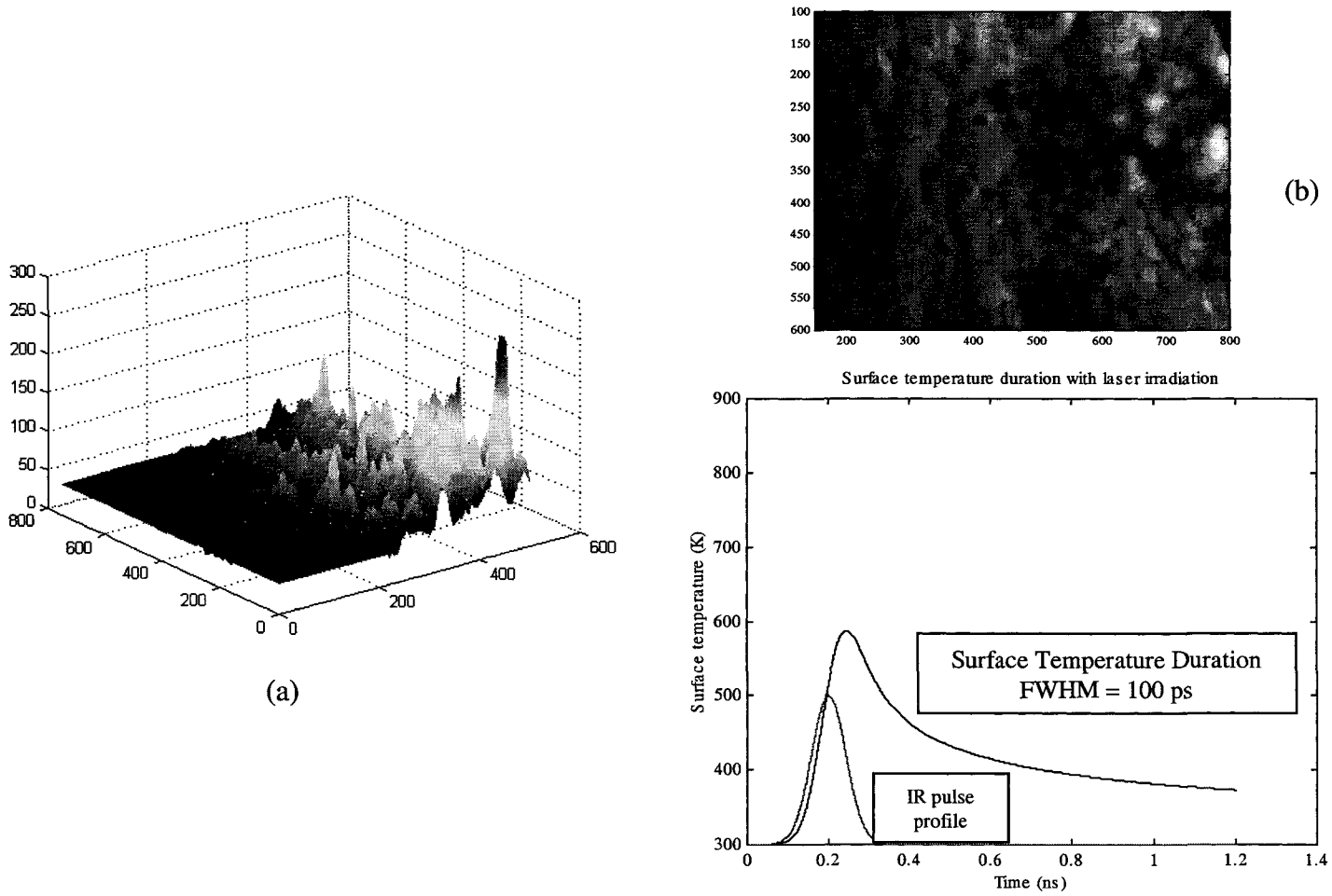

Figure 42. Image of Pb(111) surface with laser heating. The image is the average of 54 laser pulses. The image is taken with laser intensity of 1.3×10^{8} W/cm^2 corresponding to peak surface temperature of 598 K, several degrees below the Pb bulk melting temperature.

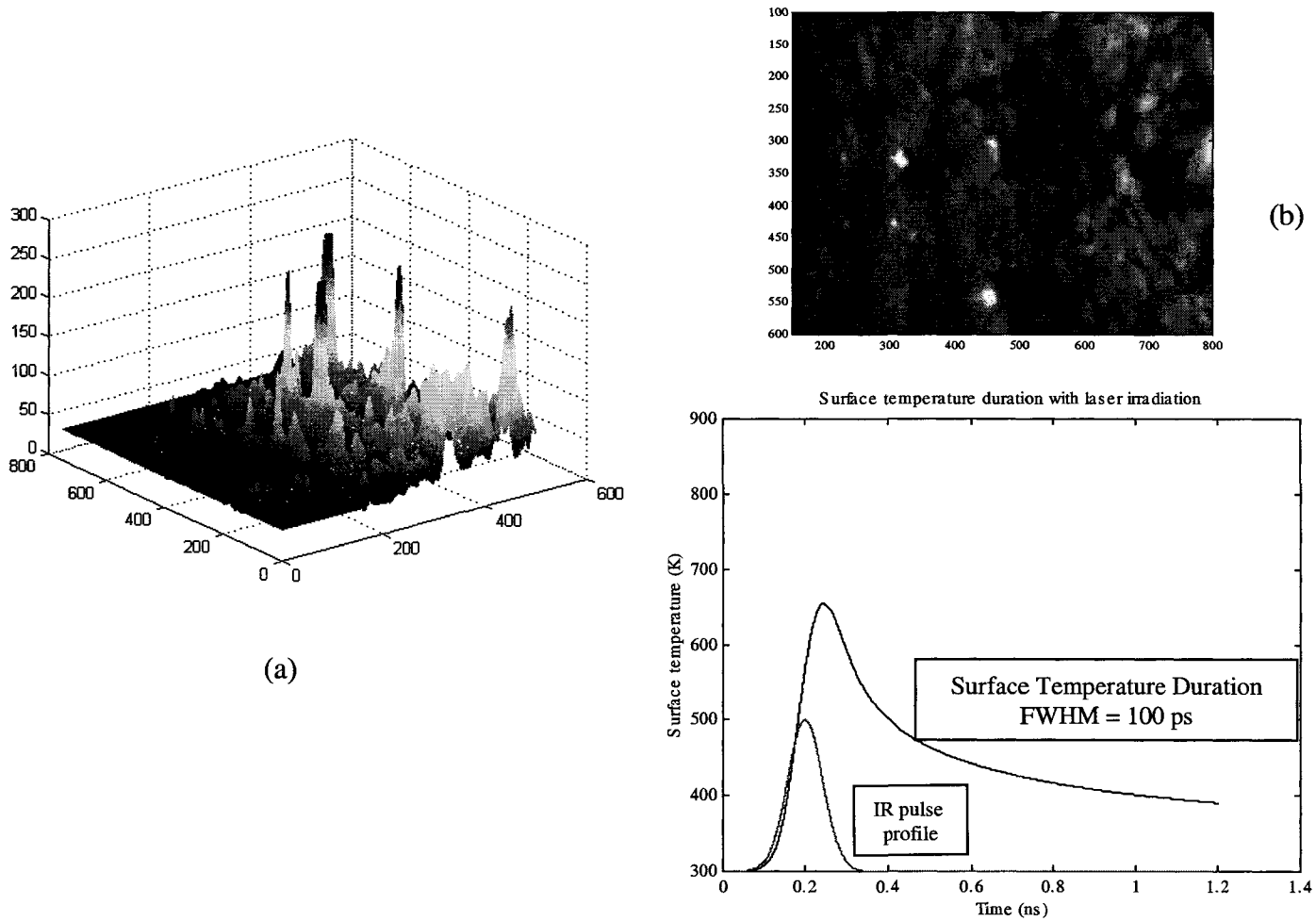

Figure 43. The image is taken with laser intensity of 1.5×10^8 W/cm^2 corresponding to surface temperature of 660 K, 60 degrees above Pb bulk melting temperature. There are four bright spots appear that may be melting spots due to surface defects or laser pulse non-uniform.

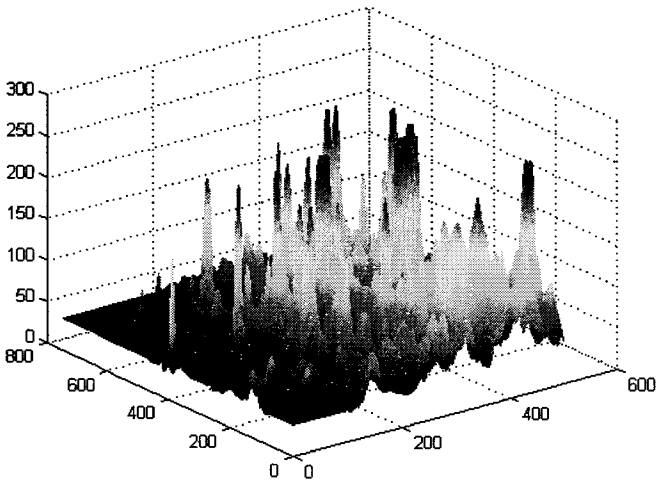

(a)

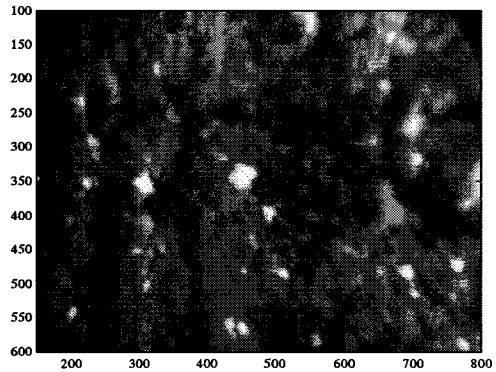

b)

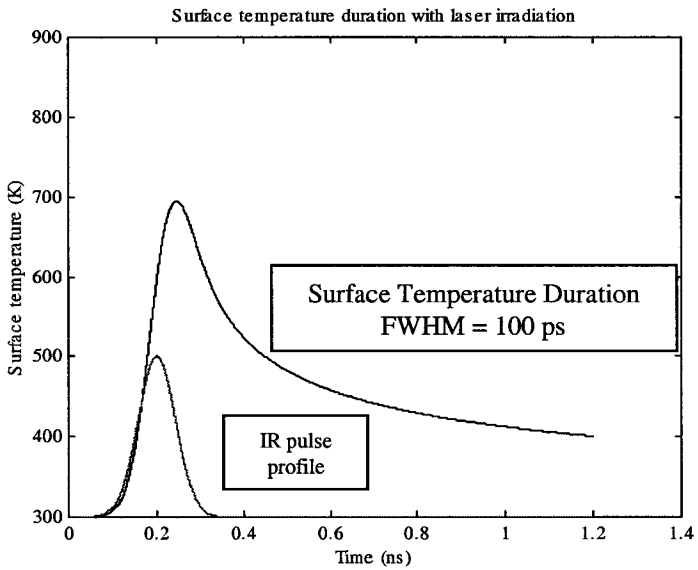

Figure 44. The image was taken with laser intensity of 1.7×10^8 W/cm^2 corresponding to surface peak temperature of 700 K, 100 degrees above Pb bulk melting temperature. There is more bright spots compared to Fig. 43.

surface. But most of the surface still remains the same as the non-laser-heating image. At this heating laser fluence, the surface temperature is already 100 K above the Pb bulk melting temperature. This is also the highest heating temperature that most of the image remains about the same as the non-laser-heating image. When the laser fluence was slightly increased further, a bright image was observed in a Fig. 45. Figure 45 was taken at a IR laser fluence of $1.8\times10^{8}W/cm^{2}$ which heats the surface to 715 K. The area of the Pb(111) surface that is heated by the 100-ps IR laser pulse begins to emit electrons intensively. The top flat surface reflected the saturation of CCD camera. The reason for the threshold of the bright image is still not full understood [6.25, 6.26]. Damascelli *et. al.* stated that multiphoton electron emission plays an important role for the threshold [6.25]. Henandez *et. al.* Considered the role of photoelectronic induced field emission [6.26]. The observed bright spots possibly relate to the intense laser field with the nonlinear photoemission and surface defects. In order to determine the total area of IR laser heating, the IR laser fluence was increased to $2.1\times10^{8}W/cm^{2}$, which is corresponding to surface temperature of 950 K according to the calculation of heat-diffusion model. The surface image of laser-heated area is become totally bright, as shown in Fig. 46. We also extracted the image intensity versus laser energy fluence, as shown in Fig. 47. Figure 47(a) shows the locations where the intensity data were extracted. The data in Fig. 47(b) are extracted from several different locations of the image that show the similar behavior. The threshold of laser fluence, $1.7\times10^{8}W/cm^{2}$ corresponding to surface peak temperature of 700 K in Fig. 44, can be obtained from Fig. 47(b) that possible relates to the nonlinear photoemission from surface defects. Figure 48 shows the percentage of melted surface as a function of incident laser energy fluence. It is

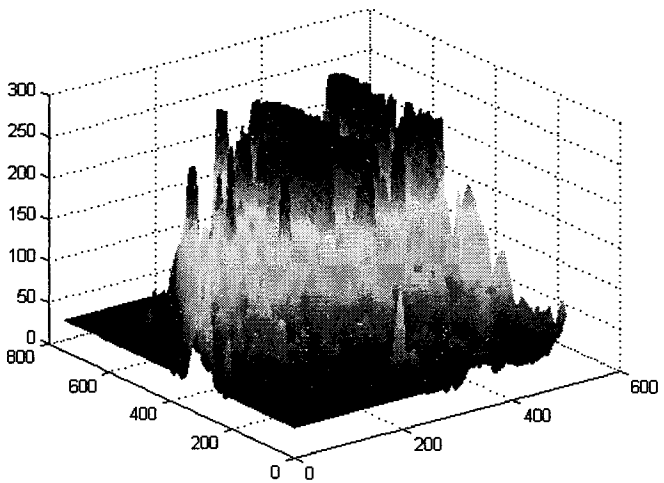

(a)

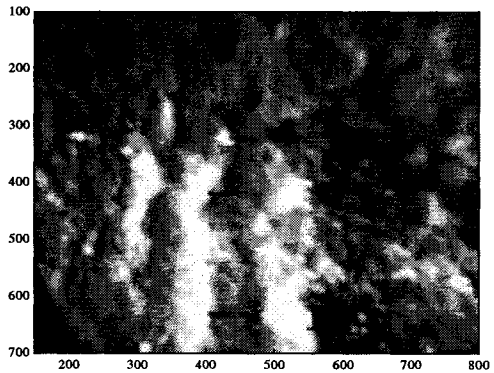

(b)

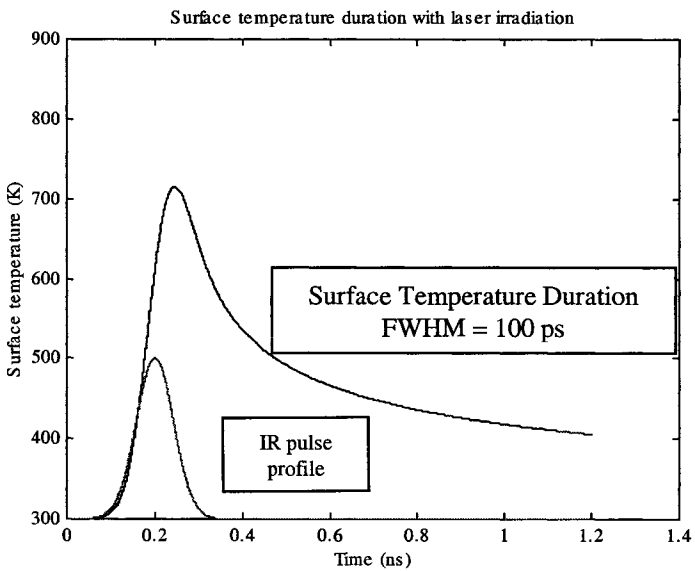

Figure 45. The image was taken with laser intensity of 1.8×10^8 W/cm^2. The surface temperature reaches 715 K. The area of laser-heated surface begins to emit electrons intensively.

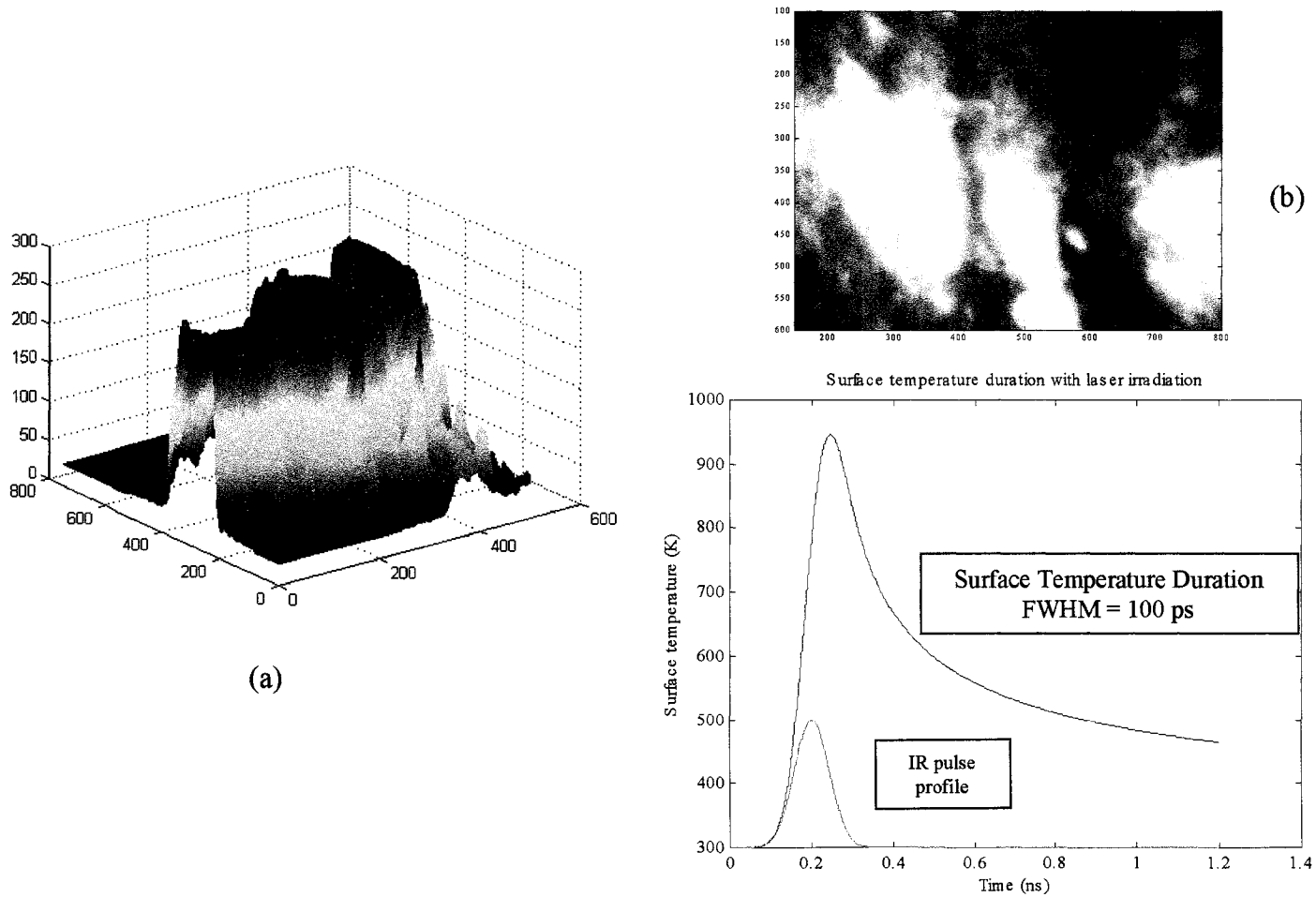

Figure 46. The image was taken with laser intensity of 2.1×10^8 W/cm^2. The surface peak temperature reaches 950 K, far beyond Pb bulk melting point (600.7 K). The area of laser-heated surface is totally melted. The bright parts of surface almost show an ellipse that is caused by the 22° incident angle of laser beam.

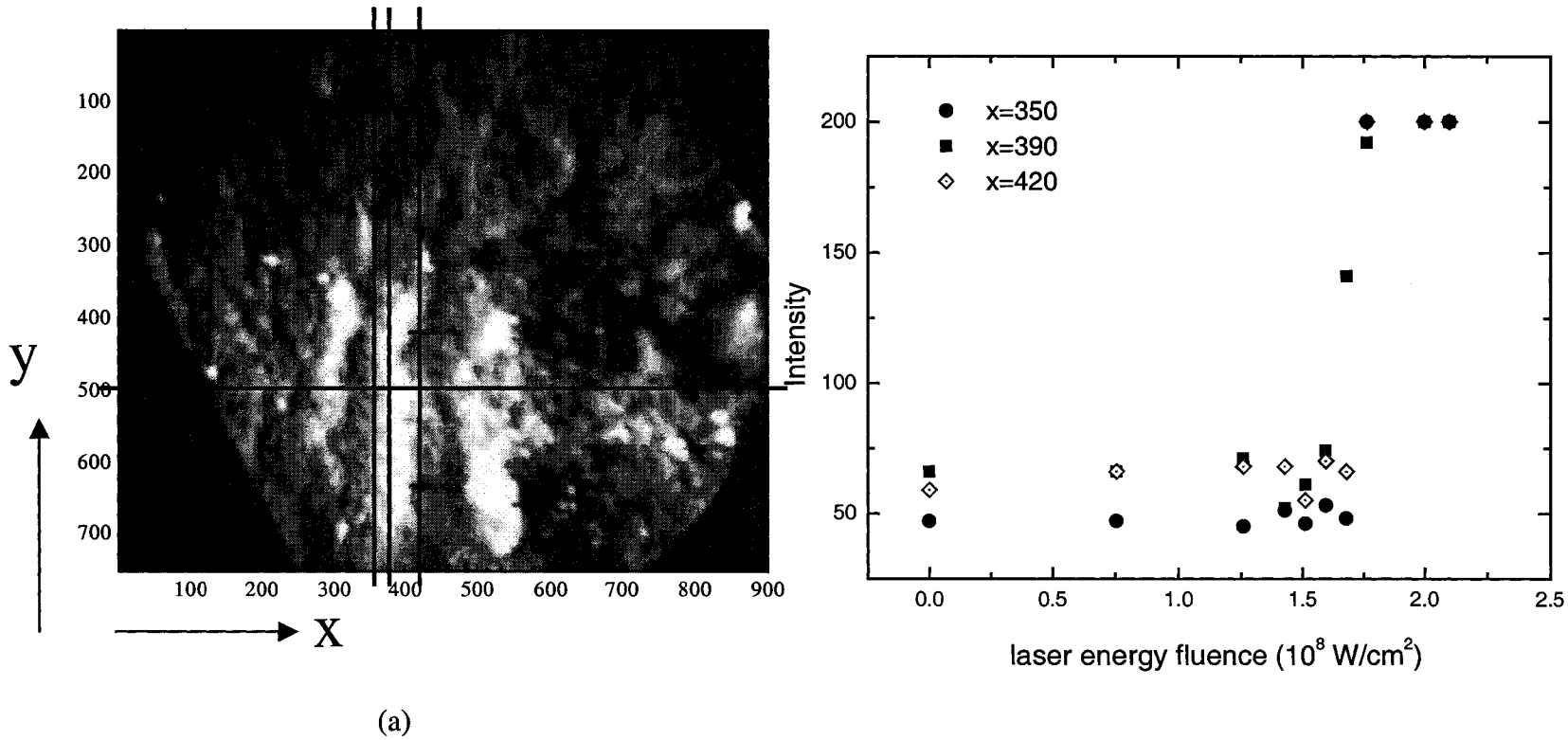

Figure 47. The intensities of images at the positions of cross in (a) are plot as a function of incident laser energy fluence in (b). The threshold of 1.7×10^8 can be extracted from this figure. When the intensity is more than 200, the camera is saturated.

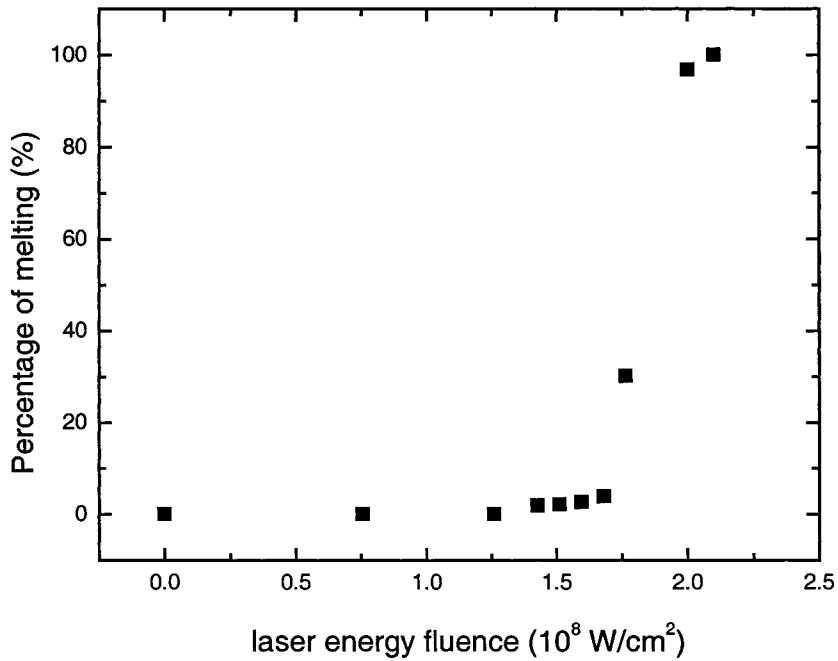

Figure 48. The percentage of melted area is plot as a function of incident laser energy fluence. The total area is defined as the size of the laser beam. The threshold of 1.7×10^8 can be extracted from this figure.

easy to conclude that Pb(111) surface does not melting when the heating laser fluence is under $1.7\times10^{8}W/cm^{2}$.

6.4. Conclusion

A laser-driven Photoemission electron microscope with 5 μm spatial resolution was developed and used to study surface morphology of laser heated Pb single crystal. The basic idea of this microscope is the use of ~50 ps ultraviolet laser pulse to produce photoemit electrons from the surface, while a well synchronized infrared laser pulse heats the surface and induces surface morphology changes. Surface morphological changes can be imaged. The photoemitted electrons are imaged using three electrostatic electron lenses on a pair of microchannel plates. The UV and IR laser pulses are set at the same time which the surface morphology is imaged during pulsed laser heating. When the surface is heated by picosecond laser pulse, the heating rate is in the order of 10^{12} K/s. Photoemission electron microscopy can be used to investigate the dynamics of laser heating-induced morphology changes on Pb(111). Using PEEM, visual images of Pb(111) surface below and above melting temperature recorded by CCD digital camera have been shown in this chapter.

Chapter VII

SUMMARY

This dissertation has contributed to the understanding of the dynamics of phase transition behavior on the low-index metal surface. Three metal surfaces, In(111), Au(110) and Pb(111), have been investigated. The high temperature behavior of the In(111) surface is investigated by means of time-resolved reflection high-energy electron diffraction. A 100-ps pulsed laser was used to provide a heating rate of ~ 10^{12} Ks^{-1}. The Au(110) surface has been studied for surface temperature from 300 K to 900 K. A laser-driven photoemission electron microscope with 5 μm lateral resolution was developed and used to study surface morphology during laser heating of Pb single crystal.

Indium (111) surface was selected because of its relatively low melting point and low vapor pressure near its melting point. The high temperature behavior of the In(111) surface was investigated using conventional and 100-ps time-resolved RHEED. For slow heating, In(111) remains solid up to the highest temperature studied, T_m – 4 K. Transient superheating of In(111) by 100-ps laser heating is observed up to $T_m + 73 \pm 9$ K. Raising the surface temperature above the maximum transient superheating temperature results in RHEED intensity reduction from that expected from Debye-Waller behavior. With temperature rise, an increase in vacancy density on In(111) surface is observed with no noticeable change in the FWHM of the RHEED profile at the out-of-phase condition, which indicates that the random step terrace width does not change with temperature. Transient superheating of the In(111) surface with laser fluence below the melting threshold does not change the surface morphology.

The Au(110) surface structure and morphology throughout the (1x2) deconstruction phase transition is investigated using reflection high-energy electron diffraction. At room temperature, the topmost layer is observed to be contracted by 0.31 ± 0.03 Å or ~22% from a bulk terminated structure. A surface Debye temperature of 65±6 K is measured and no anharmonic effects are observed in the intensity-temperature curve of the (0,0) order up to the highest temperature studied, ~ 900 K. The critical temperature of the (2x1) deconstruction transition is 650 K in agreement with LEED results [5.3, 5.4], but lower than observed by SARIS [5.14] and STM [5.10] that observe the short-range order. Critical exponents of the (2x1)-(1x1) phase transition are consistent with the Ising universality class. The surface morphology was probed throughout the deconstruction phase transition. The average step terrace width of the vicinal Au(110) surface remains roughly constant from room temperature up to ~ 625 K and increases by (34±10)% at 683 K consistent with the picture that atoms originally forming the (1×2) reconstruction move and initially cause increased average step terrace widths. The average surface string length on Au(110) remains basically unchanged up to ~ 650 K and decreases sharply at higher temperatures indicative of a step induced roughening transition. Measurement of adatom/vacancy density on terraces shows a noticeable increase above ~ 680 K. Since the MR structure was previously observed with SARIS near 700 K [5.10], the present results supports that roughness accompany the deconstruction transition and that surface roughness develops as increased step edge roughness and terrace adatom/vacancy density.

A laser-driven Photoemission electron microscope with 5 μm spatial resolution was developed and used to study surface morphology of laser heated Pb single crystal.

The basic idea of this microscope is the use of ~50 ps ultraviolet laser pulse to produce photoemit electrons from the surface, while a well synchronized infrared laser pulse heats the surface and induces surface morphology changes. Surface morphological changes can be imaged. The photoemitted electrons are imaged using three electrostatic electron lenses on a pair of microchannel plates. The UV and IR laser pulses are set at the same time which the surface morphology is imaged during pulsed laser heating. When the surface is heated by picosecond laser pulse, the heating rate is in the order of 10^{12} K/s. Photoemission electron microscopy can be used to investigate the dynamics of laser heating-induced morphology changes on Pb(111). Using PEEM, visual images of Pb(111) surface below and above melting temperature recorded by CCD digital camera have been shown in the chapter 6.

CHAPTER I REFERENCES:

[1.1]. J. F. van der Veen, "Surface-induced melting of solids," *Phase transitions in Surface Films 2*, Edited by H. Taub, (Plenum Press, New York), (1991).

[1.2]. J. Frenkel, *Kinetic Theory of Liquids*, (Oxford: Clarendon Press), pp. 425-426 (1946).

[1.3]. J. K. Kristensen, and R. M. J. Cotterill, "On the existence of pre-melting and after-melting effects. A neutron scattering investigation," *Phil. Mag.* **36**, pp. 437-452 (1977).

[1.4]. R. Lipowsky, "Critical surface phenomena at first-order bulk transitions," *Phys. Rev. Lett.* **49**, pp. 1575-1578 (1982).

[1.5]. J. Q. Broughton, and G. H. Gilmer, "Molecular dynamics investigation of the crystal-fluid interface. I. Bulk properties," *J. Chem. Phys.* **79**, pp. 5095-5104 (1983).

"Molecular dynamics investigation of the crystal-fluid interface. II. Structures of the FCC (111), (100), and (110) crystal-vapor systems," *J. Chem. Phys.* **79**, pp. 5105-5118 (1983).

[1.6]. S. Titmuss, A. Wander, and D. A. King, "Reconstruction of clean and adsorbate-covered metal surfaces," *Chem. Rev.* **96**, pp. 1291-1306 (1996).

[1.7]. W. Moritz and D. Wolf, "Multilayer distortion in the reconstructed (110) surface of Au," *Surf. Sci.* **163**, pp. L655-L665 (1985).

[1.8]. E. Vlieg, I. K. Robinson, K. Kern, "Relaxations in the missing-row structure of the (1×2) reconstructured surface of Au(110) and Pt(110)," *Surf. Sci.* **233**, pp. 248-254 (1990).

[1.9]. R. Koch, M. Borbonus, O. Haase, and K. H. Rieder, "Reconstruction behaviour of FCC(110) transition metal surfaces and their vicinals," *Appl. Phys.* **A 55**, pp. 417-429 (1992).

[1.10]. J. C. Campuzano, A. M. Lahee, G. Jennings, "On the feasibility of the missing row model of the (1×2) reconstructions of (110) Pt and Au," *Surf. Sci.* **152/153**, pp. 68-76 (1985).

[1.11]. J. F. van der Veen, B. Pluis, A. W. Denier van der Gon, *in Chemistry and Physics of Solid Surface VII*, edited by R. Vanselow and R. F. Howe (Springer-Verlag, Berlin), pp. 455 (1988).

[1.12]. A. Pavlovska, K. Faulian and E. Bauer, "Surface roughening and surface melting in the high temperature equilibrium shape of small Pb crystals," *Surf. Sci.* **221**, pp. 233-243 (1989);

B. Pluis, A. W. Denier van der Gon, J. W. M. Frenken and J. F. van der Veen, "Crystal-face dependence of surface melting," *Phys. Rev. Lett.* **29**, pp. 2678-2681 (1987).

CHAPTER II REFERENCES:

[2.1]. H. J. Fecht and W. L. Johson," Entropy and enthalpy catastrophe as a stability limit for crystalline material," *Nature* **334**, pp. 50-51 (1988).

[2.2]. S. Lele, P. Ramachandra Rao and K. S. Dubey, "Entropy catastrophe and superheating of crystals," *Nature* **336**, pp. 567-568 (1988).

[2.3]. K. Lu and Y. Li, "Homogeneous nucleation catastrophe as a kinetic stability limit for superheated crystal," *Phys. Rev. Lett.* **80**, pp. 4474-4477 (1998).

[2.4]. M. Iwamatsu, "Homogeneous nucleation for superheated crystal," *J. Phys.: Condens. Matter*, **11**, pp. L1-L5 (1999).

[2.5]. W. H. Shih, Z. Q. Wang, X. X. Zeng and D. Stroud, "Ginzburg-Landau theory for the solid-liquid interface of bcc elements," *Phys. Rev.* **A 35**, pp. 2611-2618 (1987).

[2.6]. Francesco D. Di Tolla, Furio Ercolessi, and Erio Tosatti, "Maximum overheating and partial wetting of nonmelting solid surfaces," *Phys. Rev. Lett.* **74**, pp. 3201–3204 (1995).

[2.7]. M. P. Allen and D. J. Tildesley, *Computer Simulation of Liquids*, (Oxford University Press), (1987).

[2.8]. M. F. Finnis and J. E. Sinclair, "A simple empirical N-body potential for transition metals," *Phil. Mag.* **A 50**, pp. 45-55 (1984).

[2.9]. M. S. Daw and M. I. Bakes, "Embedded-atom method: Derivation and application to impurities, surfaces, and other defects in metals," *Phys. Rev.* **B 29**, pp. 6443-6453 (1984).

[2.10]. K. W. Jacobsen, J. K. Norskov and M. J. Puska, "Interatomic interactions in the effective-medium theory," *Phys. Rev.* **B 35**, pp. 7423-7442 (1987).

[2.11]. F. Ercolessi, E. Tosatti, "Au (100) surface reconstruction," *Phys. Rev. Letts.* **57**, pp. 719-722 (1986).

[2.12]. F. Ercolessi, E. Tosatti, and M. Parrinello, "Simulation of gold in the glue model," *Phil. Mag.* **A 58**, pp. 213-226 (1988).

[2.13]. H. Hakkinen and Uzi Landman, "Superheating, melting, and annealing of copper surfaces," *Phys. Rev. Letts.* **71**, pp. 1023-1026 (1993).

[2.14]. J. F. van der Veen, "Surface-induced melting of solids," *Phase Transitions in Surface Films 2*, Edited by H. Taub, (Plenum Press, New York), (1991).

[2.15]. J. Frenkel, *Kinetic Theory of Liquids*, (Oxford: Clarendon Press), (1946).

[2.16]. J. K. Kristensen, and R. M. J. Cotterill, "On the existence of pre-melting and after-melting effects. A neutron scattering investigation," *Phil. Mag.* **36**, pp. 437-452 (1977).

[2.17]. R. Lipowsky, "Critical surface phenomena at first-order bulk transitions," *Phys. Rev. Lett.* **49**, pp. 1575-1578 (1982).

[2.18]. J. Q. Broughton, and G. H. Gilmer, "Molecular dynamics investigation of the crystal-fluid interface. II. Structures of the FCC (111), (100), and (110) crystal-vapor systems," *J. Chem. Phys.* **79**, pp. 5105-5118 (1983).

[2.19]. D. P. Woodruff, *The Solid-Liquid Interface* (Cambridge University Press, Cambridge), (1973).

[2.20]. J. F. van der Veen, B. Pluis, A. W. Denier van der Gon, *in Chemistry and Physics of Solid Surfaces VII*, edited by R. Vanselow and R. F. Howe (Springer-Verlag, Berlin), pp. 45 (1988).

[2.21]. J. W. M. Frenken and J. F. van der Veen, "Observation of surface melting," *Phys. Rev. Lett.* **54**, pp. 134-137 (1985); J. W. M. Frenken, P.M. J. Maree, and J. F. van der Veen, "Observation of surface-initiated melting," *Phys. Rev.* **B 34**, pp. 7506-7516 (1986).

[2.22]. J. W. Herman and H. E. Elsayed-Ali, "Superheating of Pb(111)," *Phys. Rev. Lett.* **69**, pp. 1228-1231 (1992).

[2.23]. E. A. Murphy, H. E. Elsayed-Ali and J. W. Herman, "Superheating of Bi(0001)," *Phys. Rev.* **B 48**, pp. 4921-4924 (1993).

[2.24]. P. Fery, W. Moritz and Wolf, "Structure determination of the (1x2) and (1x3) reconstructions of Pt(110) by low-energy electron diffraction," *Phys. Rev.* **B 38**, pp. 7275-7286 (1988).

CHAPTER III REFERENCES:

[3.1]. N. Georgiev, A. Pavlovska and E. Bauer, "Surface disordering without surface roughening" *Phys. Rev.* **B 52**, pp. 2878-2888 (1995).

[3.2]. M. G. Lagally, "diffraction Techniques" *in Methods of Experimental Physics*, Vol. **22**, (Academic Press, Inc.), pp. 237-298 (1985).

[3.3]. Bo Lin and H. E. Elsayed-Ali, "Temperature dependent reflection electron diffraction study of In(111) and observation of laser-induced transient surface superheating," *Surf. Sci.* **498**, pp. 275-284 (2002).

[3.4]. E. Bauer, *Techniques of Metals Research*, Vol. II, Part 2, edited by R. F. Bunshah (Interscience, New York), (1969).

[3.5]. E. John, K. M. Mahan, G. Y. R. Geib and G. L. Robert, "A review of the geometrical fundamentals of reflection high-energy electron diffraction with application to silicon surfaces," *J. Vac. Sci. Technol.* **A 8(5)**, pp. 3692-3700 (1990).

[3.6]. N. W. Ashcroft and N. D. Mermin, *in Solid State Physics* (Holt, Inehart, and Winton, Philadelphia), pp. 98 (1976).

[3.7]. M. G. Lagally, D. E. Savage, and M. C. Tringides, *in Reflection High-Energy Electron Diffraction and Reflection Electron Imaging of Surfaces*, edited by P. K. Laesen and P. J. Dobson, (Plenum Press, New York), pp. 139 (1988).

[3.8]. M. P. Seah and W. A. Dench, "Quantitative electron spectroscopy of surfaces: a standard database for electron inelastic mean free paths in solids," *Surface and Interface Analysis* **1**, pp. 2-11 (1979).

CHAPTER IV REFERENCES:

[4.1]. R. W. Cahn, "Melting and the surface," *Nature* **323**, pp. 668-669 (1986).

[4.2]. D. P. Woodruff, *The Solid-Liquid Interface*, (Cambridge University Press, London), (1973).

[4.3]. H. Teichler "Melting transition in molecular-dynamics simulations of the $Ni_{0.5}Zr_{0.5}$ intermetallic compound," *Phys. Rev.* **B 59**, pp. 8473-8480 (1999).

[4.4]. D. R. Uhlmann, "On the internal nucleation of melting," *J. Non-Cryst. Solids* **41**, pp. 347-357 (1980).

[4.5]. J. W. M. Frenken and J. F. Vender Veen "Observation of surface melting," *Phys. Rev. Lett.* **54**, pp. 134-137 (1985).

[4.6]. J. W. M. Frenken, P. M. J. Marée and J. F. van der Veen, "Observation of surface-initiated melting," *Phys. Rev.* **B 34**, pp. 7506-7516 (1986).

[4.7]. A. W. van der Gon, R. J. Smith, J. M. Gay, D. J. O'Connor and J. F. van der Veen, "Melting of Al surface," *Surf. Sci.* **227**, pp. 143-149 (1990).

[4.8]. B. Pluis, T. N. Taylor, D. Frenkel, and J. F. van der Veen, "Role of long-range interactions in the melting of a metallic surface," *Phys. Rew.* **B 40**, pp. 1353-1356 (1989).

[4.9]. H. M. van Pinxteren and J. W. M. Frenken, "Observation of surface-melting-induced faceting", *Europhys. Lett.* **21**, pp. 43-48 (1993).

[4.10]. J. Daeges, H. Gleiter and J. H. Perepezko, "Surperheating of metal crystal," *Phys. Lett.* **A 119**, pp. 79-82 (1986).

[4.11]. J. W. Herman and H. E. Elsayed-Ali, "Time-resolved study of surface disordering of Pb(110)," *Phys. Rev. Lett.* **68**, pp. 2952-2955 (1992).

[4.12]. J. W. Herman and H. E. Elsayed-Ali, "Superheating of Pb(111)," *Phys. Rev. Lett.* **69**, pp. 1228-1231 (1992).

[4.13]. J. W. Herman, H. E. Elsayed-Ali and E. A. Murphy "Time-resolved structural study of Pb(100)," *Phys. Rev. Lett.* **71**, pp. 400-403 (1993).

[4.14]. J. W. Herman and H. E. Elsayed-Ali, "Time-resolved structural studies of the low-index faces of lead," *Phys. Rev.* **B 49**, pp. 4886-4897 (1994).

[4.15]. E. A. Murphy, H. E. Elsayed-Ali and J. W. Herman, "Superheating of Bi(0001)," *Phys. Rev.* **B 48**, pp. 4921-4924 (1993).

[4.16]. P. Carnevali, F. Ercolessi and E. Tosatti, "Melting and nonmelting behavior of the Au(111) surface," *Phys. Rev.* **B 36**, pp. 6701-6704 (1987).

[4.17]. F. D. Di Tolla, F. Ercolessi and E. Tosatti, "Maximum overheating and partial wetting of nonmelting solid surfaces," *Phys. Rev. Lett.* **74**, pp. 3201-3204 (1995).

[4.18]. H. Häkkinen and M. Manninen, "Computer simulation of disordering and premelting of low-index faces of copper," *Phys. Rev.* **B 46**, pp. 1725-1742 (1992).

[4.19]. G. Bilalbegovi , F. Ercolessi and E. Tosatti, "Orientational phase separation for vicinal surfaces close to the nonmelting Pb(111) face," *Europhys. Lett.* **17**, pp. 333-337 (1992).

[4.20]. H. J. Fecht and W. L. Johnson, "Entropy and enthalpy catastrophe as a stability limit for crystalline material," *Nature* **334**, pp. 50-51 (1988).

[4.21]. S. Lele, P. Ramachandra Rao and K. S. Dubey, "Entropy catastrophe and superheating of crystals," *Nature* **336**, pp. 567-568 (1988).

[4.22]. K. Lu and Y. Li, "Homogeneous nucleation catastrophe as a kinetic stability limit for superheated crystal," *Phys. Rev. Lett.* **80**, pp. 4474-4477 (1998).

[4.23]. M. Iwamatsu, "Homogeneous nucleation for superheated crystal," *J. Phys.: Condens. Mat.* **11**, pp. L1-L5 (1999).

[4.24]. J. F. van der Veen, B. Pluis and A. W. Denier van der Gon In: R. Vanselow and R. F. Howe, Editors, *Chemistry and Physics of Solid Surface VII*, (Springer, Berlin), pp. 455 (1988).

[4.25]. J. C. Heyraud and J. J. Métois, "Surface free energy anisotropy measurement of indium," *Surf. Sci.* **177**, pp. 213-220 (1986).

[4.26]. H. E. Elsayed-Ali and J. W. Herman, "Ultrahigh vacuum picosecond laser-driven electron diffraction system," *Rev. Sci. Instrum.* **61**, pp. 1636-1647 (1990).

[4.27]. H. E. Elsayed-Ali and J. W. Herman, "Picosecond time-resolved surface-lattice temperature probe," *Appl. Phys. Lett.* **57**, pp. 1508-1510 (1990).

[4.28]. M. Aeschlimann, E. Hull, C. A. Schmuttenmaer, J. Cao, L. G. Jahn, Y. Gao, H. E. Elsayed-Ali, D. A. Mantell and M. Scheinfein, "A picosecond electron gun for surface analysis," *Rev. Sci. Instrum.* **66**, pp. 1000-1009 (1995).

[4.29]. X. L. Zeng, Bo Lin, I. El-Kholy and H. E. Elsayed-Ali, "Time-resolved structural study of the Ge(111) high-temperature phase transition," *Surf. Sci.* **439**, pp. 95-102 (1999).

[4.30]. X. L. Zeng, B. Lin, I. El-Kholy and H. E. Elsayed-Ali, "Time-resolved reflection high-energy electron diffraction study of the Ge(111)-*c*(2×8)–(1×1) phase transition," *Phys. Rev. B* **59**, pp. 14907-14910 (1999).

[4.31]. M. G. Lagally, D. E. Savage and M. C. Tringides, Diffraction from disordered surfaces: an overview, *in Reflection High-Energy Electron Diffraction and*

Reflection Electron Imaging of the Surface, edited by P. K. Larsen and P. J. Dobson, (Plenum Press, New York), pp. 139 (1988).

[4.32]. N. Georgiev, A. Pavlovska and E. Bauer, "Surface disordering without surface roughening," *Phys. Rev.* ***B*** **52**, pp. 2878-2888 (1995).

[4.33]. M. Jaochowski and E. Bauer, "Quantum size and surface effects in the electrical resistivity and high-energy electron reflectivity of ultrathin lead films," *Phys. Rev.* ***B*** **38**, pp. 5272-5280 (1988).

[4.34]. A. Pavlovska, D. Dobrev and E. Bauer, "Orientation dependence of the quasi-liquid layer on tin and indium crystals," *Surf. Sci.* **314**, pp. 341-352 (1994).

[4.35]. H. E. Elsayed-Ali, T. B. Norris, M. A. Pessot and G. A. Mourou, "Time-resolved observation of electron-phonon relaxation in copper," *Phys. Rev. Lett.* **58**, pp. 1212-1215 (1987).

[4.36]. D. E. Gray, Editor, *American Institute of Physics Handbook* (third ed.), (McGraw-Hill, New York), (1972). G.W.C. Kays *Tables of Physical and Chemical Constants and Some Mathematical Functions* (fourteenth ed.), (Longman, London), (1973).

[4.37]. Z. H. Zhang, B. Lin, X. Zeng and H. E. Elsayed-Ali, "Surface morphology of laser-superheated Pb(111) and Pb(100)," *Phys. Rev.* ***B*** **57**, pp. 9262-9269 (1998).

[4.38]. X. Zeng and H. E. Elsayed-Ali, "Surface thermal expansion of Ge(111)," *Surf. Sci.* **442**, pp. L977-L982 (1999).

[4.39]. H. N. Yang, K. Fang, G.C. Wang and T. M. Lu, "Vacancy-induced disordering in the Pb(100) surface," *Phys. Rev.* **B 44**, pp. 1306-1310 (1991).

[4.40]. C. S. Lent and P. I. Cohen, "Diffraction from stepped surfaces. I. Reversible surfaces," *Surf. Sci.* **139**, pp. 121-154 (1984).

[4.41]. H. Toyoshima, T. Shitara, J. Zhang, J. H. Neave and B. A. Joyce, "A systematic RHEED study of regular and random steps on GaAs(001) surfaces," *Surf. Sci.* **264**, pp. 10-22 (1992).

[4.42]. Z. Mitura and J. L. Beeby, " Theoretical studies on the quantitative interpretation of RHEED data," *J. Phys.: Condens. Mat.* **8,** pp. 8717-8731 (1996).

[4.43]. U. Korte, J. M. McCoy and P. A. Maksym, "Perturbation theory of diffuse RHEED applied to rough surfaces: Comparison with supercell calculations," *Phys. Rev.* **B 54**, pp. 2121-2137 (1996).

[4.44]. H. Häkkinen and U. Landman, "Superheating, melting, and annealing of copper surfaces," *Phys. Rev. Lett.* **71**, pp. 1023-1026 (1993).

[4.45]. Y. S. Touloukian, R. K. Kirby, R. E. Taylor, P. D. Desai, in: *Thermophysical properties of matter* vol. 12, (Plenum Press, New York), (1975).

CHAPTER V REFERENCES:

[5.1]. Review articles in Phase transitions and adsorbate restructuring at metal surfaces, *The Chemical Physics of Solid Surfaces* Vol. 7, edited by D. A. King and D. P. Woodruff, (Elsevier, Amesterdam), (1994).

[5.2]. M. den Nijs, "Roughening-induced deconstruction in (110) facets of fcc crystals," *Phys. Rev. Lett.* **66**, pp. 907-910 (1991); *Phys Rev.* **B 46**, pp. 10386-10410 (1992).

[5.3]. U. Romahn, P. von Blanckenhagen, C. Kroll and W. Göpel, "Step-induced deconstruction and step-height evolution of the Au(110) surface," *Phys. Rev.* **B. 47**, pp. 12840-12851 (1993).

[5.4]. W. Moritz and D. Wolf, "Multilayer distortion in the reconstructed (110) surface of Au," *Surf. Sci.* **163**, pp. L655-L665 (1985); "Structure determination of the reconstructed Au(110) surface" *Surf. Sci.* **88**, pp. L29-L34 (1979); J. R. Noonan and H. L. Davis, **"**LEED analysis of the reconstructed Au(110) surface**,"** *J. Vac. Sci. Technol.* **16**, pp. 587-589 (1979); D. L. Adams, H. B. Nielsen, M. A. Van Hove, and A. Igatiev, "LEED study of the Pt(110)-(1×2) surface," *Surf. Sci.* **104**, pp. 47-62 (1981); C. M. Chan, M. A. Van Hove, W. H. Weinberg, and E. D. Willimas, "An R-factor analysis of several models of the reconstructed Ir(110)-(1×2) surface" *Surf. Sci.* **91**, pp. 440-448 (1980).

[5.5]. H. Derks, H. Hemme, W. Heiland, and S. H. Overbury, "Low energy ion scattering from the Au(110) surface - structural results," *Nucl. Instrum. Methods Phys. Res.* **B 23**, pp. 374-378 (1987); J. Möller, K. J. Snowden, W. Heiland, and H. Neihus, "Low energy ion scattering from the Au(110) surface," *Surf. Sci.* **178**, pp. 475-482 (1986); J. Möller, H. Neihus, and W. Heiland, "Direct measurement

of Au(110) surface structural parameters by low energy ion backscattering," *Surf. Sci* **166**, pp. L111-L114 (1986); M. Copel and T. Gustafsson, "Structure of Au(110) determined with medium-energy-ion scattering," *Phys. Rev. Lett.* **57**, pp. 723-726 (1986).

[5.6]. I. K. Robinson and D. Wolf, "Structure determination of the reconstructed Au(110) surface," *Surf. Sci.* **88**, pp. L29-L34 (1979).

[5.7]. D. T. Keane, P. A. Bancel, J. L. Jordan-Sweet, G. A. Held, A. Mak, and R. J. Birgeneau, "Evidence for two-step disordering of the Au(110)-(1×2) reconstructed surface," *Surf. Sci.* **250**, pp. 8-16 (1991).

[5.8]. L. D. Marks and D. J. Smith, "Direct imaging of carbon-covered and clean gold (110) surfaces," *Phys. Rev. Lett.* **51**, pp. 1000-1002, (1983).

[5.9]. J. M. Gimzewski, R. Berndt, and R. R. Schlittler, "Observation of mass transport on Au(110)-(1×2) reconstructed surfaces using scanning tunneling microscopy," *Surf. Sci.* **247**, pp. 327-332 (1991); J. K. Gimzewski, R. Berndt, and R. R. Schlittler, "Scanning-tunneling-microscope study of antiphase domain boundaries, dislocations, and local mass transport on Au(110) surfaces," *Phys. Rev.* **B 45**, pp. 6844-6857 (1992); S. Speller, S. Molitor, C. Röthig, J. Bömermann, and W. Heiland, "Surface mobility on the Au(110) surface observed with scanning tunneling microscopy," *Surf. Sci.* **312**, pp. L748-L752 (1994); L. Kuipers, M. S. Hoogenman, J. W. M. Frenken, and H. van Beijeren, "Step and kink dynamics on Au(110) and Pb(111) studied with a high-speed STM," *Phys. Rev.* **B 52**, pp. 11387-11397 (1995).

[5.10]. M. Sturmat, R. Koch, and K.H. Rieder, "Real space investigation of the roughening and deconstruction transitions of Au(110)," *Phys. Rev. Lett.* **77**, pp. 5071-5074 (1996).

[5.11]. M. J. Rost, R. van Gastel, and J. W. M. Frenken, "Anomalous shape and decay of islands on Au(110)," *Phys. Rev. Lett.* **84**, pp. 1966-1969 (2000).

[5.12]. M. J. Rost and J. W. M. Frenken, "Comment on "real space investigation of the roughening and deconstruction transitions of Au(110)," *Phys. Rev. Lett.* **87,** pp. 039603-1 (2001).

[5.13]. D. Cvetko, A. Lausi, A. Morgante, F. Tommasini, and K. C. Prince, "He beam study of deconstruction and roughening of Au(110)(1×2)," *Surf. Sci.* **269/270**, pp. 68-73 (1992).

[5.14]. C. Höfner and J. W. Rabalais, "Deconstruction of the Au{110}-(1 x 2) surface," *Phys. Rev.* **B. 58**, pp. 9990-9997 (1998).

[5.15]. D. Wolf, H. Jagodzinski and W. Moritz, "Diffuse LEED intensities of disordered crystal surfaces: III. LEED investigation of the disordered (110) surface of gold," *Surf. Sci.* **77,** pp. 265-282 (1978); W. Moritz, and D. Wolf, "Multilayer distortion in the reconstructed (110) surface of Au," *Surf. Sci.* **163**, pp. L655-L665 (1985).

[5.16]. J. C. Campuzano, M. S. Foster, G. Jennings, R. F. Willis, and W. N. Unertl, "Au(110) (1x2)-to-(1x1) phase transition: a physical realization of the two-dimensional ising model ," *Phys. Rev. Lett.* **54**, pp. 2684-2687 (1985).

[5.17]. J. Sprösser, B. Salanon, and J. Lapujoulade, "Roughening transition and deconstruction transition on Au(110)-(2x1)," *Europhys. Lett.* **16**, pp. 283-288 (1991).

[5.18]. L. Onsager, "Crystal statistics. I. A two-dimensional model with an order-disorder transition," *Phys. Rev.* **65,** pp. 117-149 (1944).

[5.19]. J. C. Campuzano, in The Au(110) (1×2)⇔(1×1) phase transition, *the chemical physics of solid surfaces* Vol. 7, edited by D. A. King and D. P. Woodruff (Elsevier, Amsterdam), (1994).

[5.20]. I. K. Robinson, "Direct determination of the Au(110) reconstructed surface by X-ray diffraction ," *Phys. Rev. Lett.* **50**, pp. 1145-1148 (1983).

[5.21]. W. Moritz and D. Wolf, "Multilayer distortion in the reconstructed (110) surface of Au," *Surf. Sci.* **163**, pp. L655-L665 (1985).

[5.22]. J. Möller, K. J. Snowdon, W. Fleiland and H. Niehus, "Low energy ion scattering from the Au(110) surface," *Surf. Sci.* **178** pp. 475-482 (1986); H. Derks. H. Hemme, W. Heiland and S. H. Overbury, "Low energy ion scattering from the Au(110) surface-structure results," *Nucl. Instrum. Methods* **B 23**, pp. 374-378 (1987).

[5.23]. M. Copel and T. Gustafsson, "Structure of Au(110) determined with medium-energy-ion scattering ," *Phys. Rev. Lett.* **57,** pp.723-726 (1986).

[5.24]. E. Vlieg, I. K. Robinson, "Relaxations in the missing-row structure of the (1×2) reconstructed surfaces of Au(110) and Pt(110)," *Surf. Sci.* **233**, pp. 248-254 (1990).

[5.25]. J. E. Avron, L. S. Balfour, C. G. Kuper, J. Landau, S. G. Lipson, and L. S. Shulman, "Roughening transition in the ^{4}He solid-superfluid interface," *Phys. Rev. Lett.* **45,** pp. 814-817 (1980); S. Balibar, D. O. Edwards, and C, Laroche, "Surface tension of solid ^{4}He," *Phys. Rev. Lett.* **42,** pp. 782-784 (1979); P. E.

Wolf. S. Balibar and F. Gallet, "Experimental observation of a third roughening transition on hcp ^{4}He crystals," *Phys. Rev. Lett.* **51**, pp. 1366-1369 (1983).

[5.26]. J. Villain and I. Vilfan, "Surface deconstruction of Au(110)," *Surf. Sci.* **199**, pp. 165-173 (1988).

[5.27]. J. C. Campuzano, A. M. Lahee, and G. Jennings, "On the feasibility of the missing row model of the (1×2) reconstructions of (110) Pt and Au," *Surf. Sci.* **152/153**, pp. 68-76 (1978).

[5.28]. M. G. Lagaly, D. E. Savage, arid M. C. Tringidcs, *in Reflection High-Energy Electron Diffraction and Reflection Imaging of Surfaces,* Vol. 188 of *NATO Advanced Study Institute Series B: Physics,* edited by K. Larson and P. J. Dohson (Plenum, New York), p. 139 (1988).

[5.29]. Z. H. Zhang, Bo Lin, X. L. Zeng, and H. E. Elsayed-Ali, "Surface morphology of laser-superheated Pb(111) and Pb(100) ," *Phys. Rev.* **B 57**, pp. 9262-9269 (1998).

[5.30]. Bo Lin and H. E. Elsayed-Ali, "Temperature dependent reflection electron diffraction study of In(111) and observation of laser-induced transient surface superheating," *Surf. Sci.* **498**, pp. 275-284 (2002).

[5.31]. X. Zeng, Bo Lin, I. El-Kholy, and H. E. Elsayed-Ali, "Time-resolved reflection high-energy electron diffraction study of the Ge(111)-*c*(2×8)–(1×1) phase transition," *Phys. Rev.* **B 59**, pp. 14907-14910 (1999).

[5.32]. J. W. Herman and H. E. Elsayed-Ali, "Time-resolved structural studies of the low-index faces of lead," *Phys. Rev.* **B 49**, pp. 4886-4897 (1994).

[5.33]. X. Zeng and H. E. Elsayed-Ali, "Time-resolved structural study of low-index surfaces of germanium near its bulk melting temperature," *Phys. Rev.* **B 64**, pp. 085410-085421 (2001).

[5.34]. Q. Yan, D. M. Zehner, F. W. Meyer, S. Schippers, "Projectile velocity and target temperature dependence of charge-state distributions of multicharged ions scattered during grazing interactions with a Au(110) surface," *Phys. Rev.* **A 54**, pp. 641-648 (1996).

[5.35]. H. N. Yong, T. M. Lu and G. C. Wang, "Collapsing of thermally induced steps on the Pb(111) surface." *Phys. Rev. Lett.* **62**, pp. 2148-2151 (1989).

[5.36]. M. Schick, "The classification of order-disorder transitions on surfaces," *Prog. In Surf. Sci.* **11**, pp. 245-292 (1981).

[5.37]. H. E. Stanleu, *Introduction to Phase Transitions and Critical Phenomena* (Oxford University Press, New York), (1971).

[5.38]. O. G. Mouritsen, *Computer Studies of Phase transition and Critical Phenomena*, (Springer-Verlag, Berlin), (1984).

[5.39]. W. Moritz and M. G. Lagally, Phys. "Reliability of low-energy electron diffraction for studies of surface order-disorder phenomena," *Phys. Rev. Lett.* **56**, pp. 865-868 (1986).

[5.40]. J. M. Van Hove and P. I. Cohen, "RHEED streaks and instrument response," *J. Vac. Sci. Technol.* **A1**, pp. 609-613 (1983).

[5.41]. H. N. Yang and T. M. Lu, "Enhancement of thermal diffuse scattering by surface defects," *Phys. Rev.* **B 44**, pp. 11457-11464 (1991).

[5.42]. H. N. Yang, K. Fang, G. C. Wang, and T. M. Lu, "Vacancy-induced disordering in the Pb(100) surface," *Phys. Rev.* **B 44**, pp. 1306-1310 (1991).

[5.43]. A. Hoss, M. Nold, P. von Blanckenhagen and O. Meyer, "Roughening and melting of Au(110) surfaces," *Phys. Rev.* **B 45**, pp. 8714-8720 (1992).

[5.44]. H. N. Yang, T. M. Lu and G. C. Wang, "High-resolution low-energy electron-diffraction analysis of the Pb(110) roughening transition," *Phys. Rev.* **B 43**, pp. 4714-4727 (1991).

[5.45]. B. Bölger, P. K. Larsen, and G. Meyer Ehmsen, *in Reflection High-Energy Electron Diffraction and Reflection Imaging of Surfaces*, **Vol. 188** of NATO Advanced Study Institute Series B: Physics, edited by K. Larson and P. J. Dohson (Plenum, New York), p. 201 (1988).

[5.46]. U. Korte, J. M. McCoy, P. A. Maksym, and G. Meyer-Ehmsen, "Perturbation theory of diffuse RHEED applied to rough surfaces: Comparison with supercell calculations," *Phys. Rev.* **B 54**, pp. 2121-2137 (1996).

[5.47]. Z. L. Wang, "Statistical multiple diffuse scattering from rough surfaces in RHEED - Beyond the distorted-wave Born approximation," *Surf. Sci.* **366**, pp. 377-393 (1996).

[5.48]. G. Meyer-Ehmsen, "Real-space dynamical calculation of diffuse RHEED intensities from disordered surfaces," *Surf. Sci.* **395**, pp. L189-L195 (1998).

CHAPTER VI REFERENCES:

[6.1]. S. A. Nepijko. N. N. Sedov, O. Schmidt, G. H. Fecher, and G. Schönhense, "Size of three-dimensional objects measured by means of photoemission electron microscopy," *Ann. Phys.* **11**, pp. 39-48 (2002).

[6.2]. P. Bräunlich, B. Rosenblum, and J. P. Carrico, "Imaging of surfaces with the exoelectron microscope," *Appl. Phys. Lett.* **22**, pp. 61-63 (1973).

[6.3]. M. Mundschau, "Emission microscopy and surface science," *Ultramicroscopy* **36**, pp. 29-51 (1991).

[6.4]. W. Engel, M. E. Kordesch, H. H. Rotermund, S. Kubala, and A. von Oertzen, "AUHV-compatible photoelectron emission microscope for applications in surface science," *Ultramicroscopy* **36**, pp. 148-153 (1991).

[6.5]. G. H. Griffith, P. A. Habliston, and G. B. Birrell, "Bibliography on emission microscopy, mirror electron microscopy, low-energy electron microscopy and related techniques: 1985-91", *Ultramicroscopy* **36**, pp. 262-274 (1991).

[6.6]. H. E. Elsayed-Ali and J. W. Herman, "Ultrahigh vacuum picosecond laser-driven electron diffraction system," *Rev. Sci. Instrum.* **61**, pp. 1636-1647 (1990).

[6.7]. C. A. MacDonald, A. M. Malvezzi, and F. Spaepen, "Picosecond time-resolved measurements of crystallization in noble metals," *J. Appl. Phys.* **65**, pp. 129-136 (1989).

[6.8]. P. E. Dyer, S. R. Farrar, and P. H. Key, "Fast time-response photoacoustic studies and modelling of KrF laser ablated $YBa_2Cu_3O_7$," *Appl. Surf. Sci.* **54**, pp. 255-263 (1992).

[6.9]. Numerous references in, e.g., D. Bäuerle, *Laser Processing and Chemistry* (Springer, Berlin), (1996).

[6.10]. O. Bostanjolo and E. Endruschat, "Kinetics of laser-induced liquid metal etching of a-Si films," *Phys. Stat. Sol.* **91**, pp. 457-462 (1985); O. Bostanjolo, *Advances in Electronics and Electron Physics*, **76**, pp. 209 (1989).

[6.11]. T. Hsu and L. M. Peng. *in Reflection High-Energy Electron Diffraction and Reflection Electron Imaging of Surfaces*. Edited by P. K. Larsen and P. J. Dobson (P1enurn Press, New York, 1987); Yagi, *in Reflection High-Energy Electron Diffraction and Reflection Electron Imaging of Surfaces*, Edited by P. K. Larsen and P. J. Dobson (Plenum Press, New York), (1987)

[6.12]. W. Telieps and E. Bauer, "An analytical reflection and emission UHV surface electron microscope," *Ultramicroscopy* **17**, pp. 57-65 (1985).

[6.13]. J. W. Herman and H. E. Elsayed-Ali, "Superheating of Pb(111)," *Phys. Rev. Lett.* **69**, pp. 1228-1231 (1992); "Time-resolved structural studies of the low-index faces of lead," *Phys. Rev.* **B. 49**, pp. 4886-4897 (1994).

[6.14]. E. A. Murphy, H. E. Elsayed-Ali, and J. W. Herman, "Superheating of Bi(0001)," *Phys. Rev.* **B 48,** pp. 4921-4924 (1993).

[6.15]. Bo Lin and H. E. Elsayed-Ali, "Temperature dependent reflection electron diffraction study of In(111) and observation of laser-induced transient surface superheating," *Surf. Sci.* **498**, pp. 275-284 (2002).

[6.16]. X. L. Zeng, Bo Lin, I. El-Kholy and H. E. Elsayed-Ali, "Time-resolved structural study of the Ge(111) high-temperature phase transition," *Surf. Sci.* **439**, pp. 95-102 (1999).

[6.17]. H. Hakkinen and Uzi Landman, "Superheating, melting, and annealing of copper surfaces," *phys. Rev. Letts.* **71**, pp. 1023-1026 (1993).

[6.18]. M. Iwamatsu, "Homogeneous nucleation for superheated crystal," *J. Phys. Condens. Matter* **11**, pp. L1-L5 (1999).

[6.19]. O. Schmidt, M. Bauer, C. Wiemann, R. Porath, M. Scharte, O. Andreyev, G. Schönhense, M. Aeschlimann, "Time-resolved two photon photoemission electron microscopy," *Appl. Phys.* **B 74**, pp. 223-227 (2003).

[6.20]. O. Bostanjoglo and M. Weingärtner, "Pulsed photoelectron microscope for imaging laser-induced nanosecond processes," *Rev. Sci. Instrum.* **68(6),** pp. 2456-2460 (1997).

[6.21]. G. A. Massey, M. D. Jones and B. P. Plummer, "Space-charge aberrations in the photoelectron microscope," *J. Appl. Phys.* **52(3)**, pp. 3780-3786 (1981).

[6.22]. G. F. Rempfer, "Unipotential electrostatic lenses: Paraxial properties and aberrations of focal length and focal point," *J. Appl. Phys.* **57**, pp. 2385-2401 (1985).

[6.23]. Z. H. Zhang. Bo Lin, X. L. Zeng, and H. E. Elsayed-Ali, "Surface morphology of laser-superheated Pb(111) and Pb(100)," *Phys. Rev.* **B 57**, pp. 9262-9269 (1998).

[6.24]. Y. S. Toukoukian, *Thermophysical Properties of Matter*, (Plenum, New York), Vol. 1 and 4 (1970).

[6.25]. A. Damascelli, G. Gabetta, A. Lumachi, L. Fini and F. Parmingiani, "Multiphoton electron emission from Cu and W: An angle-resolved study," *Phys. Rev.* **B 54**, pp. 6031-6034 (1996).

[6.26]. C. Hernandez Garcia and C. A. Brau, "Electron beam formed by photoelectric field emission" *FEL2000/proceedings,* MO-3-09 (2000).

Appendix A: Ultrafast Laser System

In order to heat a crystal surface over 10 mm in diameter and up to several hundred degrees over 100-ps time scale, an ultra-fast high-energy laser system was assembled. The requirements of ultra-fast laser system for superheating experiments have characteristics of pulse width shorter than 100-ps with energy up to 20-30 mJ. This ultrafast laser system includes a Nd:YAG oscillator as a seed laser with 100-ps pulses with nanojoule energy per pulse, regenerative amplifier which can amplify the pulse by almost a factor of one million, and a single pass amplifier to amplify the pulse energy further to ~30 mJ range. The oscillator laser used in this thesis is based on a Quantronix Nd:YAG actively mode-locked laser which provides ~100-ps pulse with a repetition rate of 82 MHz. The average power of the oscillator is 12 W. I redesigned and rebuilt a Nd:YAG regenerative amplifier to amplify the seed pulse of the oscillator. The regenerative amplifier uses a Quantronix 117 laser head. A Pockels cell that is controlled by a Medox Pockels cell driver selects a pulse from the oscillator pulse train and injects it into the regenerative amplifier. The selected pulse is coupled to the regenerative amplifier by a wedge mirror with ~4% reflection. The regenerative amplifier is actually a laser cavity that is a free-running laser to produce nanosecond laser pulses when Pockels cell is operated.

Figure 44 shows a schematic of the ultra-fast high-energy laser system. The injection pulse is introduced into regenerative amplifier through a wedge reflector. In order to avoid feedback from the regenerative amplifier, which would adversely affect the model-locking pulses, a slight misalignment is needed which is provided by the wedge. Then, a fast high-voltage step is applied to intracavity Pockets cell, which

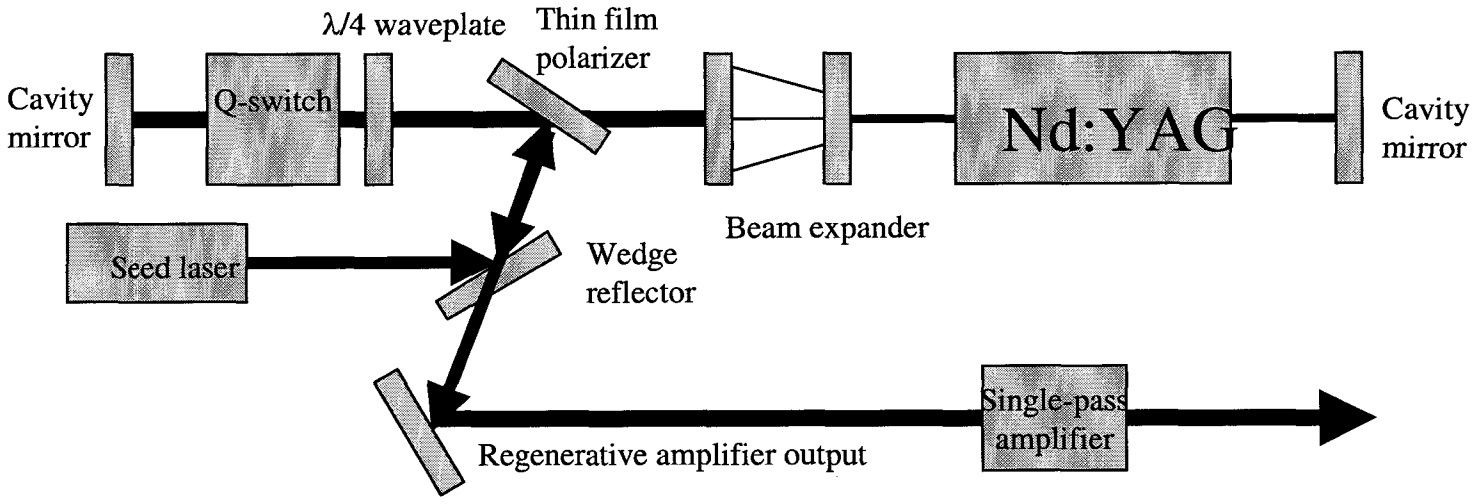

Figure 49. Schematic diagram of the regenerative Nd:YAG amplifier. Because the intra-cavity intensity is high and causes damage of the Q-switch crystal, a beam expander is placed inside the cavity to reduce the intensity. The thin film polarizer is used to introduce the seed pulse to the cavity and dump the laser pulse after amplification.

introduces quarter-wave rotation that allows the seed pulse to amplify inside regenerative cavity. With each round pass through the regenerative amplifier, the energy of the injected pulse is increasingly amplified. The amplification is very fast for the first 12-16 round trips in the regenerative amplifier. Then, the energy of injected pulse begins to saturate. After reaching the saturation point, the energy of injected pulse is decreased with each round trip. The energy of injected pulse varies from pulse to pulse inside regenerative amplifier cavity and is observed from leakage out of one of the cavity mirrors. The best time to cavity dump the amplified pulse is one round trip after saturation. The timing to switch out the pulse is important because the right timing can produce a pulse with maximum amplitude and high stability. Figure 45 shows the output pulse from regenerative amplifier. The pulse-to-pulse stability of the regenerative amplifier is better than 5% over an extended period of time. This regenerative amplifier is able to produce 100-ps laser pulses with energy more than 1.2 mJ at λ = 1064 nm and a repetition rate of 820 Hz.

After the regenerative amplifier, a single-pass amplifier from Kigre, was used to further amplify the pulse energy to 30 mJ at a repetition rate of 50 Hz. A silicon photo-detector receives single from the pulse of the single pass amplifier flash lamp as initial trigger. The pump pulse of flash lamp for single pass amplifier is much longer compared to laser pulse. At certain timing and pump pulse level, the photo-detector sends a signal to the Pockels cell of the regenerative amplifier to trigger it. The pulse-to-pulse stability of the single pass amplifier is about 8%. Finally, the ultra-fast high-energy laser system can provide pulse energies of 20 mJ with 100-ps pulse width at a repetition rate up to 50 Hz.

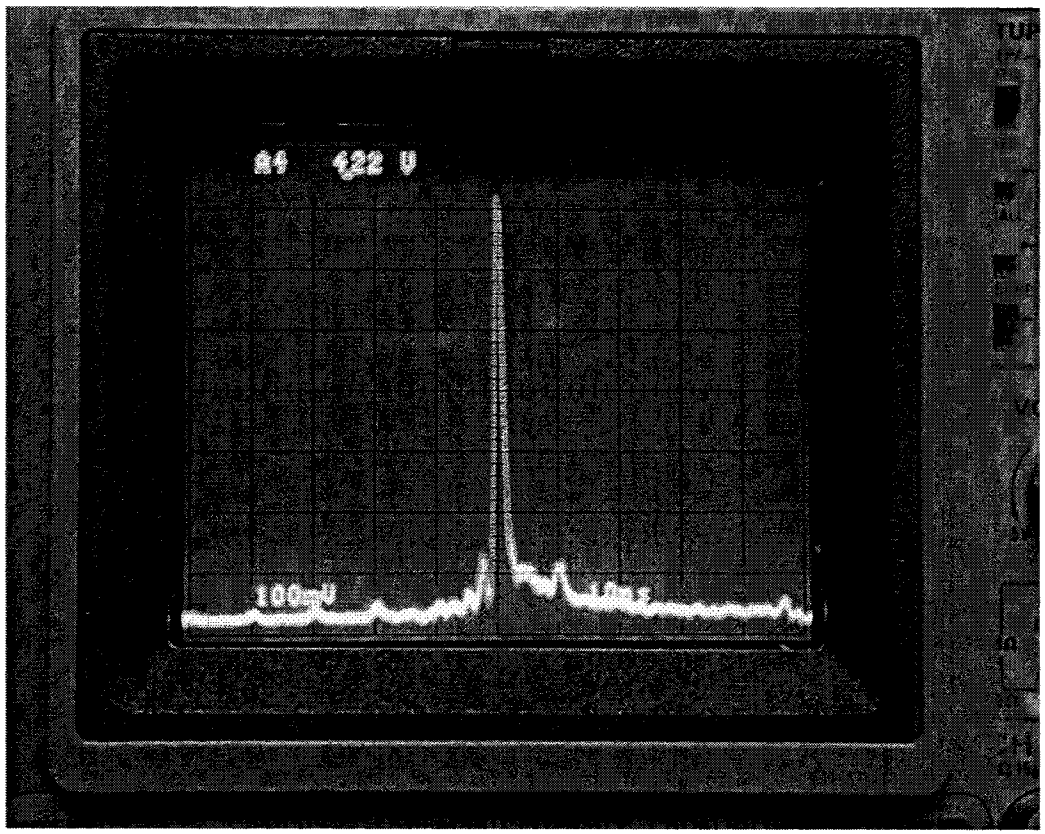

Figure 50. The output laser pulse after the amplifier. Because the 100-ps pulse width is over the limit of the detection resolution, the pulse width in the oscilloscope does not represent the pulse shape. A pulse width of 90-ps pulse is observed by the autocorrelator.

Appendix B. Autocorrelator

In our experiments, a 100-ps pulse laser was used. Because the 100-ps laser pulse is too short to be measured by electronic detectors directly, A noncolinear autocorrelator is used to measure the pulse duration. The standard method to measure the short pulse is based on intensity autocorrelation by means of second harmonic generation (SHG) in a Michelson type interferometer. In a noncolinear autocorrelator, a pulse is split into two equal parts and then recombined in a nonlinear mixing crystal. The BBO (Beta Barium Borate) crystal was used in our autocorrelator as the nonlinear mixing crystal.

When two short pulses is mixed in the BBO crystal, the generated SHG pulse is proportional to the temporal overlap of the pulses. The autocorrelation function is given as following:

$$G(s) = \int f(t)f(t+s)dt \,/\, \int f(t)f(t)dt$$

Where f(t) is the intensity of a laser pulse with width $\Delta\tau$, f(t+s) is the intensity of a laser pulse at a different time. The exact relationship between nonlinear autocorrelation half-width and laser pulse width also depends on the temporal shape of the laser pulse. The temporal shape of our 100-ps laser pulse is Gaussian that results in 0.707 ratio between half-width pulse $\Delta\tau$ and autocorrelation half-width Δs.

Figure 46 shows the setup of our homemade autocorrelator. A 50% beam splitter separates a laser pulse into two equal parts. A temporal delay is introduced into one beam by moving the 180° folding prism on one arm to produce a time shift. The reflector is driven by a translation stage to make a delay. Then, the two beams are recombined by a focus lens. The two beams are focused into a BBO crystal at same position. Because the

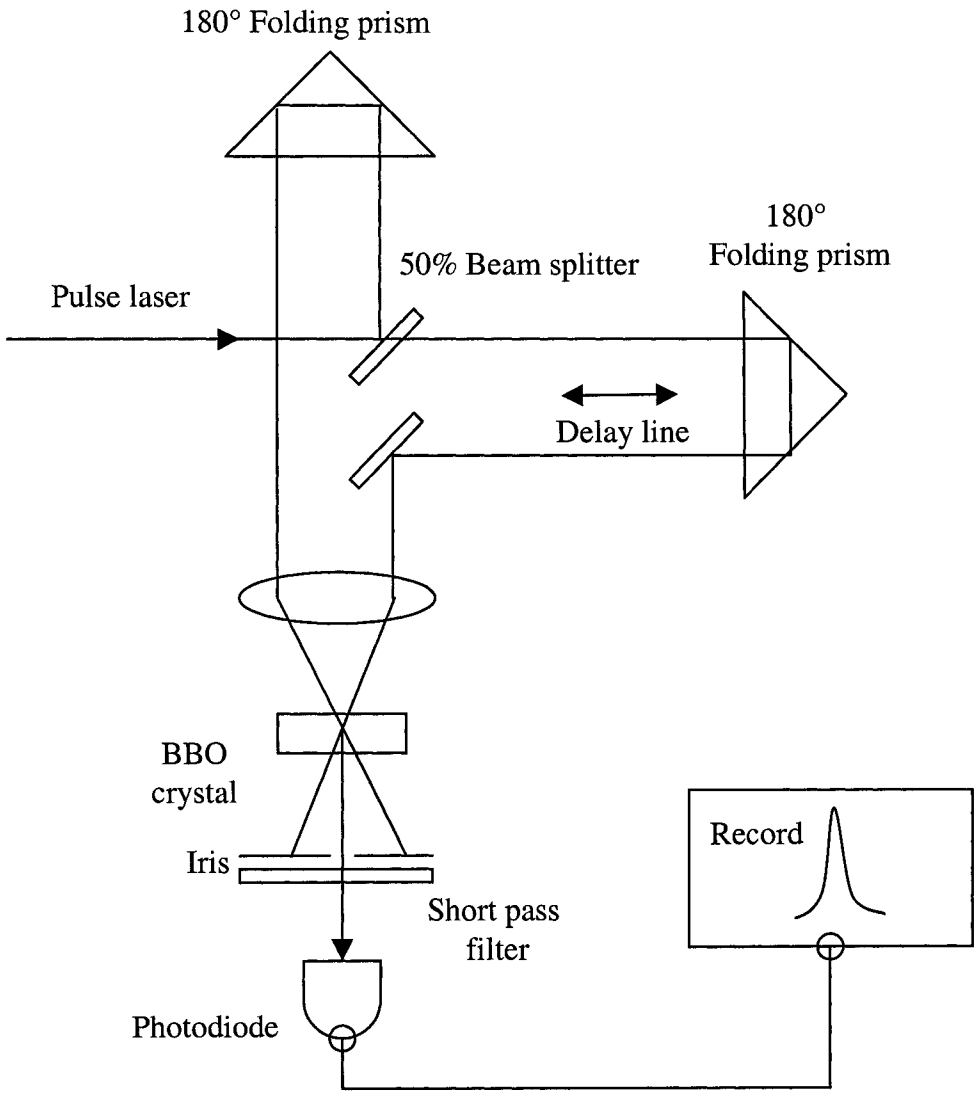

Figure 51. Schematic diagram of the noncolinear autocorrelator is shown for measurement of picosecond pulse width. One arm of 180° folding prism is placed on the translation stage.

SHG signal generated by the BBO crystal is proportional to the temporal overlap of the pulses, the variation of the signal as a function of delay time can be used as a measure of pulse width. The SHG output is then incident onto a fast silicon photodetector and the signal is recorded. In order to reduce the background, the iris and short wavelength pass filter were inserted between the BBO crystal and the photodetector.

The time delay, $\Delta\tau$, can be calculated from the difference of the optical paths, Δs. Therefore, the pulse width is equal to $\Delta\tau = 0.707\Delta s/c_{light}$, where c_{light} is the speed of light and the factor 0.707 is introduced by the Gaussian temporal pulse shape. Figure 47 shows an example of measured pulse width of our picosecond laser.

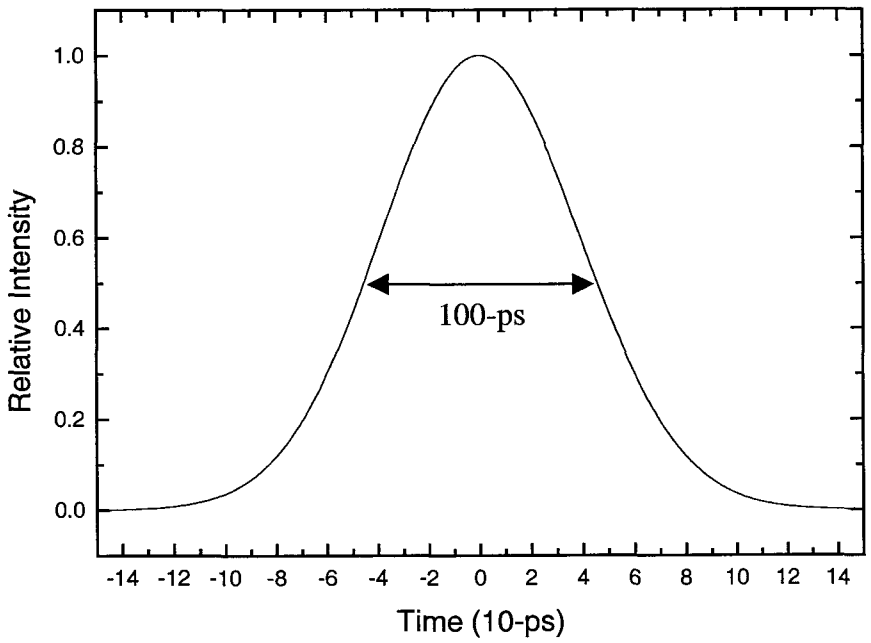

Figure 52 The picosecond laser pulse after the regenerative amplifier. The full width at half maximum of the laser pulse is 100 picosecond.

CURRICULUM VITA

For

BO LIN

DEGREES:

Doctor of Philosophy (Electrical Engineering), Old Dominion University, Norfolk, Virginia, August, 2003

Master of Science (Optics), Zhejiang University, HangZhou, Zhejiang, P. R. China, August, 1988

Bachelor of Science (Physics), Lanzhou University, LanZhou, Gansu, P. R. China, August, 1982

PART TIME EMPLOYMENT:

Department of Electrical and Computer Engineering,
Old Dominion University, Norfolk, Virginia

Research Assistant, September 1995-December 2000